NTNU
Norwegian University of
Science and Technology

Hydrogen Induced Stress Cracking of Inconel 625

Effect of Production Method, Heat Treatment and Cold Working

Eivind Bruun Thorstensen

Chemical Engineering and Biotechnology
Submission date: June 2016
Supervisor: Otto Lunder, IMTE
Co-supervisor: Roy Johnsen, IPM

Norwegian University of Science and Technology
Department of Materials Science and Engineering

Abstract

The following work has examined the effect of heat treatment, production method and cold working (CW) on the hydrogen induced stress cracking (HISC) susceptibility of Inconel 625 (UNS N06625). This was done by hydrogen pre-charging and stepwise loading in Cortest proof rings, followed by an investigation of the fracture surfaces in a scanning electron microscope (SEM). Five different versions of Inconel 625 were examined; one hot isostatic pressed (HIP), one cold worked and three forged qualities. The three forged qualities were subjected to heat treatment at 920°C, 1010°C and 1100°C, respectively. An attempt was also made to estimate the critical hydrogen concentration necessary for brittle fracture to occur in Inconel 625. This was done by combining diffusion calculations with hydrogen measurements performed by SINTEF. The critical pitting temperature (CPT) for the different versions of Inconel 625 was obtained by a modified version of the ASTM G48 test.

The forged and the HIPed versions of Inconel 625 were found to be susceptible to HISC. This was based on a decrease in strength and ductility, as well as brittle fracture surfaces and secondary cracking on the samples' outer surface. The CW samples showed a higher resistance to HISC, as no reduction in fracture strength, nor any secondary cracking was observed. Forged samples heat treated at 1010°C were found to be the most susceptible to HISC, while heat treatment at 1100°C resulted in the lowest HISC susceptibility amongst the forged qualities. The amount of grain boundary carbides was found to be the main factor influencing the HISC susceptibility, where an increased amount led to a higher susceptibility. The effect of grain size on the HISC susceptibility of Inconel 625 samples charged with hydrogen is still unresolved, but the results indicate that larger grains have a beneficial effect on the ductility. The CPT was found to decrease with increasing heat treatment.

Sammendrag

I denne masteren har effekten av varmebehandling, produksjonsmetode og kaldbearbeiding (CW) på mottakeligheten for hydrogenindusert spenningsbrudd (HISC) i Inconel 625 (UNS N06625) blitt undersøkt. Dette innebar forladning med hydrogen og trinnvis lastøkning i Cortest proof ringer, etterfulgt av en undersøkelse av bruddflatene i sveipelektronmikroskop (SEM). Fem forskjellige versjoner av Inconel 625 ble undersøkt; en varm isostatisk presset (HIP), en kaldarbeidet og tre smidde. De tre smidde versjonene ble utsatt for varmebehandling ved henholdsvis 920°C, 1010°C og 1100°C. Det ble også gjort et forsøk på å estimere den kritiske hydrogenkonsentrasjonen nødvendig for å oppnå sprøbrudd i Inconel 625. Dette ble gjort ved å kombinere diffusjonsberegninger med hydrogenmålinger utført av SINTEF. Den kritiske pitting temperaturen (CPT) for de forskjellige versjonene av Inconel 625 ble målt ved å bruke en modifisert versjon av ASTM G48 testen.

De smidde og HIPede versjonene av Inconel 625 viste seg å være mottakelige for HISC. Dette var basert på en nedgang i styrke og duktilitet, i tillegg til sprø bruddflater og sekundære sprekker på prøvenes ytre overflate. De kaldbearbeidete prøvene viste en høyere motstand mot HISC, da det ikke ble observert noen nedgang i styrke eller sekundære sprekker for disse prøvene. De smidde prøvene varmebehandlet ved 1010°C viste seg å være mest mottakelige for HISC, mens varmebehandling ved 1100°C førte til den laveste HISC mottakeligheten blant de smidde prøvene. Hovedfaktoren som påvirket HISC mottakeligheten viste seg å være mengden korngrensekarbider, der økt mengde ga høyere mottakelighet. Effekten av kornstørrelse på HISC mottakeligheten for prøver av Inconel 625 ladet med hydrogen er fortsatt usikker, men resultatene i denne masteren indikerer at større korn har en gunstig effekt på duktiliteten. Den kritiske pitting temperaturen sank ved økende varmebehandling.

Preface

This master's thesis is submitted to NTNU as part of the Master's program at the Department of Materials Science and Engineering. Professor Otto Lunder has supervised this work with Professor Roy Johnsen and Ph.D. Gaute Stenerud as co-supervisors. The project is sponsored by DNV GL and OneSubsea. Vebjørn Andresen has been the industrial contact representing DNV GL and Paal Bratland has been the industrial contact representing OneSubsea.

I would like to thank Roy Johnsen for the numerous, insightful discussions in his office and for always keeping me motivated. Special thanks is due to Gaute Stenerud for invaluable help in all things related to this thesis. I would also like to thank DNV GL and OneSubsea for providing financial support and Vebjørn Andresen and Paal Bratland for their contribution to this project.

I would like to extend my gratitude toward Peder Braadland and Jostein Thorstensen for proof reading and to Bernt Thorstensen for hours of insightful debate on the subject of metallurgy. Finally, thanks are due to Yingda Yu for help with the SEM, to Pål Christian Skaret for performing the tensile testing and to Trygve Schanche and Nils-Inge Nilsen for help in the laboratory.

Trondheim, June 14, 2016

Eivind Bruun Thorstensen

List of Figures

List of Tables

List of Equations and Chemical reactions

List of abbreviations

Ag/AgCl	Silver/Silver Chloride reference electrode
ASTM	American Society for Testing and Materials
ATI	Allegheny Technologies Incorporated
AIDE	Absorption-Induced Dislocation Emission
BCT	Body-Centered Cubic
$\mathbf{C_{critical}}$	Critical hydrogen Concentration for brittle fracture
$\mathbf{C_s}$	Surface Concentration of hydrogen
CCT	Critical Crevice Temperature
CP	Cathodic Protection
CPT	Critical Pitting Temperature
CW	Cold work
E	Potential
$\mathbf{E_{corr}}$	Corrosion Potential
$\mathbf{E_{prot}}$	Protection Potential
EDS	Energy Dispersive Spectroscopy
FCC	Face-Centered Cubic
HCP	Hexagonal Close Packed
HE	Hydrogen Embrittlement
HEAC	Hydrogen-Environment-Assisted Cracking
HEDE	Hydrogen-Enhanced Decohesion
HELP	Hydrogen-Enhanced Localized Plasticity
$\mathbf{Hg/HgSO_4}$	Mercury/Mercurysulphate reference electrode
HIC	Hydrogen Induced Cracking
HIP	Hot Isostatic Pressing
HISC	Hydrogen-Induced Stress Cracking
HRC	Rockwell Hardness
HV	Vickers Hardness
$\mathbf{H_3PO_4}$	Phosphoric Acid
I	Current
$\mathbf{I_{corr}}$	Corrosion Current
IHAC	Internal-Hydrogen-Assisted Cracking

MPA	Mega Pascal
N/A	Not Available
NTNU	Norwegian University of Science and Technology
OCP	Open Circuit Potential
OM	Optical Microscope
PM	Powder Metallurgy
ppmw	Parts Per Million by Weight
RA	Reduction of Area
$\mathbf{RA_H}$	Reduction of Area for hydrogen exposed samples
$\mathbf{RA_{ref}}$	Reduction of Area for reference sample
RRA	Reduction of Reduction of Area
SEM	Scanning Electron Microscope
ss	Surface Site
SSC	Sulfide Stress Cracking
TEM	Transmission Electron Microscope
TTT	Time-Temperature-Transformation
UTS	Ultimate Tensile Strength
VDM	United German Metalworks
YS	Yield Strength
wt%	Weight Percentage

Table of contents

1 Introduction

The development of UNS N06625, hereafter referred to as Inconel 625, was started in the 1950s to meet the demand for high-strength piping material for super critical steam power plants [1]. At the time of its release on the marked in 1964, the unique properties of Inconel 625 were described in the patent as its high tensile strength and resistance to creep and stress rupture at elevated temperatures [2]. Inconel 625 has since proven to be a versatile alloy that has a wide range of application, including in aerospace, marine and oil- and gas-industry. The reason for this is its combination of high strength and ductility, good weldability, high temperature creep resistance and resistance to corrosion in a variety of environments [3].

Inconel 625 is classified as immune to corrosion in seawater at temperatures up to 30°C and is therefore normally not in need of cathodic protection (CP) [4]. However, coupling with less noble metals in need of such protection can still lead to the cathodic protection of components made of Inconel 625. This will cause hydrogen to evolve at the surface of the material and thereby act as a source of hydrogen [5]. Hydrogen can then diffuse into the material and cause hydrogen embrittlement (HE). If the material is susceptible and a stress is applied, this can lead to hydrogen-induced stress cracking (HISC). Because of the low diffusion rate of hydrogen in Inconel 625, the alloy was previously considered immune to HISC in seawater [6]. Studies showing the HISC susceptibility of similar nickel alloys [7, 8], as well as possible HISC related failure reports from the collaborators of this project, has led to the wish for an examination of the HISC susceptibility of Inconel 625.

This work is a continuation of the author’s previous project work, where Inconel 625 was found to be susceptible to HISC [9]. The main focus of this thesis is to gain a better understanding of the HISC susceptibility of Inconel 625 by investigating the effect of heat treatment, production method and cold working (CW). To get a broader basis for evaluating these effects, the results from the author’s previous work will be presented as part of this thesis. The results obtained in Erlend Haugsnes MSc at NTNU for a cold worked Inconel 625 will also be included [10].

1.1 Objective

The main objective of this work is to examine the effect of heat treatment, production method and cold working on the HISC susceptibility of Inconel 625. This will be done by hydrogen pre-charging and stepwise loading in Cortest proof rings. Experiments will also include basic mechanical testing, precipitate characterization by energy dispersive spectroscopy (EDS), a modified version of the ASTM G48 test to determine the critical pitting temperature (CPT) and investigation in the optical microscope (OM) and the scanning electron microscope (SEM).

2 Theory

2.1 The microstructure of Inconel 625

Inconel 625 is a nickel base alloy with an austenitic, face-centered cubic (FCC) matrix phase, denoted γ. The strength of the alloy is mainly achieved through solid solution strengthening by chromium, molybdenum and niobium [11]. These impurity atoms will go into substitutional solid solution and impose lattice strains on the surrounding host atoms because of the difference in atomic size [12]. This is illustrated in Figure 2.1. The resulting strain fields will interact with the strain fields imposed by dislocations, thereby restricting dislocation motion and strengthening the material.

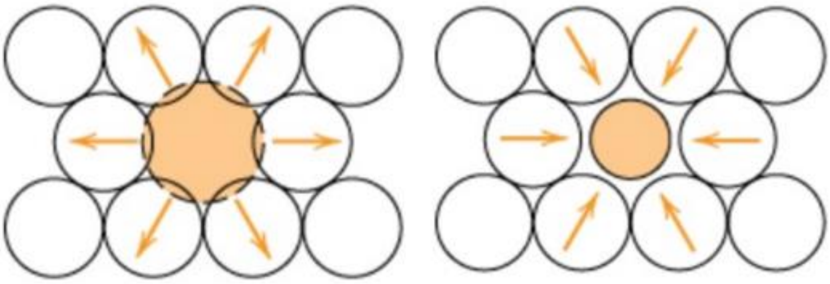

Figure 2.1: Lattice strains imposed by atoms in solid solution. Larger atoms impose compressive strains (left) and smaller atoms impose tensile strains (right). Pictures taken from Callister [12].

Although Inconel 625 is not classified as a precipitation-hardened alloy, it is possible to achieve precipitation hardening if the content of Nb is above 4% [3]. The resulting phase is the metastable Ni_3Nb, denoted γ''. This phase has a body-centered tetragonal (BCT) structure and is coherent with the austenite matrix [13]. When this secondary phase is formed within the original phase matrix, there will be a lattice misfit of about 3% [14]. The following distortion of the crystal lattice around the γ'' particles will impede dislocation motion during plastic deformation, making the alloy harder and stronger. γ'' is formed as ellipsoidal, disc-shaped particles at temperatures between 550°C and 850°C.

Upon prolonged ageing at elevated temperature (650-900°C), the metastable γ'' phase will transform into the stable, orthorhombic δ-Ni_3Nb [15]. This phase is incoherent with the Ni matrix and therefore not an effective strengthener. It will also lead to a reduction of ductility and toughness, making the alloy more exposed to embrittlement [16]. The δ-phase is often found at grain boundaries and can impede grain growth at higher temperatures, which is favorable. However, because of its adverse effect on mechanical properties, this phase is generally undesirable. The δ-phase is normally recognized by its characteristic needle-shaped morphology, but globular δ particles have also been observed [13].

Different carbides can also form in Inconel 625, the most notable being MC, M_6C and $M_{23}C_6$. The MC carbides, where M is mainly Nb and Ti, will form between 900°C and 1050°C. These carbides exhibits an FCC crystal structure and will form as both dispersed particles in the metal matrix and as thin grain boundary films [16]. Because of their dense, closely packed structure, these compounds are strong and stable [17]. The M_6C carbides will form at approximately the same temperature, but with a complex cubic crystal structure. Here, M is principally Ni, Cr and Mo. At lower temperatures, in the range of 700°C-950°C, the $M_{23}C_6$ carbide will form. This carbide exhibits the same crystal structure as M_6C, but M is almost entirely Cr. Both M_6C and $M_{23}C_6$ have blocky, irregular shapes and form as a series of separate, discrete grain boundary particles [3]. When the molybdenum content in nickel-base superalloys exceeds about 6 %, M_6C will form at the expense of $M_{23}C_6$ as the principal grain boundary precipitate [17]. Grain boundary carbides will act much in the same way as the δ-phase on the mechanical properties of the material and can give a significant reduction in ductility and toughness. Carbides have also been shown to increase a metals susceptibility to hydrogen embrittlement [18, 19]. However, grain boundary carbides can have a positive effect on the mechanical properties by pinning the grain boundaries during heat treatment. This is known as the Zener effect [20]. When a carbide is present at a grain boundary, the total grain boundary area will be reduced. For a grain boundary to expand, i.e. for a grain to grow, the grain boundary will have to move past the carbide. This requires the formation of new grain boundary, which is energetically unfavorable [20]. The result of the Zener effect is that grain growth will be hindered during heat treatment.

A high content of alloying elements in Inconel 625 can lead to the formation of the Laves phase. This is an intermetallic compound with a hexagonal close packed (HCP) crystal structure and A_2B stoichiometry, where A can be Ni, Fe, Cr and Co, while B can be Nb, Ti, Si and Mo [14]. The Laves phase forms at long exposure times to temperatures above 700°C and is therefore normally not a problem during production, but can form during long-term use at elevated temperatures. Because of the detrimental effects on strength and ductility, the Laves phase is avoided as far as possible. By lowering the Nb, Si and Mo content, the Laves phase can be almost completely eliminated, as these are the strongest contributors to Laves formation [3].

2.2 Effect of grain size of mechanical properties

The size of the grains plays an important role on the mechanical properties of most metals. This is explained by dislocation movement and pile-up. During plastic deformation, dislocations will move through the grain and pile up at the grain boundaries [12]. The pile-up causes a stress to be generated in the adjacent grain, and, upon reaching a critical value, will generate new dislocations in the adjacent grain. In this way, the plastic deformation is propagated from grain to grain. Adjacent grains will also normally have different crystallographic orientation. As a result, a dislocation moving through one grain will have to change its direction of motion when it moves into the next grain. This becomes increasingly difficult as the crystallographic misorientation increases. The grain size will determine the amount of dislocations that can pile up at a grain boundary. In large grains, more dislocations can pile up, and the resulting stress generated in the adjacent grain will increase. This will make it easier to propagate dislocations in the neighboring grain. Larger grains will also decrease the number of times the dislocations have to change their direction of motion. As a result, small grains will increase both the strength and the toughness of the material [12]. The effect of grain size on strength is expressed by the Hall-Petch relationship [21]:

$$\sigma_y = \sigma_0 + k_y d^{-\frac{1}{2}} \tag{1}$$

Where σ_y is the yield strength, σ_0 and k_y are constants and d is the grain diameter.

2.3 Effect of heat treatment on Inconel 625

Nickel alloys may be subjected to one or more of six principal types of heat treatments, depending on chemical composition, fabrication requirements and intended service [22]. For Inconel 625, the most common heat treatments are annealing, solution annealing and precipitation hardening [2]. The temperature at which different phases are formed during heat treatment can be found in the time-temperature-transformation (TTT) diagram for Inconel 625, as shown in Figure 2.2.

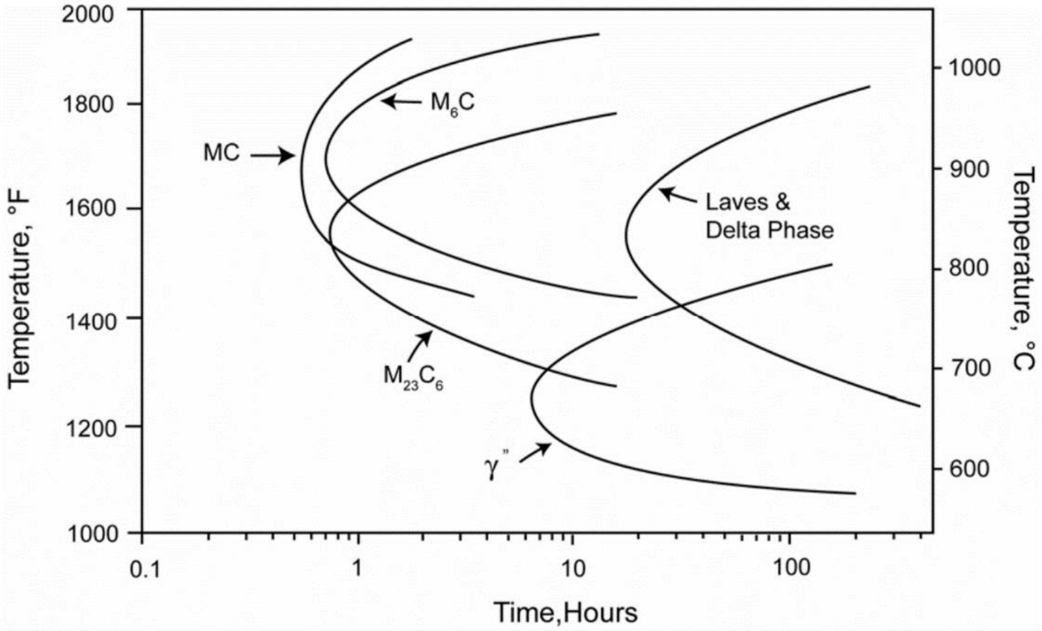

Figure 2.2: Time-Temperature-Transformation diagram for Inconel 625 that shows the phases formed at different times and temperatures. Figure taken from Shoemaker [2].

Annealing is a heat treatment that is designed to produce a fine, recrystallized grain structure in work hardened alloys [22]. The normal annealing range for Inconel 625 is between 871°C and 982°C, with a soaking time in the order of a few hours [2]. This leads to the fine precipitation of all three types of carbides, as can be seen from the TTT-diagram. Components made by the annealing process are intended for service up to 593°C.

Solution annealing is a high temperature heat treatment that yield components intended for service above 593°C. The minimum required temperature for the process is 1093°C, but higher temperatures are often used [2]. This will give a coarse grain structure where all carbides are put in solid solution, thereby enhancing the alloy’s resistance to creep and rupture at high temperatures.

By heat treating Inconel 625 components with a Nb content above 4% in the 649°C to 871°C temperature range, fine γ" particles can precipitate in the matrix [2]. This process is called precipitation hardening, and is used when increased strength is desirable. At these temperatures, carbides will form as precipitates in the matrix and on the grain boundaries. Precipitation hardening requires a longer soaking time than the two previously mentioned heat treatments, being in the order of ten hours.

2.4 Cold working

Cold working is the process where a ductile material becomes stronger and harder when it is plastically deformed [12]. During plastic deformation, the dislocation density in a metal will increase as a result of dislocation multiplication and the formation of new dislocations. Since dislocation-dislocation interactions are repulsive, the resulting decrease in the average distance between dislocations will act as a barrier against dislocation movement. As the degree of cold working increases, the stress necessary for dislocation movement, i.e. to deform a metal, will therefore increase [12]. CW materials are also strengthened by the introduction of sub-grains, which will decrease the effective grain size of the material [23]. This will increase the strength because of the Hall-Petch relationship, as described in Section 2.2. The result of the cold working is a highly deformed microstructure with oblong grains in the longitudinal direction, i.e. the direction of the deformation. Cold working is also known as work hardening or strain hardening.

The effect of cold working on the hydrogen embrittlement susceptibility of nickel alloys has been studied to some degree in the literature. El Kebir and Szummer found that the ductility decreased with an increasing degree of cold working for nickel samples charged with hydrogen [24]. Similar results were obtained by Pound, who found that the resistance of Alloy C-276 to HE decreased with an increasing amount of CW [25]. The increased susceptibility to HE is believed to be the result of an increased solubility of hydrogen due to trapping at dislocations introduced by the cold working [25]. This assumption has been supported by other research [26, 27]. Another factor influencing the susceptibility to hydrogen embrittlement is the increased amount of deformation slips found on the surface of CW samples. These slips are favorable sites for hydrogen adsorption, which will increase the hydrogen concentration in the sample, thereby increasing the susceptibility to HE [28]. The effect of CW on the strength of nickel alloys has been documented to a lesser degree than that of the ductility. However, Kane et al. found that the strength of CW nickel alloys charged with hydrogen depended greatly on the direction of loading [29]. Specimens loaded in the transverse direction, i.e. the direction where the distance between the grains is shortest, failed at much lower stresses than samples loaded in the longitudinal direction. In the longitudinal direction, the specimens did not fail, even under severe test conditions [29].

2.5 Hot isostatic pressing

Powder metallurgy (PM) has become an increasingly common technique for processing highly alloyed materials, such as nickel base superalloys. One such method is hot isostatic pressing (HIP), where a metal component is made by simultaneously applying high temperature and pressure to a metal powder [30]. An isostatic pressure is applied by an inert gas, making it possible to achieve fully isotropic properties in the material [31]. Normal HIPing temperature and pressure for nickel-base superalloys are 1100-1280°C and 100-140 MPa, respectively [32]. The HIPing process has several advantages compared to normal casting, the most notable being the removal of porosity and the effect on grain size.

Pores in metals can form in several ways, e.g. by packing of powder particles, from gas evolution or shrinkage during the solidification of castings, from the agglomeration of vacancies and by interdiffusion during the bonding of dissimilar metals [32]. These pores are stabilized by their surface energy and by the internal pressure if gas is present inside them. When HIPing is applied to a metal, the high pressure used will exceed the energy of the pores, thereby collapsing them. Any gas present in the pores will then be dissolved in the matrix. The removal of porosity results in a dense material with increased mechanical properties [32].

By using rapidly solidified, pre-alloyed powders with fine size fractions in the HIPing process, it is possible to produce metal components with small grains [33]. This is further enhanced by the high pressure used in the process, as it allows for the utilization of lower times and temperatures. When a metal is exposed to high temperatures, the grain boundaries will start to migrate, which will result in bigger grains. Minimizing the time and temperature used will therefore hinder excessive grain growth, allowing the material to retain the high strength and toughness associated with a small grain size.

2.6 Fracture mechanics

Fracture in metals are classified as either ductile or brittle, depending on the amount of plastic deformation exhibited. A ductile fracture is accompanied by substantial plastic deformation and high energy absorption. Brittle fractures, on the other hand, shows little or no plastic deformation and has low energy absorption [12]. The difference between a ductile and a brittle fracture is illustrated in Figure 2.3 [12]. Brittle fracture is most common in BCC and HCP metals, but can be found in FCC metals under certain conditions as well [6].

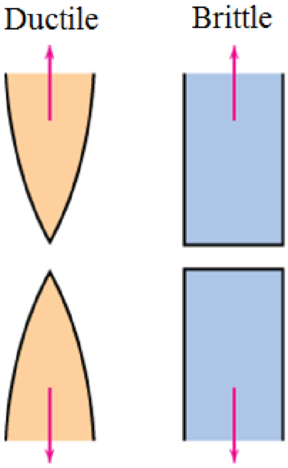

Figure 2.3: Illustration of a ductile fracture to the left and a brittle fracture to the right. Picture taken from Callister [12].

The most common type of tensile fracture for ductile metals is the cup-and cone fracture. During plastic deformation the metal will first experience necking, resulting in a reduction of the cross section area. Small cavities, or microvoids, will then start to form in the interior of this section. The voids nucleate at inclusions and second-phase particles by either interface decohesion or particle cracking. As the deformation continues, the voids will grow and coalesce with adjacent voids, resulting in the formation of an elliptical crack with its long axe perpendicular to the applied stress. The crack then continues to grow perpendicular to the applied stress by continued microvoid coalescence. Finally, fracture occurs by the rapid propagation of a crack around the other perimeter of the neck. The crack has a 45° angle with the applied stress, as this is the direction of maximum shear stress, giving the characteristic cup-and-cone appearance [12]. Macroscopically, ductile fractures has an irregular and fibrous appearance. The stages of the cup-and-cone fracture is shown in Figure 2.4, a through e.

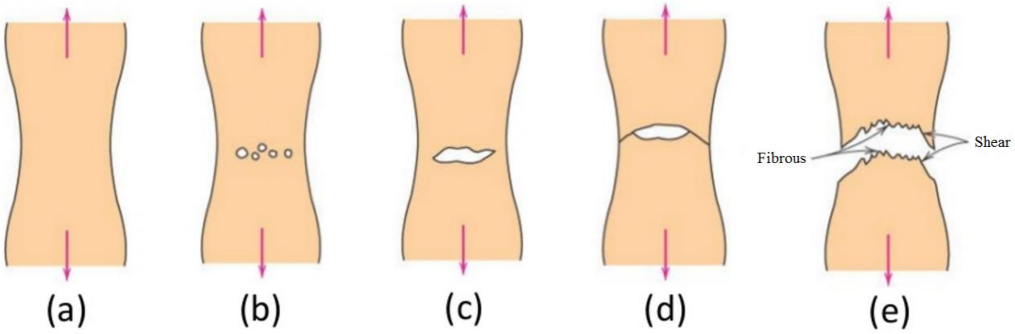

Figure 2.4: Stages of the ductile cup-and-cone fracture with a) necking, b) microvoid formation, c) microvoid coalesce, d) crack propagation and e) final shear fracture. Figure taken from Callister [12].

Brittle fracture can be subdivided into two different mechanisms: cleavage fracture and intergranular fracture. Cleavage fracture is the most common brittle fracture mechanism and is defined as the rapid propagation of a crack along a particular crystallographic plane, where the crack propagation involves the repeated breaking of atomic bonds [6]. To initiate a cleavage fracture, there must first be a local stress concentration that exceeds the bond strength of the material. This can be achieved through the formation of microcracks. These cracks can form either by dislocation pile-up at grain boundaries or by the cracking of carbides and second-phase particles. After a microcrack is formed, it can propagate into the metal matrix if the stress is sufficient, thereby causing a cleavage fracture. The crack plane is normally the plane with the lowest packing density, since this requires fewest bonds to be broken, while the direction of the cracking is nearly perpendicular to the applied stress. At a macroscopic level, the fracture surface has a grainy texture. Cleavage fracture is also called transgranular fracture, since the fracture cracks passes through the grains. Hicks and Altstetter found that slow strain-rate testing of Inconel 625 charged with hydrogen led to brittle, transgranular fracture [34].

Intergranular fracture occurs when cracks propagate along the grain boundaries. This mechanism usually follows the occurrence of a process that weaken or embrittle grain boundary regions, such as precipitation of a brittle phase on the grain boundary, environmental assisted cracking, intergranular corrosion, and grain boundary cavitation and cracking at high temperatures [6]. Martin et.al showed for instance that nickel can experience intergranular fracture if it is charged with hydrogen [35]. However, since there are several different situations that can lead to intergranular fracture, there is no single mechanism for the fracture process.

2.7 Fractography

Fractography is the detailed study of fracture surfaces by microscopy to identify which fracture mechanism has occurred [12]. In these studies, the scanning electron microscope is usually preferred to the optical microscope, since it has better resolution and depth of field. When the ductile cup-and cone fracture is examined in SEM, it will show several spherical “dimples”. These dimples are each one-half of a microvoid that formed during the plastic deformation. This is shown in Figure 2.5. Since cleavage fractures follow certain crystallographic planes, they can be identified by “river patterns”, as shown in Figure 2.6. Intergranular fractures propagate along the grain boundaries and will give a faceted surface where the three-dimensional nature of the grains can be seen. This is shown in Figure 2.7.

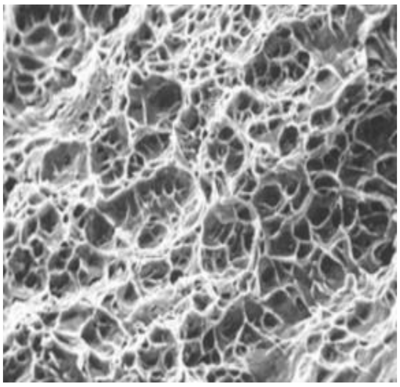

Figure 2.5: Ductile fracture showing dimples. Picture taken from Callister[12] .

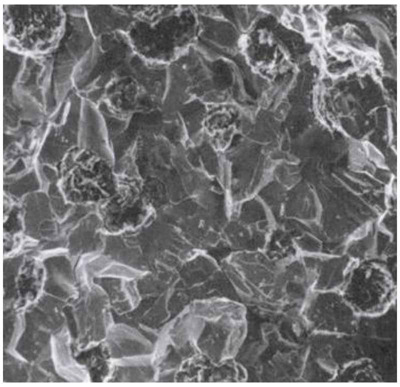

Figure 2.6: Cleavage fracture showing "river patterns". Picture taken from Callister [12].

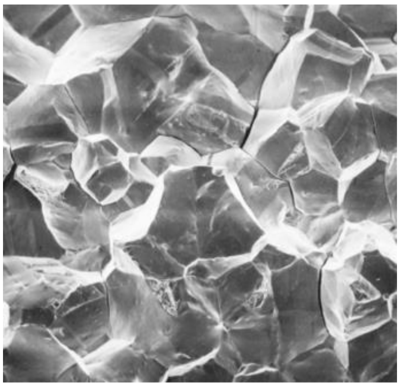

Figure 2.7: Intergranular fracture showing a faceted surface. Picture taken from Callister [12].

2.8 Diffusion of hydrogen

Since hydrogen atoms are small compared to most metallic atoms, they can readily diffuse between and occupy interstitial lattice sites in the metal matrix. The rate of diffusion depends strongly on the crystal structure of the metal, where BCC metals normally have diffusion rates several orders of magnitude higher than FCC metals [36]. This is because BCC metals have a lower packing factor than FCC, making it easier for hydrogen to move through the metal. The size of the interstitial sites are, however, larger in FCC metals, making them able to store more hydrogen than BCC metals. During diffusion, hydrogen can also be trapped at various other sites, including vacancy clusters, grain boundaries, dislocations, voids, internal cracks, precipitates and inclusions [36]. For instance, research done by Pound indicates that the main irreversible hydrogen traps in Inconel 625 are (Nb,Ti)C particles [25].

Steady-state diffusion of hydrogen can be described by Fick’s first law, which shows that the direction of diffusion is from high to low concentrations [12]:

$$J = -D \frac{dC}{dx} \tag{2}$$

Where J is the diffusion flux, D is the diffusion coefficient and dC/dx is the concentration gradient. For nonsteady-state diffusion, i.e. when the diffusion flux and the concentration gradient vary with time, Fick’s second law applies [12]:

$$\frac{\partial C}{\partial t} = D \frac{\partial^2 C}{\partial x^2} \tag{3}$$

Where $\partial C/\partial t$ is the time dependent concentration gradient. If the initial concentration of hydrogen in the solid is C_0, the diffusion length (x) is zero at the surface and the time (t) is zero when the diffusion process begins, Equation 3 can be expressed as [12]:

$$\frac{C_{x,t}-C_0}{C_s-C_0} = 1 - \mathrm{erf}\left(\frac{x}{2\sqrt{Dt}}\right) \tag{4}$$

Where $C_{x,t}$ is the concentration at point x, C_s is the surface concentration and erf is the Gaussian error function. One of the factors influencing the diffusion rate in metals is the temperature, where increased temperature gives increased diffusion rate. The temperature dependence of the diffusion coefficient is given by an Arrhenius equation [12]:

$$D = D_0 \exp\left(-\frac{Q_d}{RT}\right) \tag{5}$$

Where D_0 is a temperature independent pre-exponential, Q_d is the activation energy, R is the gas constant and T is the absolute temperature [12]. The effect of temperature on hydrogen diffusion is often used in post-processing treatments, where the metal is heated for some time in a hydrogen free atmosphere to get rid of residual hydrogen. Another factor influencing the diffusivity of hydrogen in metals is the level of stress. It has been found that stress in a metal will increase the diffusion rate of hydrogen, as hydrogen tends to diffuse to regions of high stress [37, 38]. The diffusion rate of Inconel 625 at 25°C was found by Pound to be $D = 2.2\times10^{-11}$ cm^2 s^{-1} [39].

2.9 Hydrogen embrittlement

When atomic hydrogen is introduced into a susceptible metal, it may severely damage the mechanical properties of the material. This process is known as hydrogen embrittlement and can lead to a reduction of both strength and ductility. Ductile metals affected by HE can also show a transition from ductile to brittle fracture. Hydrogen embrittlement was previously thought to affect only BCC and HCP metals, but is now know to affect most alloy systems, including austenitic and ferritic steel, titanium, aluminum and nickel-base alloys [6].

Hydrogen embrittlement can appear in several ways, including hydrogen induced cracking (HIC) and hydrogen induced stress cracking (HISC). In HIC, hydrogen atoms diffuse into the metal and accumulate in structural defects, such as inclusions, dislocations and microvoids [40]. When the hydrogen pressure reaches a critical value, the metal will blister and crack. This mechanism does not require an applied stress. HISC, on the other hand, is the process where a metal fractures due to the combined effect of hydrogen in the material and an applied stress. The criterion for HISC to occur is a hydrogen source, an applied stress and a susceptible material [41].

Crack propagation due to hydrogen embrittlement is often divided into two categories, depending on how hydrogen enters the material. In hydrogen-environment-assisted cracking (HEAC), hydrogen enters the material during use, e.g. by cathodic protection. If the hydrogen is introduced into the metal during manufacturing, e.g. by heat treatment, welding, casting etc., the process is called internal-hydrogen-assisted cracking (IHAC) [42]. The mechanism for both types of crack propagation is assumed to be the same. Because of the high local stress near a crack tip, the crystal lattice will expand, which increases the hydrogen solubility locally. This causes embrittlement of the zone around the crack tip, which combined with the high local stress will result in the formation of microcracks ahead of the initial crack tip. Over time, the microcrack will merge with the initial crack, resulting in crack growth. The crack will then continue to grow by repeated microcrack formation and coalesce [6].

Hydrogen embrittlement in Inconel 625 has been studied to some extent in the literature. Hicks and Altstetter found that slow strain-rate tests on Inconel 625 exposed to hydrogen resulted in a reduction of strength, ductility and reduction of area (RA) [34]. Similar observations were done by Takai et al., who showed that charging Inconel 625 with hydrogen gave a marked loss of strength and ductility [43]. During the literature review done as a part of this project, searches were also made on HISC-related failure cases of Inconel 625. Unfortunately, no information was found on the subject.

2.10 Hydrogen embrittlement mechanisms

The mechanism for hydrogen embrittlement has been widely discussed and has not yet been fully understood. There are several proposed mechanisms in the literature, where the most recognized are: Hydrogen-Enhanced Decohesion (HEDE), Hydrogen-Enhanced Localized Plasticity (HELP), Absorption-Induced Dislocation Emission (AIDE) and a mechanism based on the formation of hydrides.

The hydrogen-enhanced decohesion model is based on the assumption that high, localized hydrogen concentrations ahead of a crack tip will weaken the metallic bonds [44]. If the reduction of the cohesive energy in the metal matrix is sufficiently large, tensile separation of atoms (decohesion) will occur in preference to slip. The weakening of metallic bonds is attributed to the decrease in electron-charge density between metal atoms, due to the presence of hydrogen. This is illustrated in Figure 2.8. The high hydrogen concentration is a result of the increased hydrogen solubility in regions of high stress, as is the case close to the crack tip. The validity of the HEDE model has been supported by the measurement of high hydrogen concentrations at grain boundaries and particle-matrix interphases, as well as by quantum mechanical calculations [36]. Direct experimental evidence has nevertheless been hard to obtain, as there is no direct technique to observe atomistic events in a bulk material.

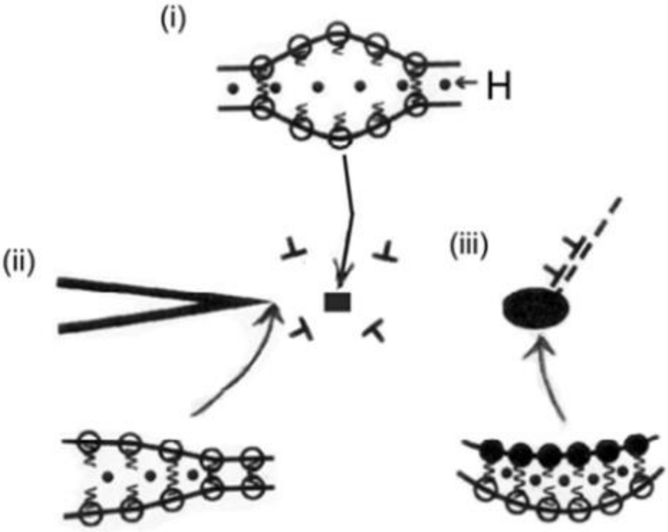

Figure 2.8: Illustration of the HEDE mechanism showing tensile separation of atoms due to weakening of atomic bonds by: (i) hydrogen in the lattice, (ii) adsorbed hydrogen and (iii) hydrogen at particle/matrix interface. Figure taken from Lynch [44].

Hydrogen-enhanced localized plasticity is a model that introduces a completely different view on hydrogen embrittlement. Here it is postulated that hydrogen shields dislocations from interacting with obstacles to dislocation movement, e.g. other dislocations, solute atoms, etc. The result is that resistance to dislocation movement is reduced and dislocation velocities are increased [44, 45]. Because of the increased dislocation movement and the shielding effect, more dislocations can pile up at grain boundaries. This will create regions with localized high deformation and softening of the metal ahead of the crack tip. As a result, localized cracking by microvoid formation and coalesce will occur. On a macroscopic scale, the fracture will still be perceived as brittle [45]. The main supporting evidence for HELP is in situ transmission electron microscopy (TEM), where it has been shown that metal samples exposed to hydrogen have an increased number of dislocations in a pile-up, as well as increased dislocation movement [45]. However, the experimental method has been subject to some debate, as the thin foil used in TEM may not be representative for a normal bulk material. The HELP mechanism is illustrated in Figure 2.9.

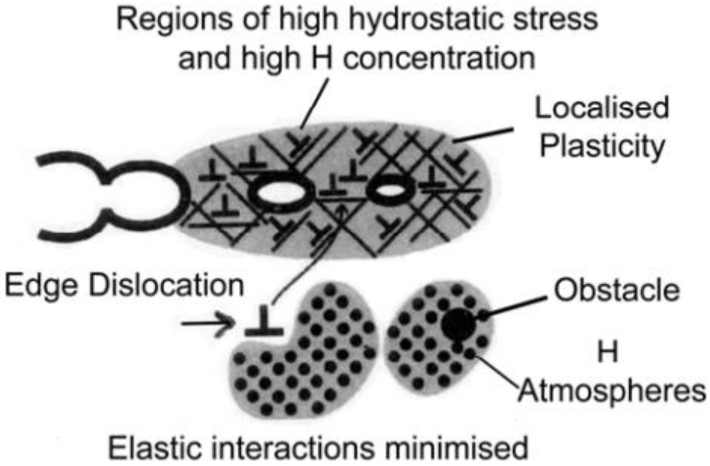

Figure 2.9: Illustration of the HELP mechanism, with microvoid formation and coalescence in regions of localized plasticity due to high hydrogen concentrations. Figure taken from Lynch [44].

Absorption-induced dislocation emission is best understood as a combination of the HEDE and HELP models. The mechanism for this model is based on the weakening of atomic bonds by hydrogen, like in the HEDE model, but with crack growth occurring by localized slip, as is the case in the HELP model [44]. Here it is proposed that when hydrogen absorbs at a crack tip and weakens the metallic bonds, the nucleation of dislocations is facilitated. Dislocations can then move ahead of the crack tip and lead to the formation of microvoids by plastic deformation, as previously explained. Supporting evidence for this theory is based on a combination of the evidence for the two other models.

The hydride forming model is based on the stress induced formation and cleavage of hydrides ahead of a crack tip [45]. It is believed that the mechanism involves hydrogen diffusion to crack tips under the influence of a stress gradient, nucleation and growth of a hydride phase, cleavage of hydride phase and crack-arrest at the hydride-matrix interface [36]. Since the hydrides formed are brittle, the resulting fracture will also be brittle. The hydride forming mechanism has been well documented by TEM-studies, and is generally accepted for typical hydride forming elements, i.e. V, Zr, Nb, Ta and Ti [45].

2.11 Effect of grain size on hydrogen embrittlement

The increased resistance to hydrogen embrittlement by decreasing the grain size in steel has been well documented [46-48]. This is not the case for nickel alloys, which have shown conflicting results on the topic. Sjöberg and Cornu showed that fine-grained samples of Inconel 718 was more exposed to embrittlement by hydrogen than coarse-grained samples of the same material [49]. The increase in embrittlement was explained by grain boundary hydrogen sensitiveness. Similar experiments done by Knarbakk showed that hydrogen led to a higher reduction of ductility for coarse-grained samples of Inconel 718 compared to fine-grained samples of the same alloy. However, these results were not supported by the fracture values, as the fine-grained samples showed a higher reduction in fracture strength than the coarse-grained samples when charged with hydrogen [8].

Contradicting results were obtained by Gray, who found that the HE susceptibility of Udimet 700 decreased with decreasing grain size [50]. Latanision and Opperhauser obtained similar results when charging polycrystalline nickel with hydrogen, which showed that a larger grain size resulted in both reduced fracture stress and ductility [51]. Because of the contradicting results on the effect of grain size on hydrogen embrittlement in nickel alloys, no conclusion is reached on the topic yet.

2.12 Hydrogen evolution by cathodic protection

Cathodic protection (CP) is the process where a metal is protected from corrosion by making it the cathode in an electrochemical cell. This can be done in two ways, either by connecting the metal to a sacrificial anode, which will corrode instead of the protected metal, or by an impressed current (I) that will lower the potential (E) of the metal into the immune area of the Pourbaix diagram [52]. An example of a Pourbaix diagram for an imaginary metal is given in Figure 2.10. In the active regions of the diagram, the metal will corrode, while corrosion is thermodynamically impossible in the immune region. In the passive region, a protective oxide will form on the metal surface, making electrochemical reactions go slowly.

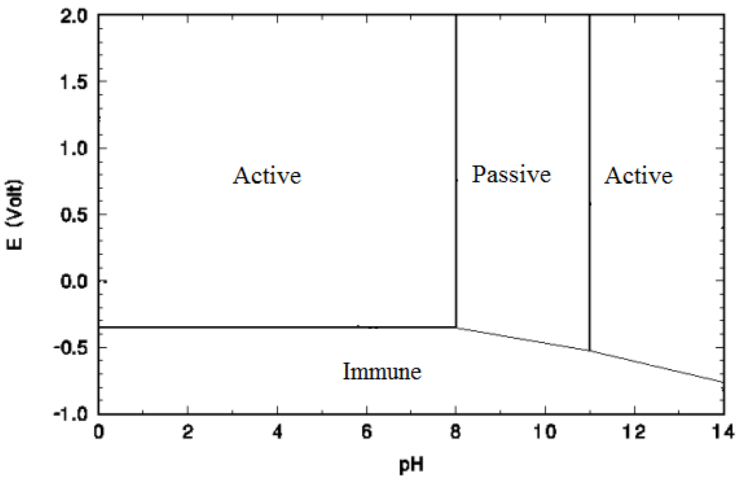

Figure 2.10: Pourbaix diagram for imaginary metal, where E is the potential. The metal will corrode in the active region, while corrosion will not occur in the immune area. In the passive area, a protective film will form such that electrochemical reactions go slowly. Figure taken from Talbot [5]

When CP is applied to a metal in seawater, two possible reactions can lead to the formation of atomic hydrogen [53]:

$$H_2O + e^- + ss \leftrightarrow H_{ads} + OH^- \tag{6}$$

$$H^+_{aq} + e^- + ss \leftrightarrow H_{ads} \tag{7}$$

Where ss is a surface site available for hydrogen adsorption. Hydrogen capable of diffusing into the metal is then produced by chemisorption on the metal surface. Chemisorption is an adsorption process that involves the chemical reaction between surface and adsorbate [54]. The process where hydrogen goes from being adsorbed to being absorbed can be expressed by Equation 8 [53]:

$$H_{ads} \leftrightarrow H_{abs} \tag{8}$$

Hydrogen adsorbed at the surface can alternatively leave the metal instead of being further absorbed. This happens when hydrogen recombines to form gaseous H_2 in accordance with Equation 9 and 10 [53]:

$$H^+ + H_{ads} + e^- \leftrightarrow H_2 + ss \tag{9}$$

$$H_2O + H_{ads} + e^- \leftrightarrow H_2 + OH^- + ss \tag{10}$$

The rate at which hydrogen is evolved at a surface is most easily obtained through an Evans diagram, as illustrated in Figure 2.11. This diagram gives the correlation between the potential and the current for the possible electrochemical reactions [5]. The corrosion potential (E_{corr}), and current (I_{corr}), for the metal M can be found at point B, where the lines for the oxygen reduction reaction and the metal oxidation reactions meet. Since the current at this point is relatively high, the rate of metal oxidation will also be high. By impressing a current on the metal, the potential can be reduced to the protection potential (E_{prot}), thereby reducing the rate of metal oxidation, see point A in Figure 2.11. As the potential is lowered, the hydrogen evolution reaction becomes the increasingly dominant reduction reaction, with the corresponding increase in reaction rate [29]. As a result, CP of a metal component will act as a continuous source for hydrogen.

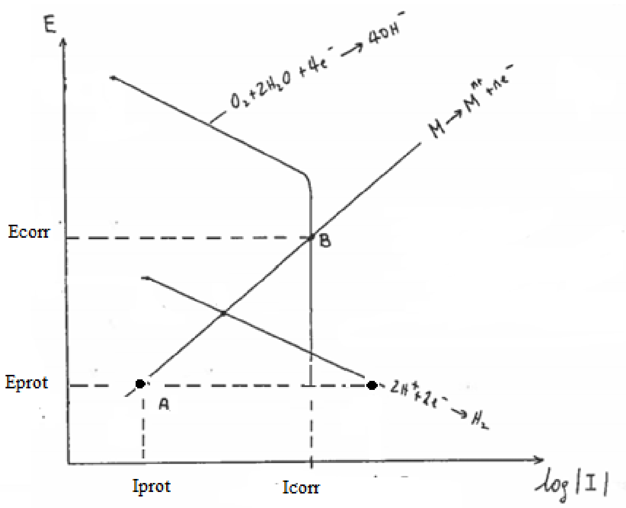

Figure 2.11: Evans diagram for the hypothetical metal M, where E is the potential and I is the current. At point B the metal corrodes, while at point A the metal is protected and corrosion rates are slow. Slightly modified version of Evans diagram as given by Schweitzer [55].

Cathodic protection is normally not needed for components made of Inconel 625, as they are resistant to corrosion in seawater up to 30°C [4]. However, metallic contact with metals in need of such protection will cause the Inconel 625 components to be protected as well, thereby allowing hydrogen to be evolved at the surface.

When measuring the potential of an electrochemical cell, it is actually a potential difference that is observed. As a result, different reference electrodes will show different potentials for the same reaction. By using a conversion chart, the potential value shown by one reference electrode can be converted into the corresponding potential of another reference electrode. Such a conversion chart is given in Table 2.1. Here the conversion between an Ag/AgCl reference electrode and an $Hg/HgSO_4$ reference electrode is given [52].

Table 2.1: Conversion chart between Ag/AgCl and $Hg/HgSO_4$ reference electrodes, where E is the potential.

Reference electrode	E vs Ag/AgCl [mV]	E corresponding to -1050 $mV_{Ag/AgCl}$ [mV]
Ag/AgCl	0	-1050
$Hg/HgSO_4$	-456	-1506

3 Experimental

3.1 Material

Two versions of the same Inconel 625 were tested in this study. Both versions were of forged quality, but subjected to different heat treatments. These samples will hereafter be referred to as F1010 and F1100, indicating forged samples heat treated at 1010°C and 1100°C, respectively. To get a broader basis for evaluating the HISC susceptibility of Inconel 625, the findings from the author's previous work will also be presented. The materials investigated in the previous work was one forged quality heat treated at 920°C and one HIPed quality heat treated at 920°C. These samples will hereafter be referred to as F920 and H920, respectively. Finally, the results from a parallel experiment on a cold worked Inconel 625 sample performed by Erlend Haugsnes at NTNU the same semester will also be presented. This sample will hereafter be referred to as C1150, indicating a cold worked sample heat treated at 1150°C. Unless otherwise specified, the experimental procedures for H920, F920 and C1150 are identical with the ones described in the following sections, but performed by the author during the 9th semester project or in Erlend Haugsnes' MSc.

The manufacturer VDM [56] supplied F920, Kennametal [57] supplied H920 and ATI [58] supplied C1150. The chemical compositions of the different versions of Inconel 625 are given in Table 3.1, where Bal. is balance, i.e. the remaining wt%. Since F1010 and F1100 were created by heat treating F920 samples, they have the same chemical composition.

Table 3.1: Chemical composition in weight percentage (wt%) for the five different versions of Inconel 625.

	Material		
	F920/F1010/F1100	**H920**	**C1150**
Element	**Wt. [%]**		
C	0.03	0.01	0.052
Si	0.13	0.04	0.03
Mn	0.05	0.06	0.03
S	<0.001	0.003	<0.0003
Cr	22.3	21.46	20.91
Mo	9.19	9.29	8.51
Ni	Bal.	Bal.	Bal.
Ti	0.32	<0.01	0.26
Fe	4.32	<0.01	4.61
P	0.004	0.002	0.006
Nb+Ta	3.43	3.46	3.32
Co	0.02	0.21	0.02
Al	0.026	0.03	0.26

Heat treatment and key properties of the three base materials, such as yield strength (YS), ultimate tensile strength (UTS), Rockwell hardness (HRC) and reduction of area (RA), were supplied in data sheets by VDM, Kennametal and ATI, and are listed in Table 3.2. The values for C1150 correspond to the metal in pre cold-worked condition. The degree of CW was 66%.

Table 3.2: Key mechanical properties plus heat treatment for the three base versions of Inconel 625, as supplied in datasheets by VDM, Kennametal and ATI. YS is yield strength, UTS is ultimate tensile strength, HRC is Rockwell hardness and RA is reduction of area.

Material	**YS (0.2%) [MPa]**	**UTS [MPa]**	**HRC (C-scale)**	**Grain size**	**Elongation [%]**	**RA [%]**	**Heat treatment**
F920	536	897	22	7	50	55	920°C for 1 hour + water quenching
H920	531.5	960	35 (max)	N/A	48,5	48,5	920 °C for 6.5 hours + water quenching
C1150	297	741	4	N/A	63.5	N/A	1150 °C for 3 hours + water quenching

3.2 Sample dimensions

Samples with three different geometries were used in this study, depending on the experiment performed. Figure 3.1 shows the dimensions of the sample used in the tensile test, while Figure 3.2 gives a picture of the same sample. Figure 3.3 and Figure 3.4 show the same things for the sample used in the HISC test. In Figure 3.5, the dimensions of the sample used in the OM, EDS, hardness test and modified ASTM G48 pitting test [59] are illustrated, while a picture of the sample is given in Figure 3.6.

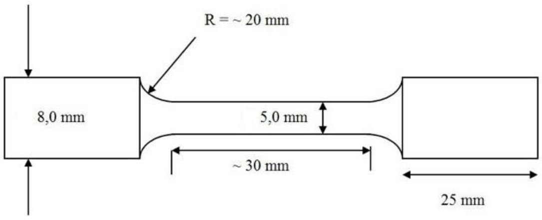

Figure 3.1: Dimensions for the tensile test samples.

Figure 3.2: Picture of sample used in the tensile test.

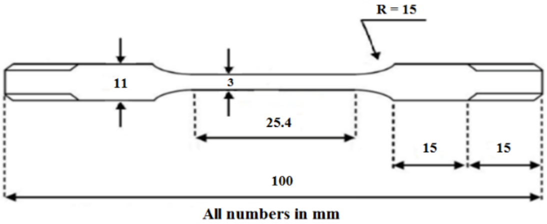

Figure 3.3: Dimensions for the HISC test sample.

Figure 3.4: Picture of the sample used in the HISC test.

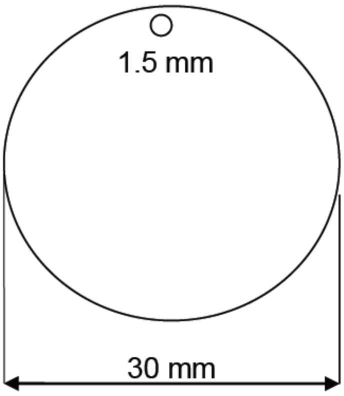

Figure 3.5: Dimensions for sample used in OM, EDS, hardness test and modified ASTM G48 test [59].

Figure 3.6: Picture of the sample used in OM, EDS, hardness test and modified ASTM G48 test.

3.3 Heat treatment

Two different heat treatments were performed in this study, one at 1010°C and one at 1100°C, resulting in the creation of F1010 and F1100. The basis for each heat treatment was thirteen F920 samples, where three had the geometry as shown in Figure 3.1, five as shown in Figure 3.3 and five as shown in Figure 3.5. To prevent high temperature oxidation of the samples during heat treatment, the samples were inserted into a steel box with an argon atmosphere, see Figure 3.7. The argon atmosphere was maintained by connecting the box to an argon 4.0 tank, which delivered an argon flow of 2.5 L/min. The box with the samples was then inserted into a Nabertherm N17 oven with a Nabertherm C290 program controller and heated to the desired temperature with the fastest possible heating rate. After the desired temperature had been reached, it was held for one hour, whereupon the samples were cooled with the fastest possible cooling rate inside the oven. When the samples had cooled to 600°C, they were removed from the oven and air-cooled to room temperature. The temperature inside the box was recorded using an Omega HH1384 Datalogger.

Figure 3.7: Box used during heat treatment to maintain an argon atmosphere.

During the heat treatment, a black oxide layer formed on the samples' surface, probably being the result of an insufficient argon atmosphere inside the box. This layer was removed by grinding the samples with 80, 120, 320, 800 and 1200 grit Struers SiC paper. The grinding was done by hand due to the geometry of the samples.

3.4 Stress-strain curves

The mechanical properties of F1010 and F1100 were tested in a 100kN MTS 810 Hydraulic tensile test machine. Three samples were used from both F1010 and F1100 to get representative values. Sample dimensions are shown in Figure 3.1. Each sample was first inserted into the tensile test machine and an extensometer was attached to the thin part of the sample. The sample was then loaded at a constant elongation rate of 2 mm/min until fracture. Stress-strain curves were recorded by connecting the tensile test machine to a computer with dedicated software. The experimental setup for measuring stress-strain curves is depicted in Figure 3.8.

Due to the high ductility of the F1100 samples, the extensometer was unable to measure the full elongation of these samples. This resulted in the incomplete recording of the elongation of the first F1100 sample. The problem was overcome for the other two F1100 samples by stopping the tensile test at 55% elongation, reattaching the extensometer, and then continuing the tensile test. To obtain conservative results, the sample with the lowest YS from each version of Inconel 625 was used as a basis for calculating the starting load in the subsequent HISC test.

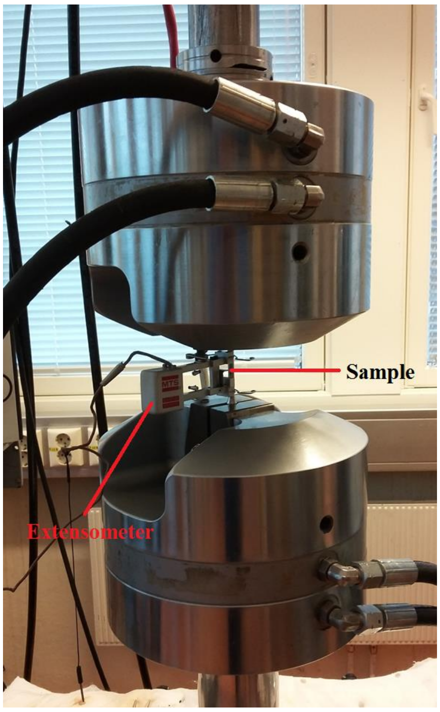

Figure 3.8: Test setup for the tensile test experiment

After fracture, the diameter of the samples were measured with a caliper to obtain the reduction of area. The RA was calculated according to Equation 11 [12]:

$$RA = \frac{A_0 - A}{A_0} = \frac{r_0^2 - r^2}{r_0^2} \tag{11}$$

Where A_0 is the initial area of the sample, A is the area of the sample after fracture, r_0 is the initial radius of the sample and r is the radius of the sample after fracture.

3.5 HISC-test

HISC testing was performed as a three-stage-process, with hydrogen pre-charging, constant loading and loading until fracture, as described in the subsequent chapters. The Cortest proof rings used in the loading phase were originally designed for sulfide stress cracking (SSC) tests [60], but was adapted to be used in HISC testing by connecting the rings to a potentiostat.

3.5.1 Hydrogen pre-charging

In the first part of the HISC test, four of the five HISC samples from F1010 and F1100 were pre-charged with hydrogen. The fifth sample was only exposed to air, and thus served as a reference sample for the hydrogen-exposed samples. Figure 3.3 gives the dimensions of the samples used in the HISC test. The electrolyte used for pre-charging was a 2:1 mix of glycerol and ortho-phosphoric acid (H_3PO_4). This electrolyte was chosen because similar work done by Knarbakk suggested that it was a more effective charging medium than 3.5 wt% NaCl [8]. The four samples from each parallel were bound together by a platinum wire and submerged into two separate 1000 mL glass containers with accompanying glass caps, as illustrated in Figure 3.9. Through the holes in the glass cap, a platinum counter electrode, an $Hg/HgSO_4$ reference electrode and the platinum wire holding the samples were inserted. The samples were then connected to a Wenking MP 04 mini-potentiostat. In addition to the electrodes, a heat sensor was also inserted through the glass cap to keep the temperature constant. An IKA C-MAG HP 7 hot plate was used to supply heat. When the experimental setup was finished, the potentiostat was turned on, polarizing the samples to -1506 $mV_{Hg/HgSO4}$ (see Table 2.1). Finally, the heat was turned on, elevating the temperature to 120°C. The pre-charging lasted for six days, during which the electrolyte was changed every second day, as it turned black.

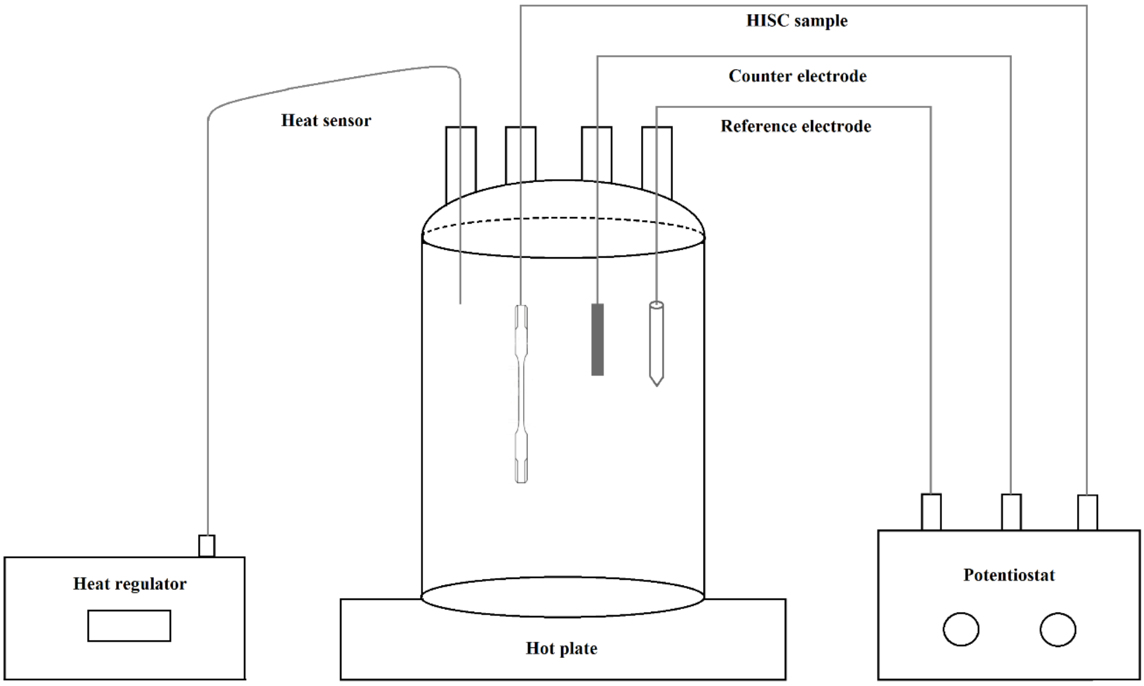

Figure 3.9: Illustration of experimental setup for the hydrogen pre-charging of the samples.

During the pre-charging period, it was noted that the F1100 samples showed periods of low hydrogen evolution. After four days, the potentiostat connected to F1100 stopped working, resulting in a loss of potential for somewhere between 0 and 20 hours (the exact time of malfunction is unknown, as it happened between two check-ups). The damaged potentiostat was replaced the following day with a Wenking MP 87 potentiostat. Because of the abovementioned problems with the hydrogen pre-charging of F1100, it was decided to increase the pre-charging period of these samples by two days. After pre-charging, the samples were stored in a freezer until the next part of the experiment was initiated. A picture of the experimental setup is given in Appendix A.

3.5.2 Constant load

In the second part of the experiment, the samples where moved to a different part of the laboratory for HISC testing in Cortest proof rings. Before the testing began, the initial diameters of the Cortest proof rings were measured with a caliper to obtain a basis for the subsequent loading. A 3.5 wt% NaCl solution was also made for use as an electrolyte. This was done by dissolving 70 g NaCl in 2000 mL of water. The reference samples were then mounted in the Cortest proof rings, as shown in Figure 3.10. These samples were only exposed to air. The remaining samples were submerged into the 3.5 wt% NaCl electrolyte in sealed, acrylic glass chambers, mounted in the Cortest proof rings and connected to a potentiostat, see Figure 3.11. The F1010 samples were connected to a Wenking MP 04 mini-potentiostat, while the F1100 samples were connected to a Wenking MP 87 potentiostat. The setup also contained counter electrodes made by platinum wire and Ag/AgCl reference electrodes. When the experiment was set up, the samples exposed to hydrogen pre-charging were polarized to -1050 $\mathrm{mV_{Ag/AgCl}}$, resulting in hydrogen evolution on the samples' surface. This was done to prevent hydrogen from diffusing out of the samples during loading. All the samples were then loaded to 100% of their YS by manually tightening the nut on top of the Cortest proof rings. This load was held for five days, during which the diameters of the rings were calibrated daily to account for creep. The diameter of the Cortest proof rings needed to reach the required load was calculated in Excel sheets supplied by the supervisor, where the input data was the initial diameter of the samples, the initial diameter of the ring and the lowest yield strength obtained in the tensile test for F1010 and F1100.

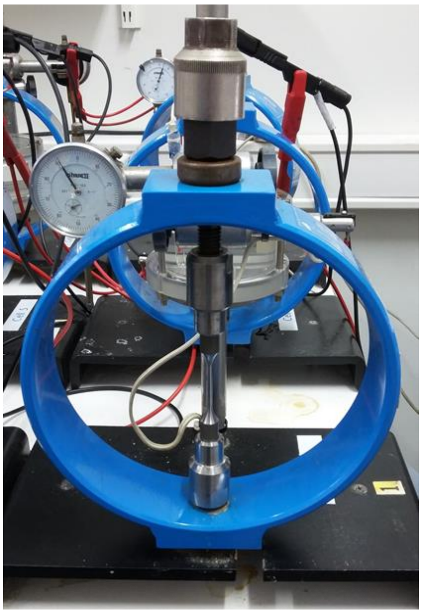

Figure 3.10: Picture of experimental setup for the stepwise loading in Cortest proof rings – reference sample.

Figure 3.11: Picture of experimental setup for the stepwise loading in Cortest proof rings - hydrogen exposed sample.

3.5.3 Increasing load until fracture

In the final phase of the experiment, the load was increased daily until fracture. Based on the values from the tensile test, F1100 was expected to fracture at a higher percentage of YS than F1010. The load was therefore increased by 8% of YS for seven days for F1100, while the load was increased by 8% of YS for five days for F1010. After that, the load was increased by 4% of YS each day until fracture for both materials. When a sample fractured, it was immediately removed from the Cortest proof rings, washed with distilled water and ethanol, and stored in a freezer. This was done to keep the samples clean for later SEM studies and to prevent hydrogen from diffusing out of the samples. When all the samples had fractured, the Cortest proof rings were calibrated with an AEP Transducers MP1 Basic load cell to obtain the real stress values. This was done by inserting the load cell into the Cortest rings, tighten the rings to the diameter at which the samples had previously fractured and measure the force at this point. The calibration setup is shown in Figure 3.12.

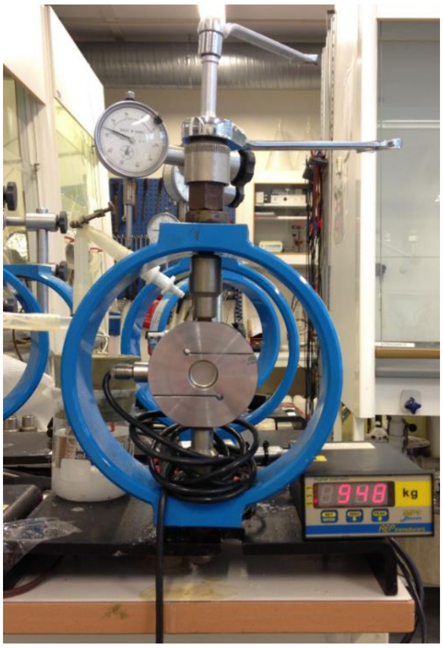

Figure 3.12: Setup for the Cortest ring calibration.

3.6 SEM of fracture surface

After the samples had fractured, the fracture surfaces were examined in a Zeiss Ultra 55 SE scanning electron microscope. The samples' sides were also examined to investigate any secondary cracking. The RA-values for the HISC samples were obtained by measuring the diameter of the fracture surfaces in the SEM and using Equation 11 from Section 3.4. Additionally, the reduction of reduction of area (RRA) for the samples charged with hydrogen in reference to the reference samples was also found. The RRA was calculated according to Equation 12 [12]:

$$RRA = 1 - \frac{RA_H}{RA_{ref}} \tag{12}$$

Where RA_H is the reduction of area for the samples charged with hydrogen and RA_{ref} is the reduction of area for the reference sample.

3.7 Characterization of microstructure by optical microscope

To be able to identify the microstructure and grain size, one sample from F1010 and one sample from F1100 were examined in an optical microscope. Sample dimensions are given in Figure 3.5. The microstructure was revealed by first grinding with 320, 500, 800, 1200 and 2400 grit Struers SiC paper on a Saphir 330 grinding machine, at a rotation speed of 200 rpm. For each new grit size, the sample was rotated 90° and ground until the abrasive strips from the previous grit size was gone. The samples were then polished with a 3µm and 1µm diamond suspension on a DP-U3 Struers polishing machine, using the same method as for the grinding. Because the abrasive strips were barely visible at this point, the samples had to be washed with ethanol and dried between the polishing steps to be able to confirm that the previous abrasive strips were gone. Finally, the samples were etched by immersion in Kalling's nr 2 for 3 minutes, in accordance with ASTM E407 – 07 [61]. To avoid the deposition of etching products on the sample surface, the samples had to be continuously swabbed with a piece of cotton during immersion.

After the etching, the samples were examined in a Leica MEF4M optical microscope at different magnifications, and the grain size was determined by Jeffries' procedure, in accordance with ASTM E112 - 13 [62].

3.8 EDS

Since the optical microscope revealed the existence of precipitates in F1010 and F1100, it was decided to investiate them further by energy dispersive spectroscopy (EDS). The samples previously used in the optical microscope were washed with ethanol and inserted into a FEI Quanta FEG 650 SEM with an EDAX X1 EDS analyser. Matrix precipitates and grain boundary precipitates were then analysed to reveal their chemical composition. H920, F920 and C1150 were also investigated by EDS, since this had not been previously done.

3.9 Hardness test

To obtain the hardness of F1010 and F1100, the two samples previously used in the optical microscope and the EDS were tested in a Vickers hardness (HV) test. The samples were prepared by grinding with 800 and 1200 grit Struers SiC paper, in the same way as described in Section 3.7. After grinding, the samples were inserted into a DKV-1S Matsuzawa Vickers hardness test machine. A load of 5 kg was used, with a loading time of 15 seconds and a loading speed of 100 µm/s. To obtain reliable results, ten measurements were done for each sample and the mean value was calculated. The values were then converted to HRC in accordance with ASTM E140 – 12b [63], to be able to compare them with the values given by the manufacturers.

3.10 Modified G48 pitting test

The critical pitting temperature was obtained for H920, F920, F1010 and F1100 by using a modified version of ASTM G48 [59]. Two samples from each material were used, with dimensions as shown in Figure 3.5. Before the testing began, each sample was weighed on a Mettler AT200 analytical balance to the nearest 0.0001 g. The electrolyte used in the experiment was then made by dissolving 100 g iron(III)-chloride hexahydrate ($FeCl_3 \cdot 6H_2O$) in 900 mL of distilled water, in accordance with ASTM G48 [59]. A 2000 mL glass beaker containing the electrolyte was then mounted on an IKA C-MAG HP 7 hot plate and a heat sensor and a salt bridge were inserted into the electrolyte. The salt bridge was used to secure the electrical connection between the electrolyte and an Ag/AgCl reference cell. Finally, the samples were connected to the Ag/AgCl reference electrode and a channel logging the open circuit potential (OCP), and submerged in the pre-heated electrolyte. The experimental setup is illustrated in Figure 3.13.

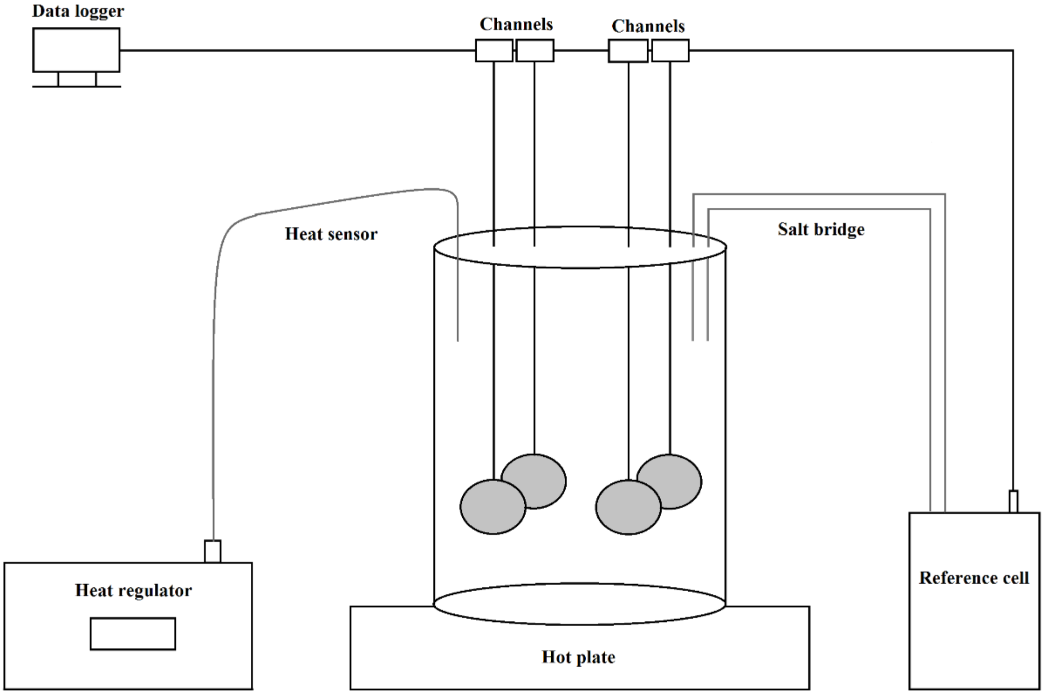

Figure 3.13: Illustration of the experimental setup for the modified ASTM G48 test.

The experiment was done twice, as only four samples could be tested at a time. In the first experiment, H920 and F920 were tested with a starting temperature of 40°C. Since these samples showed a high pitting temperature, it was decided to use 60°C as the starting temperature for F1010 and F1100. After one day at the initial temperature, the temperature was increased by 5°C each day. The experiment was stopped if the potential at any time dropped below 500 $mV_{Ag/AgCl}$ or if the potential was still above 500 $mV_{Ag/AgCl}$ after one day at 85°C. If the potential dropped below 500 $mV_{Ag/AgCl}$, pitting was considered to be initiated. This limit for pitting initiation is based on experience from co-supervisor Roy Johnsen. The 85°C limit is given in ASTM G48 as the maximum recommended value for testing in $FeCl_3$-solution [59]. After testing, the samples were removed from the solution, cleaned with distilled water and ethanol and weighed again at the Mettler AT200 analytical balance to the nearest 0.0001 g. Finally, the samples were examined in a Leica MEF4M optical microscope to see if any pits were visible. The modified ASTM G48 was not performed on C1150, since no samples with the right dimensions were available. A picture of the experimental setup is given in Appendix A.

3.11 Hydrogen measurements

One hydrogen charged sample from each version of Inconel 625 was sent to SINTEF for hydrogen measurements. The hydrogen measurements were done on the thin part of the hydrogen charged HISC samples, as shown in Figure 3.3. A description of the analyzing method given by SINTEF is shown in Appendix B.

4 Results

4.1 Heat treatment

Figure 4.1 shows the heat treatment of F1010 and F1100. After cooling down to 600°C, the samples were removed from the oven and cooled in air. At this point, the cooling rate was no longer recorded, but is instead depicted as an instantaneous temperature change to room temperature. Because of the thin diameter of the samples, this approximation is considered valid.

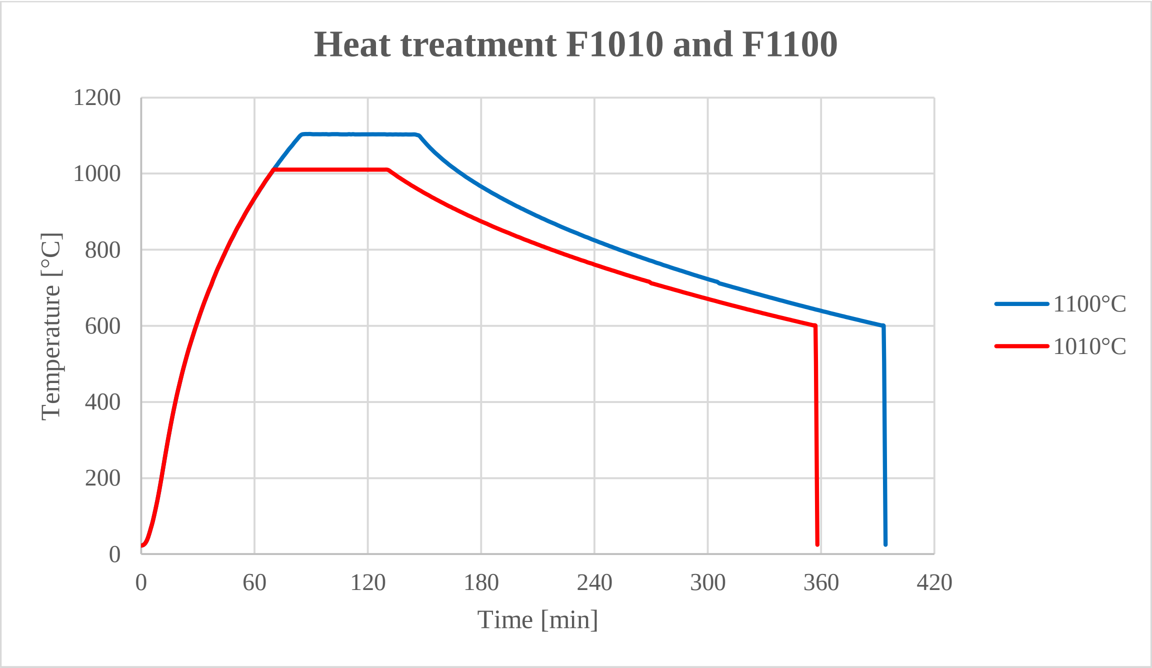

Figure 4.1: Heat treatment of F1010 and F1100.

4.2 Tensile test

Figure 4.2 shows the stress-strain curves obtained from the tensile test for the samples with the lowest YS for each version of Inconel 625. Apart from C1150, the curves show a decrease in strength and an increase in ductility with increasing heat treatment, which is in agreement with the fact that a higher heat treatment will result in bigger grains [12]. The grain size for the different versions of Inconel 625 is given in Section 4.3.1. C1150 shows higher strength and lower ductility than the other samples, which is in agreement with the cold working process [12].

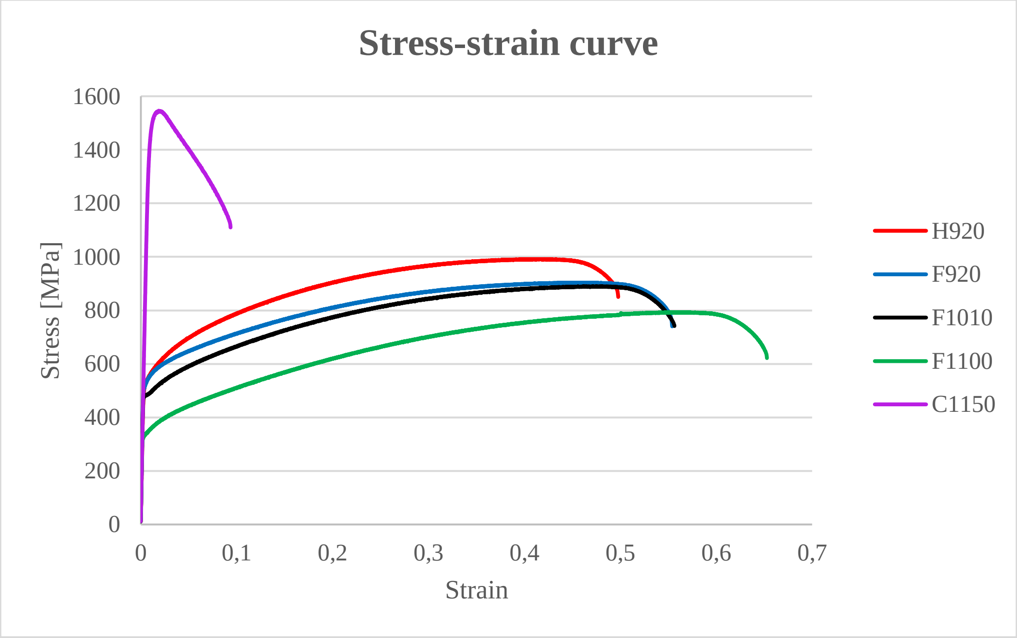

Figure 4.2: Stress-strain curves for the different versions of Inconel 625, measured in mega pascal (MPa). The curves correspond to the samples with the lowest yield strength (YS).

The key mechanical properties from the tensile test are given in Table 4.1. The results for H920 and F920 correspond well with the values supplied by the manufacturers, as given in Table 3.2. Since the values for C1150 in Table 3.2 are given in the pre-cold worked condition, these values cannot be directly compared to the values from the tensile test. Note that the strain was not found for F1100 sample number one, as the extensometer maxed out at 55%

Table 4.1: Key mechanical properties obtained from the tensile test for the different versions of Inconel 625. YS is yield strength, UTS is ultimate tensile strength, RA is reduction of area and N/A is not available.

Material	Sample number	YS (0.2%) [MPa]	UTS [MPa]	UTS/YS [%]	Strain [%]	RA [%]	Average RA [%]
H920	1	536.1	991.1	184.9	48.1	50.2	51.1
	2	533.6	990.0	185.5	48.5	52.4	
	3	529.0	991.8	187.5	49.8	50.8	
F920	1	525.8	908.0	172.7	55.6	52.5	54.0
	2	531.9	909.8	171.0	54.6	55.0	
	3	519.2	903.8	174.1	55.4	54.6	
F1010	1	492.3	896.2	182.0	57.4	58.7	58.9
	2	483.9	891.7	184.3	56.5	60.2	
	3	481.4	890.3	184.9	55.6	57.8	
F1100	1	413.2	802.1	194.1	N/A	61.6	60.9
	2	409.2	793.3	193.9	65.3	60.4	
	3	416.2	799.6	192.1	64.9	60.7	
C1150	1	1450.0	1546.3	106.6	9.3	48.3	49.6
	2	1430.0	1539.4	107.7	9.1	49.4	
	3	1452.0	1556.3	107.2	9.2	51.2	

4.3 Characterization of microstructure by optical microscope

4.3.1 Microstructure

Figures 4.3-4.6 show microstructural images obtained by optical microscopy at 20X magnification for the forged and the HIPed versions of Inconel 625. Even though several etching procedures were performed on C1150, it was not possible to obtain decent microstructural images. It was therefore decided to use a microstructural image given by the supplier ATI. This is shown in Figure 4.7.

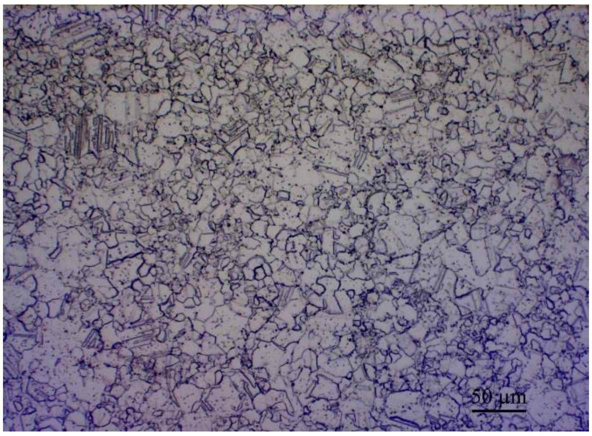

Figure 4.3: Microstructure of H920 at 20X magnification.

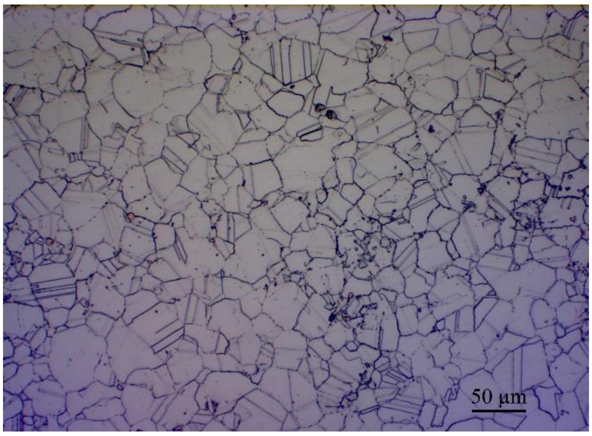

Figure 4.4: Microstructure of F920 at 20X magnification.

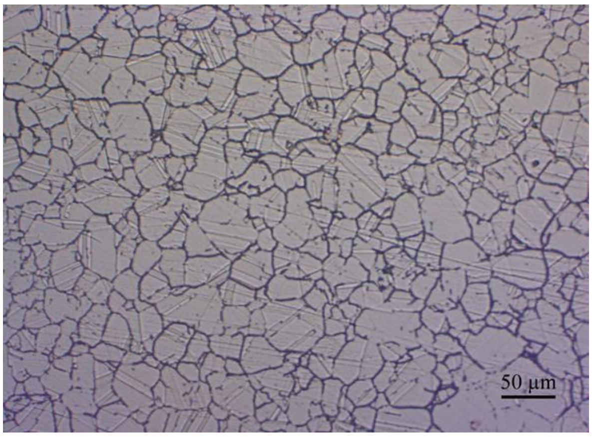

Figure 4.5: Microstructure of F1010 at 20X magnification.

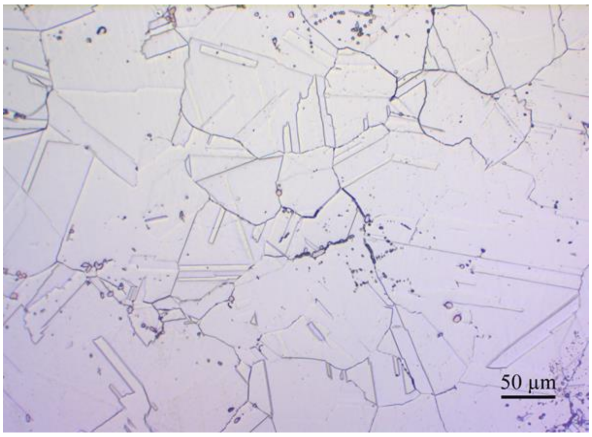

Figure 4.6: Microstructure of F1100 at 20X magnification.

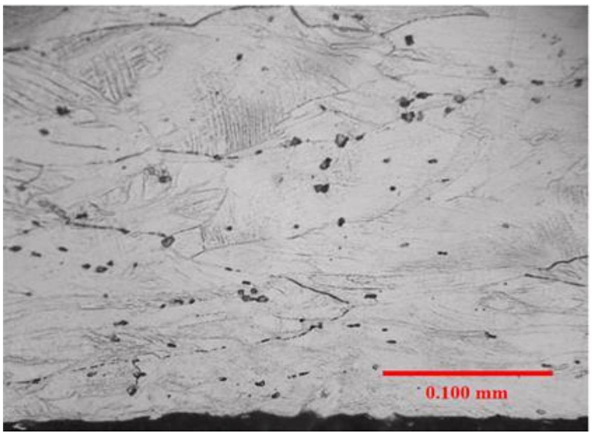

Figure 4.7: Microstructure of C1150 as given by ATI.

The grain diameter and the corresponding ASTM grain size obtained from Jeffries' procedure are given in Table 4.2. H920 showed a smaller grain size than the forged samples, which is as expected from the HIPing process. For the forged samples, the grain size increased with increasing heat treatment. Since limited photos of C1150 were available, the ASTM grain size of C1150 was taken from the datasheet supplied by ATI. The high ATSM grain size of C1150 is concurrent with the introduction of sub-grains during the cold working process [23].

Table 4.2: Grain diameter and the corresponding ASTM grain size for the different versions of Inconel 625. The grain size was calculated in accordance with ASTM E112 [62].

Material	Grain diameter [μm]	ASTM grain size
H920	14.5	9.0
F920	31.7	7.0
F1010	31.8	7.0
F1100	85.7	4.0
C1150	N/A	10.0

4.3.2 Precipitates

During the investigation in the optical microscope, several precipitates were found in the different versions of Inconel 625. For H920, the precipitates were found in large amounts scattered all over the matrix, as can be seen in Figure 4.8. Figure 4.9 and Figure 4.10 show the precipitates found in F920 and F1010, respectively. Both these materials showed a high amount of grain boundary precipitates, as well as some matrix precipitates. However, the size and amount of grain boundary precipitates appeared to be highest in F1010. In F1100, the amount of grain boundary precipitates was heavily reduced, as can be seen in Figure 4.11. Some large matrix precipitates were also found in F1100, where one of these are clearly visible and marked by a red circle in Figure 4.11. In general, the matrix precipitates found in F920, F1010 and F1100 were bigger than the grain boundary precipitates. In C1150, the precipitates were large and scattered throughout the matrix, as can be seen in Figure 4.12.

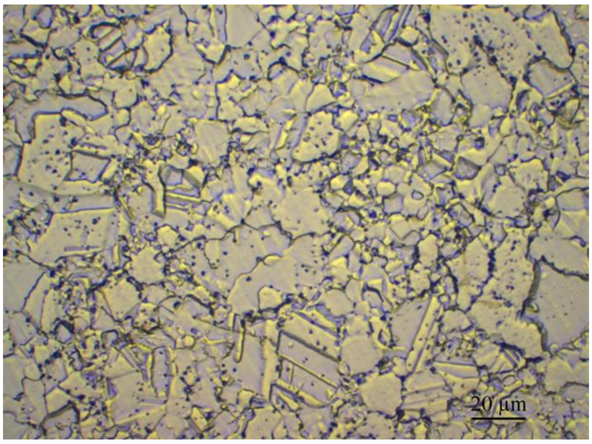

Figure 4.8: Precipitates in H920 at 50X magnification.

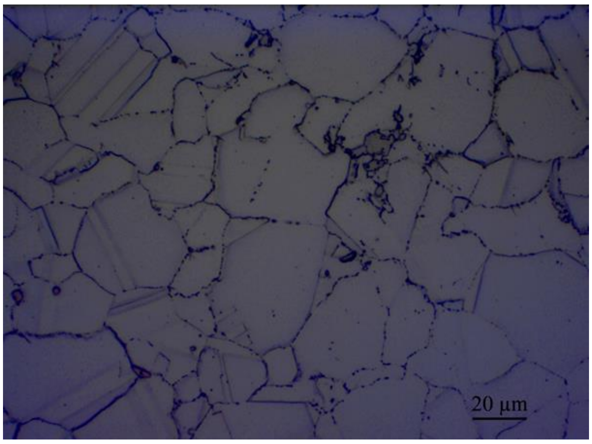

Figure 4.9: Precipitates in F920 at 50X magnification.

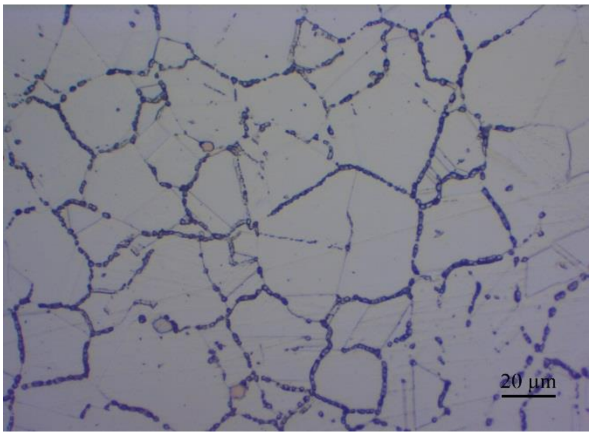

Figure 4.10: Precipitates in F1010 at 50X magnification. Grain boundary precipitates visible as a continuous layer.

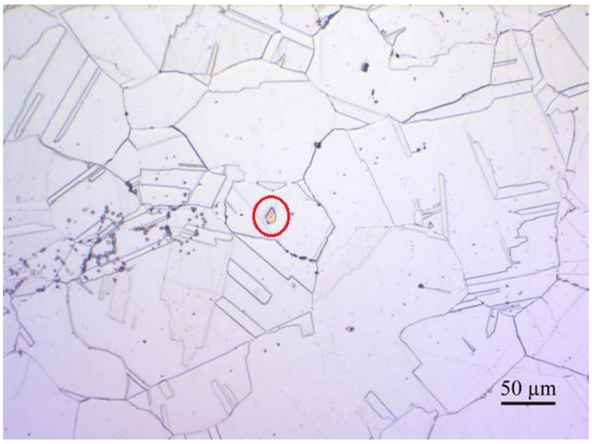

Figure 4.11: Precipitates in F1100 at 20X magnification. Large matrix precipitate marked with red circle.

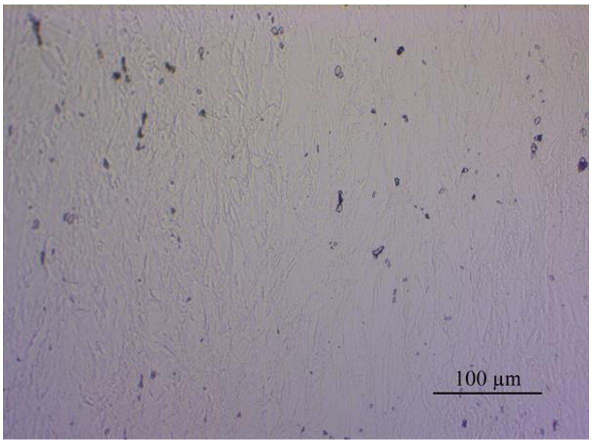

Figure 4.12: Precipitates in C1150 at 10X magnification.

4.4 EDS

The results from the chemical analysis done in the EDS are given in the following section. For each version of Inconel 625, the chemical content of the matrix was examined and found to be in good agreement with the actual composition as given by the manufacturers, see Table 3.1.

The chemical content of the matrix was used as a reference for evaluating the precipitates found in the other spots. The chemical content of the spots examined are given in Appendix C.

Figure 4.13 shows a SEM image indicating some of the spots examined by EDS for H920.

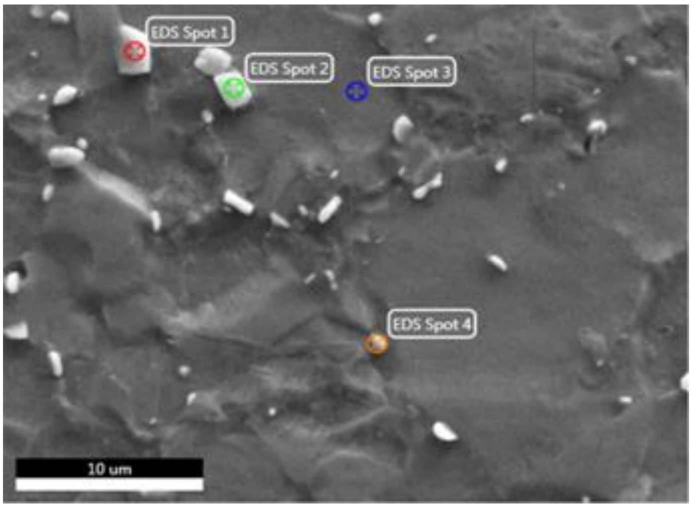

Figure 4.13: Spots marked for chemical examination by EDS for H920.

Spot one in Figure 4.13 showed elevated levels of carbon, nitrogen and niobium, indicating that the particle is a Nb(C,N)-carbonitride. The chemical content of spot one is representative for all the largest particles found in H920. Spot four showed high levels of carbon, chromium, nickel and some molybdenum. This seems to indicate that the particle is a $(Mo,Cr,Ni)_6C$-particle. However, the chemical content of spot four is similar to the chemical content of the matrix. It is therefore a degree of uncertainty related to this finding.

Figure 4.14 shows a SEM image indicating some of the spots examined by EDS for F920.

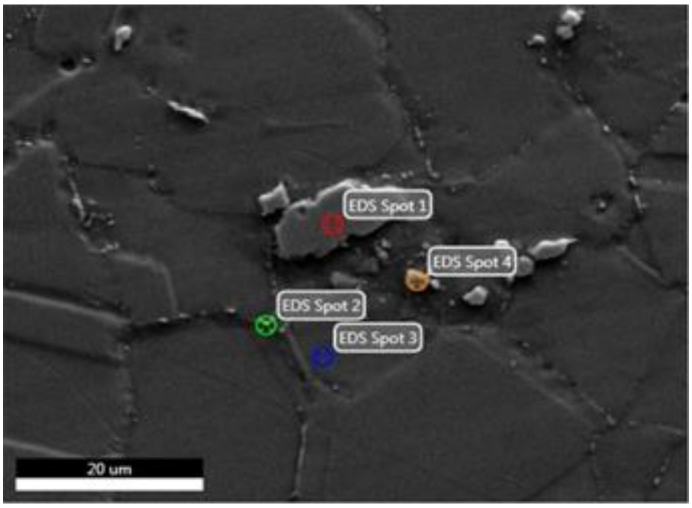

Figure 4.14: Spots marked for chemical examination by EDS for F920.

Spot one in Figure 4.14 showed elevated levels of carbon, niobium and titanium, indicating that the particle is a (Nb,Ti)C-particle. Spot two is located on a grain boundary and showed elevated levels of carbon, molybdenum, chromium and nickel, indicating that the particle is a $(Mo,Cr,Ni)_6C$-particle. In general, the large particles found scattered in the matrix were MC-particles, where M is Nb and Ti, while the smaller particles found at the grain boundaries were M_6C-particles, where M is Mo, Cr and Ni. By considering the atomic percentage values for F920 spot two found in Appendix C, the C to (Mo,Cr,Ni) ratio is found to be approximately 1 to 3. Although (Mo,Cr,Ni)C-particles are most commonly referred to as M_6C, these particles have been found to have a composition ranging from M_3C to $M_{13}C$ [17]. It is therefore safe to assume that the particles found at the grain boundaries indeed are M_6C-particles.

Figure 4.15 shows a SEM image indicating some of the spots examined by EDS for F1010.

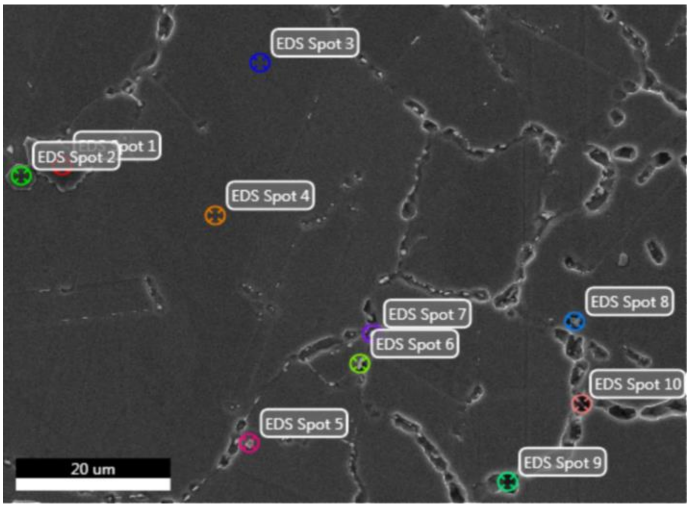

Figure 4.15: Spots marked for chemical examination by EDS for F1010.

Spot one in Figure 4.15 exhibited elevated levels of nitrogen and titanium, indicating that the large particle is a TiN-particle. Spot five is located on one of the grain boundary particles and showed elevated levels of carbon, molybdenum, chromium and nickel, indicating that the particle is a $(Mo,Cr,Ni)_6C$-particle. The general observation from the EDS-analysis was that the large precipitates found scattered in the matrix were TiN-particles, while the smaller grain boundary precipitates were M_6C-particles.

Figure 4.16 shows a SEM image indicating some of the spots examined by EDS for F1100.

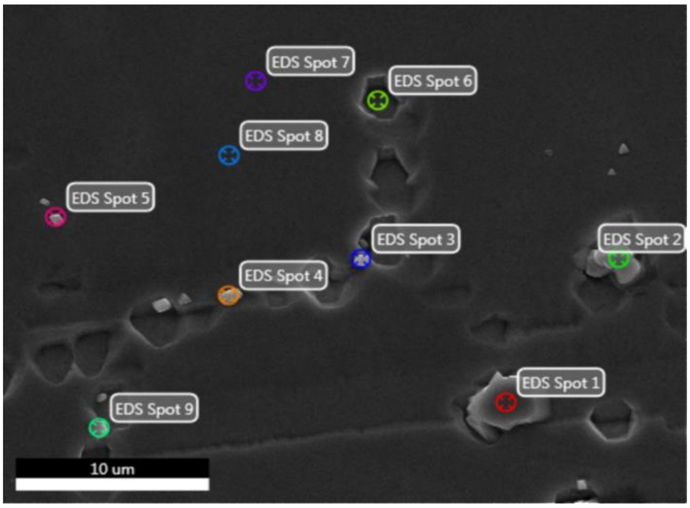

Figure 4.16: Spots marked for chemical examination by EDS for F1100.

Spot one in Figure 4.16 showed elevated levels of carbon and niobium, and somewhat elevated levels of titanium, indicating that the large particles are (Nb,Ti)C-particles. Spot four exhibited elevated levels of carbon, molybdenum, chromium and nickel, indicating that the particles are $(Mo,Cr,Ni)_6C$-particles. The general observation from the EDS analysis was that the large precipitates found scattered in the matrix were MC-particles, and that the smaller grain boundary precipitates were M_6C-particles. It should also be noted that one of the large particles found in F1100 showed very similar chemical composition as spot one in F1010, indicating that TiN-particles were also present in F1100.

Figure 4.17 shows a SEM image indicating some of the spots examined by EDS for C1150.

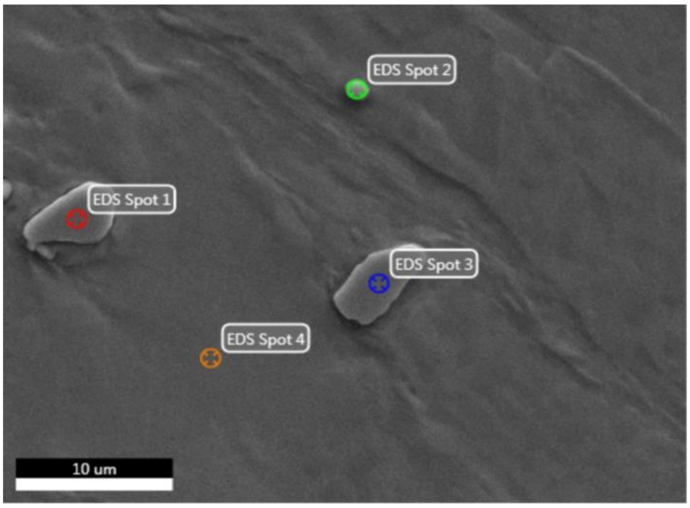

Figure 4.17: Spots marked for chemical examination by EDS for C1150.

Spot one in Figure 4.17 exhibited elevated levels of carbon, niobium and titanium, indicating that the carbides found in C1150 are (Nb,Ti)C-particles. These MC carbides were the only particles found in C1150.

The carbides found in the different versions of Inconel 625 are summarized in Table 4.3.

Table 4.3: Carbides found in the different versions of Inconel 625.

Material	**H920**	**F920**	**F1010**	**F1100**	**C1150**
Carbides	M(C,N)[1] + M_6C[2]	MC[3] + M_6C	TiN + M_6C	TiN +MC + M_6C	MC

1) (Nb,Ti)(C,N), 2) $(Mo,Cr,Ni)_6C$, 3) (Nb,Ti)C

4.5 Hardness test

Table 4.4 gives the Vickers hardness for the different versions of Inconel 625 obtained from the hardness test, with the corresponding Rockwell hardness C-scale conversion. By comparing the hardness of the different versions of Inconel 625 with the stress-strain curves given in Figure 4.2, it is evident that when the strength decreases, the hardness decreases as well. This is in agreement with the literature [12].

Table 4.4: Vickers hardness (HV) for the different versions of Inconel 625, with the corresponding Rockwell hardness. Conversion from HV to HRC was done in accordance with ASTM E140 – 12b [63].

Material	**Vickers Hardness [HV]**	**Rockwell Hardness C-scale [HRC]**
H920	268.8	25.5
F920	248.1	22.5
F1010	220.7	17.0
F1100	179.1	6.5
C1150	509.8	50.0

4.6 HISC-test

4.6.1 Fracture values from the HISC test

The calibrated fracture values from the HISC test for the different versions of Inconel 625 are given in Tables 4.5-4.7. “No fracture” refers to the last stress at which the samples did not break and “Fracture” equals the stress to which the samples were loaded when they broke. The values are given as a percentage of the lowest yield strength obtained in the tensile test for each version of Inconel 625, as found in Table 4.1. Note that F1010 sample number four broke during the initial loading to 100% because of wrongful use of the equipment. This fracture value is therefore unknown and not used in the rest of the thesis. F1100 samples number one and five did not fracture because they were so ductile that they reached the maximum possible tightening in the Cortest rings. C1150 sample number five was reported by Erlend Haugsnes to have been damaged before the testing and is therefore not included. The fracture values according to the excel sheet supplied by the supervisor are given in Appendix D.

Table 4.5: Calibrated fracture values as percentage of the yield strength (YS) from the HISC testing of H920 and F920.

Sample	**H920**		**F920**	
	No fracture [%]	**Fracture [%]**	**No fracture [%]**	**Fracture [%]**
1 (reference)	183.0	185.2	173.4	177.3
2	169.4	173.2	158.9	162.1
3	168.7	173.8	157.0	162.8
4	167.0	171.5	155.1	159.8
5	170.3	174.5	161.0	164.0

Table 4.6: Calibrated fracture values as percentage of the yield strength (YS) from the HISC testing of F1010 and F1100.

Sample	**F1010**		**F1100**	
	No fracture [%]	**Fracture [%]**	**No fracture [%]**	**Fracture [%]**
1 (reference)	199.8	208.3	213.5	N/A
2	175.8	180.7	198.3	203.8
3	182.2	188.3	187.2	196.4
4	N/A	N/A	198.5	204.2
5	184.3	190.7	211.6	N/A

Table 4.7: Calibrated fracture values as percentage of the yield strength (YS) from the HISC testing of C1150.

Sample	**C1150**	
	No fracture [%]	**Fracture [%]**
1 (reference)	106.1	107.1
2	110.3	112.7
3	110.4	114.2
4	105.7	109.2

Table 4.8 summarizes the effect on fracture strength by charging the samples with hydrogen. The table includes the average fracture strength for samples charged with hydrogen, as well as the average reduction in fracture strength for samples charged with hydrogen compared to the reference samples. These values are given as a percentage of the lowest yield strength obtained in the tensile test for each version of Inconel 625, as can be found in Table 4.1. Additionally, the average reduction of fracture strength is given as a percentage of the lowest UTS obtained in the tensile test for each version of Inconel 625, as displayed in Table 4.1. The reduction of fracture strength relative to the UTS is the value used in the subsequent chapters. The standard deviation (STD) is shown in parenthesis.

Since F1100 sample number one and five did not fracture, it is not possible to get an exact value for the average fracture strength and the average reduction in fracture strength for F1100. However, an estimate has been done by using the “No fracture” values as the fracture values for sample one and five. By doing this, the average fracture strength and average reduction of fracture strength for F1100 will be lower than they should be. Note that C1150 has a negative average reduction in fracture strength, meaning that the reference sample fractured at a lower stress than the hydrogen exposed samples.

Table 4.8: Key findings from the HISC test. Average fracture strength and average reduction in fracture strength given as a percentage of the lowest yield strength (YS) obtained in the tensile test. Average reduction of fracture strength is also given as a percentage of the ultimate tensile strength (UTS). The standard deviation is given in parenthesis.

Material	Average fracture strength [% of YS]	Average reduction in fracture strength [% of YS]	Average reduction of fracture strength [% of UTS]
H920	173.0 (±1.2)	12.2 (±1.2)	6.6 (±0.7)
F920	162.9 (±0.7)	14.4 (±0.7)	8.1 (±0.4)
F1010	186.5 (±3.9)	21.7 (±3.9)	10.4 (±1.8)
F1100	204.0 (±4.4)	9.5 (±5.3)	4.4 (±2.5)
C1150	112.0 (±2.1)	-4.9 (±2.1)	-4.6 (±2.0)

4.6.2 Reduction of area from HISC test

Table 4.9 gives the RA-values obtained from the HISC test for the reference samples and the average RA-values from the tensile test, as well as the average RA-value with the corresponding STD for the samples charged with hydrogen. The reduction of reduction of area for the samples charged with hydrogen in reference to the reference samples is also given.

Table 4.9: Reduction of area (RA) for the reference samples and the samples pre-charged with hydrogen from the HISC test. Reduction of reduction of area (RRA) for the pre-charged samples. RA from the tensile test taken from Table 4.1.

Material	RA for reference sample [%]	Average RA from tensile test [%]	Average RA for samples charged with hydrogen including STD [%]	RRA [%]
H920	51.8	51.1	22.8 (±3.8)	56.0 (±7.4)
F920	55.0	54.0	26.0 (±9.7)	52.7 (±17.7)
F1010	63.2	58.9	33.5 (±6.1)	46.9 (±9.7)
F1100	N/A	60.9	43.3 (±0.2)	28.8 (±0.4)
C1150	42.3	49.6	15.9 (±7.2)	62.5 (±16.9)

Since the F1100 reference sample did not break, the RA-value was estimated by using the average RA-value from the tensile test, as taken from Table 4.1. These values are based on samples not charged with hydrogen, and should be identical with the reference samples used in the HISC testing. By comparing the average RA-values from the tensile test with the RA-values for the reference samples for the other materials, it is evident that these values are similar, indicating that the estimate should be reasonable. Sample number five from F1100 is not included in the RA and RRA calculations, since it did not fracture. However, this sample showed a high degree of ductility and it is therefore reasonable to assume that it also had a higher RA-value than the other samples charged with hydrogen. If this is the case, the average RA-value for the samples charged with hydrogen should be higher, resulting in a lower RRA-value.

4.7 SEM of fracture surface

4.7.1 Reference sample overview

Figures 4.18-4.21 show SEM overview pictures of the fracture surface for the H920, F920, F1010 and C1150 reference samples. All the samples showed a high degree of necking, which is characteristic for ductile fractures. Since the F1100 reference sample did not fracture, it was not possible to examine any fracture surface. However, it is reasonable to assume that the F1100 reference sample would have shown a similar fracture surface, as it exhibited a high degree of ductility during loading.

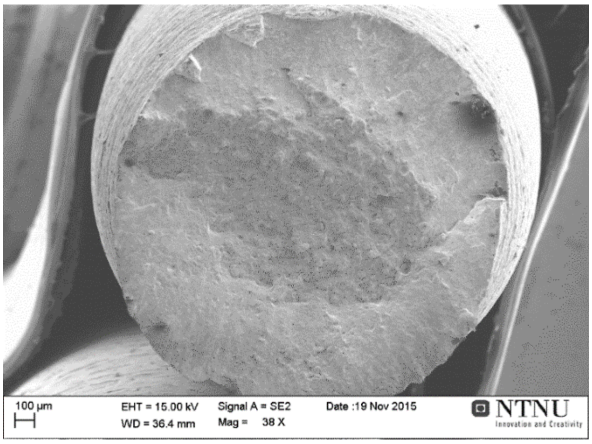

Figure 4.18:Overview picture of H920 reference sample.

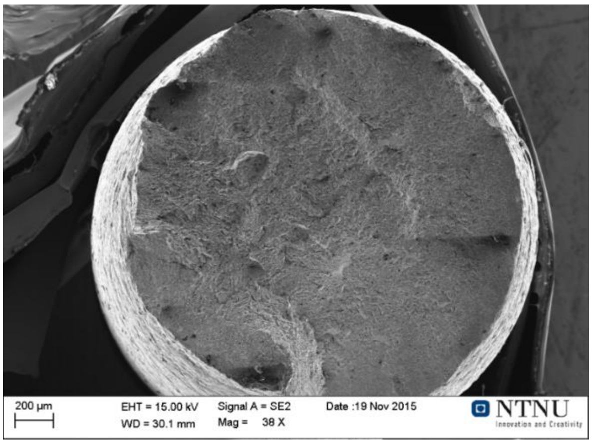

Figure 4.19: Overview picture of F920 reference sample.

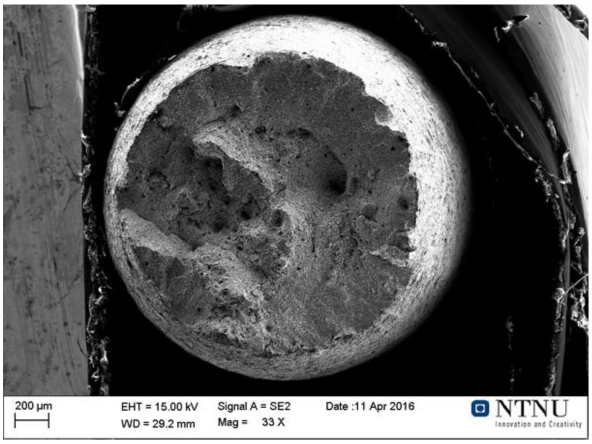

Figure 4.20: Overview picture of F1010 reference sample.

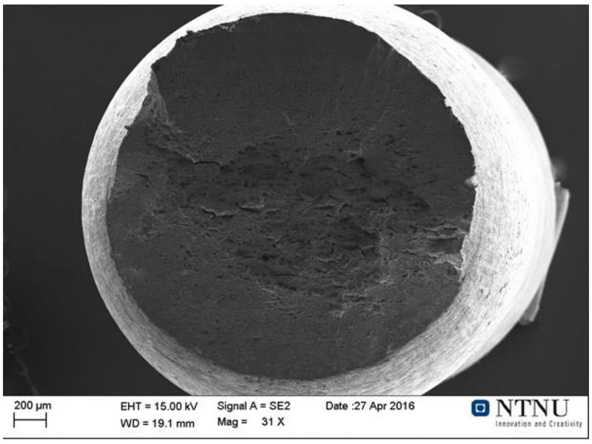

Figure 4.21: Overview picture of C1150 reference sample.

4.7.2 Reference sample center

A closer examination of the fracture surfaces is given in Figures 4.22-4.25, which shows the center of the reference samples at 2000X magnification. All the pictures showed surfaces with a high concentration of dimples, which is characteristic for ductile fractures. No brittle features were observed.

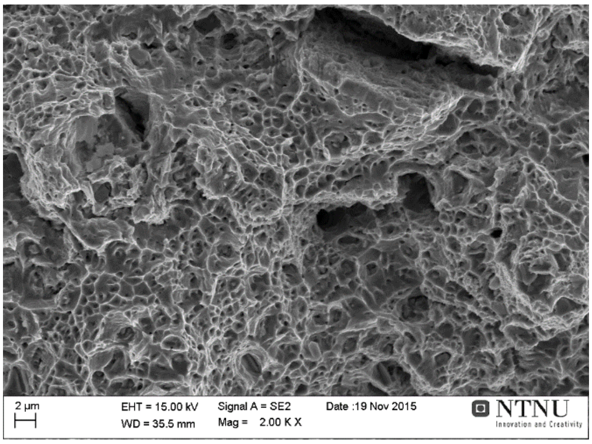

Figure 4.22: Center of H920 reference sample.

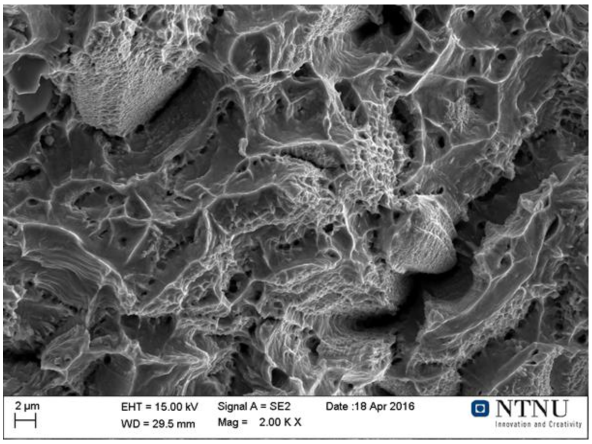

Figure 4.23: Center of F920 reference sample.

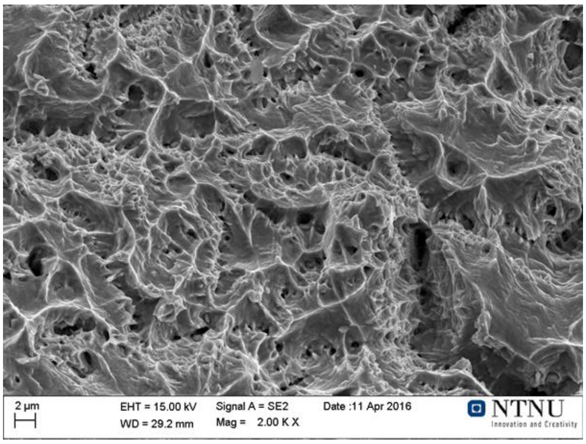

Figure 4.24: Center of F1010 reference sample.

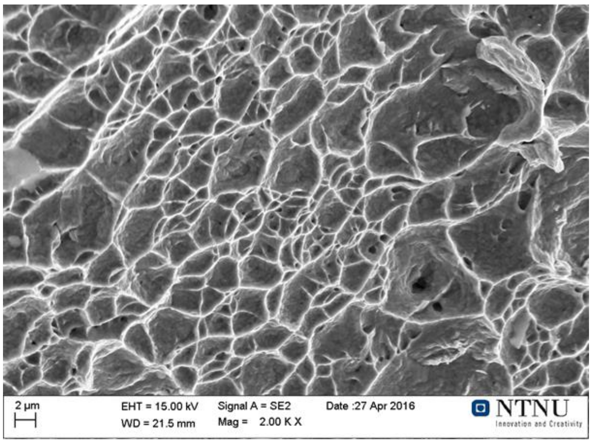

Figure 4.25: Center of C1150 reference sample.

4.7.3 Reference sample edge

In Figures 4.26-4.29, the edges of the same reference samples are given at 2000X magnification. As for the center of these samples, the edges showed a high concentration of dimples, which is characteristic for ductile fractures. No brittle features were observed.

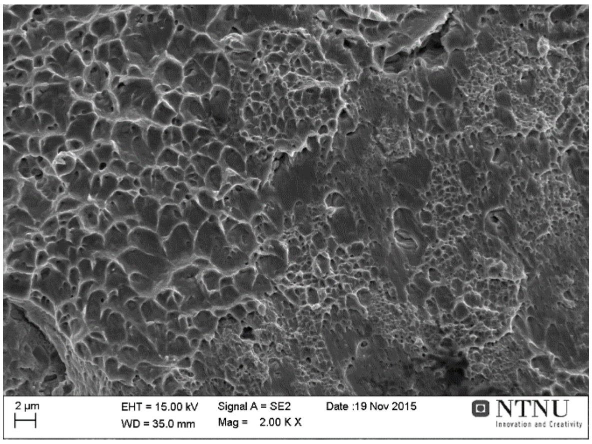

Figure 4.26: Edge of H920 reference sample.

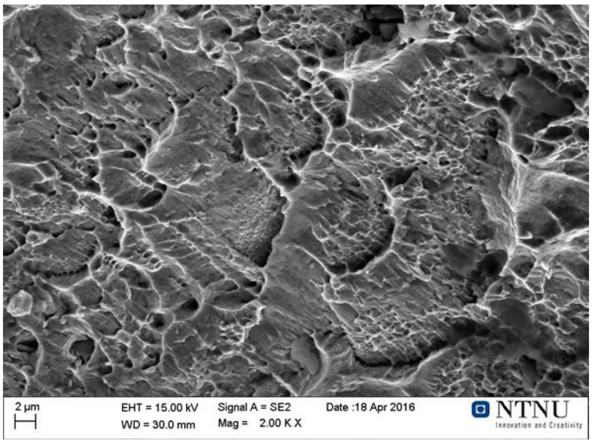

Figure 4.27: Edge of F920 reference sample.

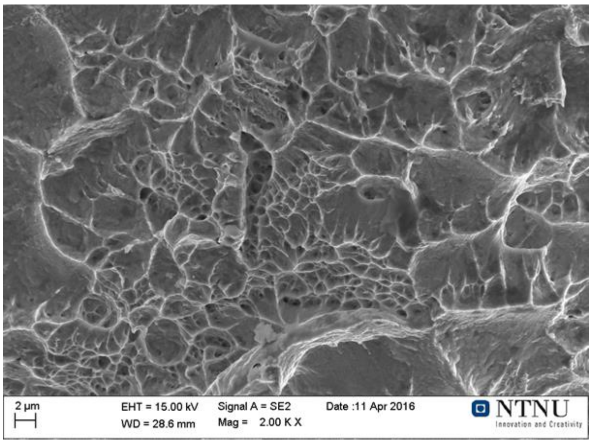

Figure 4.28: Edge of F1010 reference sample.

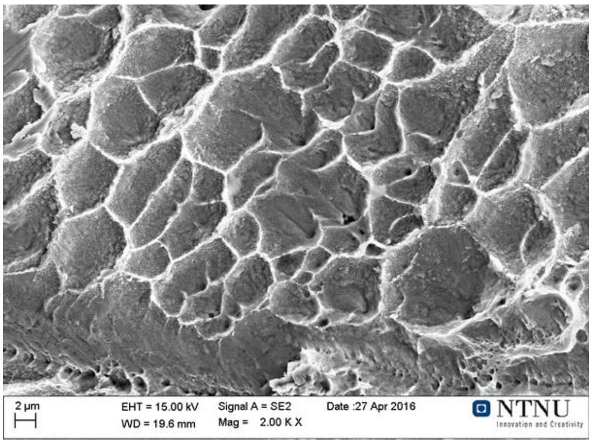

Figure 4.29: Edge of C1150 reference sample.

4.7.4 Hydrogen charged samples overview

In Figures 4.30-4.34, overview pictures of the fracture surfaces for the different versions of Inconel 625 charged with hydrogen are shown. The samples showed less necking than the reference samples, indicating that hydrogen has had an embrittling effect. This observation is quantified by the RA- and RRA-values in Table 4.9.

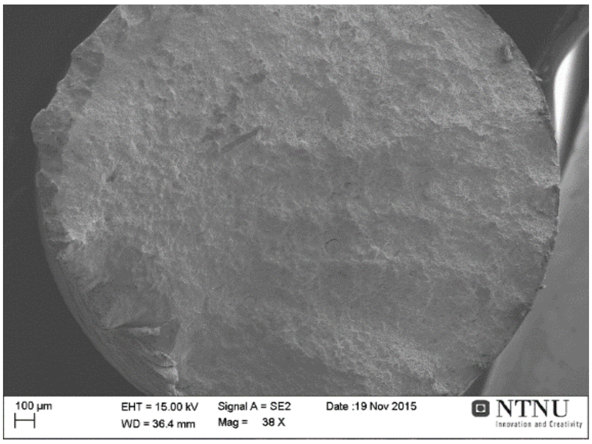

Figure 4.30: Overview picture of H920 sample charged with hydrogen.

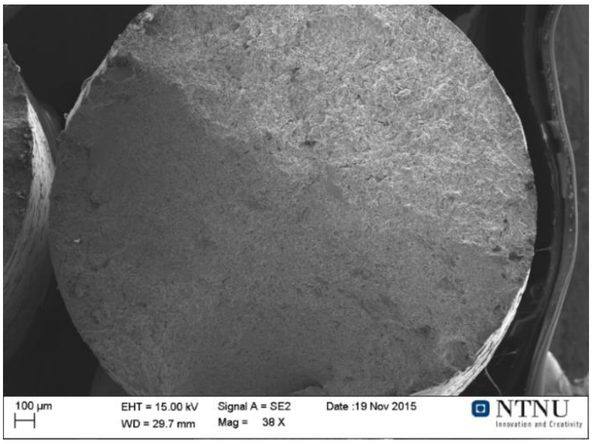

Figure 4.31: Overview picture of F920 sample charged with hydrogen.

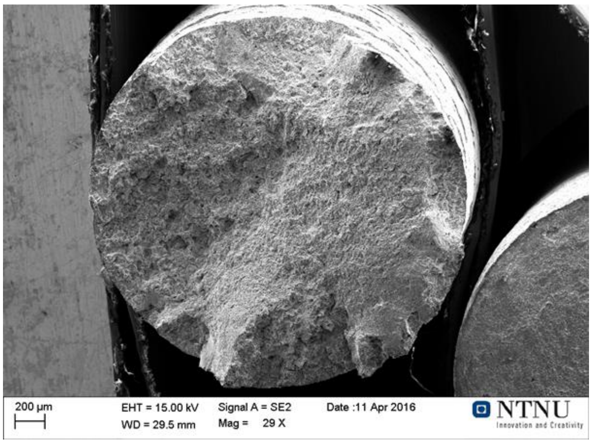

Figure 4.32: Overview picture of F1010 sample charged with hydrogen.

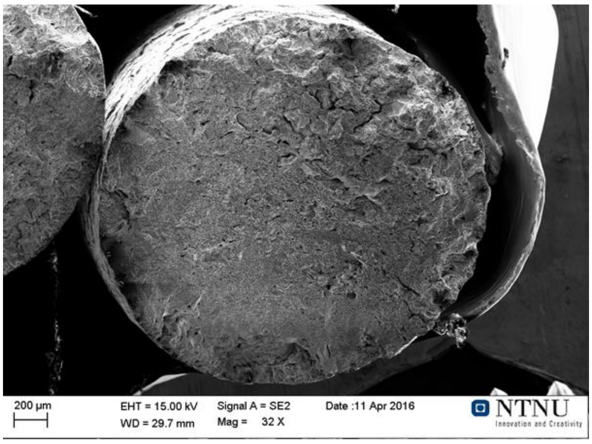

Figure 4.33: Overview picture of F1100 sample charged with hydrogen.

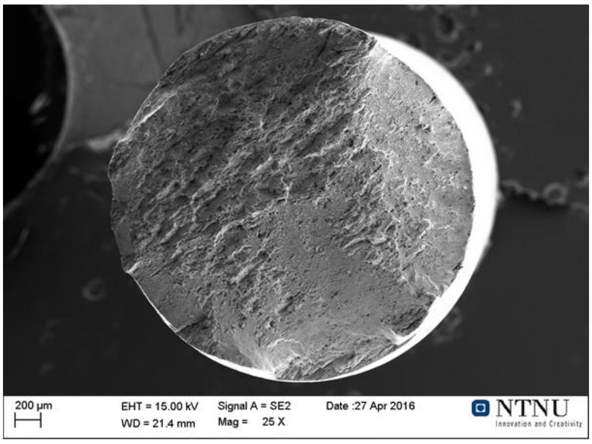

Figure 4.34: Overview picture of C1150 sample charged with hydrogen.

4.7.5 Hydrogen charged samples center

Figures 4.35-4.39 give a closer look at the center of the same samples at 2000X magnification. The surfaces revealed a high concentration of dimples, indicating that the center of the samples were still ductile after being charged with hydrogen. This is most likely the result of a low hydrogen concentration in the center, because of the low diffusivity of hydrogen in Inconel 625 [64].

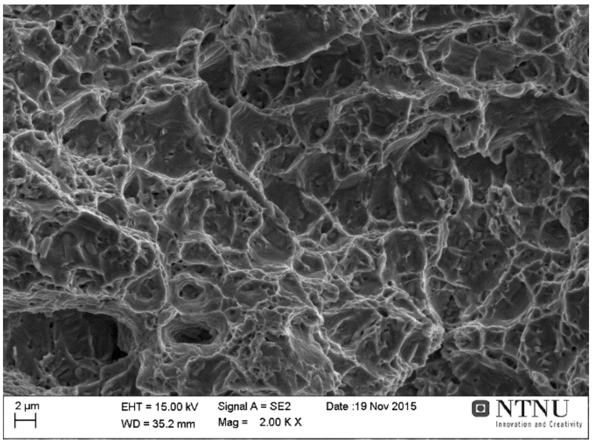

Figure 4.35: Center of H920 sample charged with hydrogen.

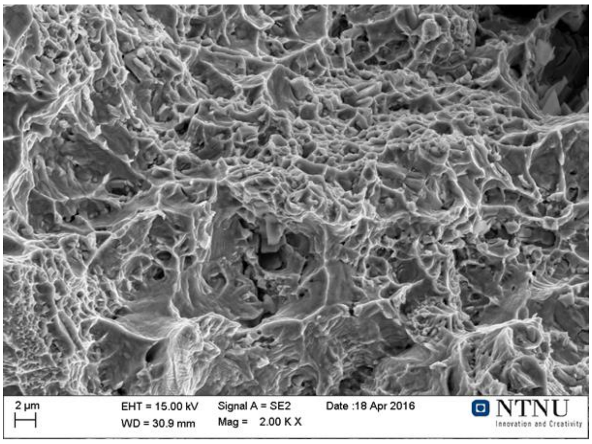

Figure 4.36: Center of F920 sample charged with hydrogen.

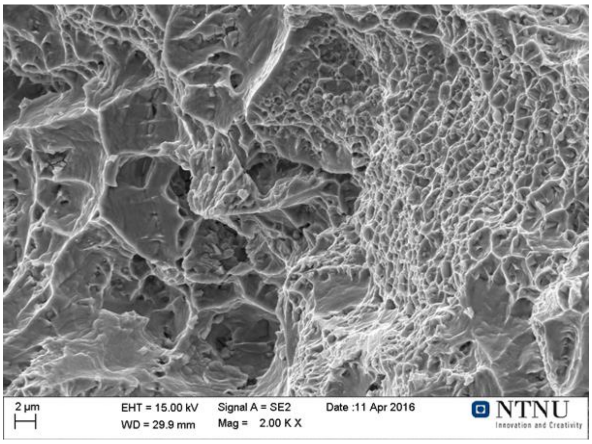

Figure 4.37: Center of F1010 sample charged with hydrogen.

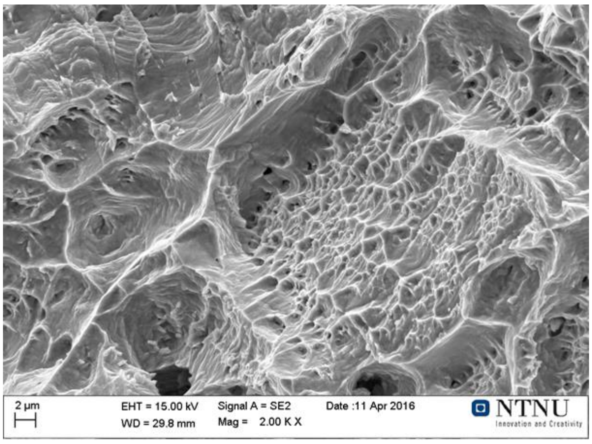

Figure 4.38: Center of F1100 sample charged with hydrogen.

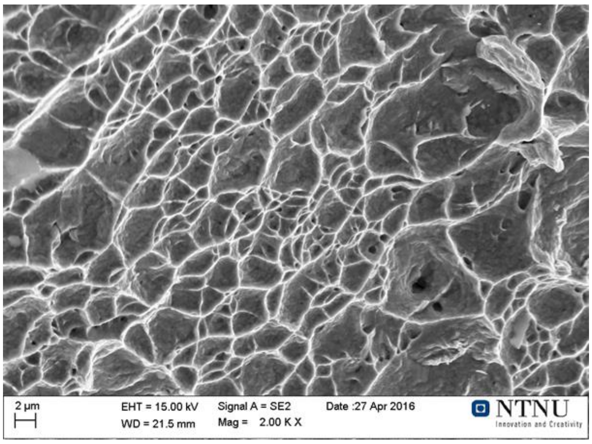

Figure 4.39: Center of C1150 sample charged with hydrogen.

4.7.6 Hydrogen charged samples edge

In Figures 4.40-4.44, the edges of the samples are given at 2000X magnification. Here, the samples exhibited a mix of brittle transgranular and intergranular features. This was attributed to the hydrogen concentration being highest near the edge and shows that hydrogen has had an embrittling effect. Compared to the other samples, the edge of C1150 shows less brittle features, and some dimples are clearly visible. Additionally, areas along the edge showing completely ductile fracture were also found during the examination of C1150, as can be seen in Figure 4.45. This seems to indicate that hydrogen has affected C1150 less than the other samples.

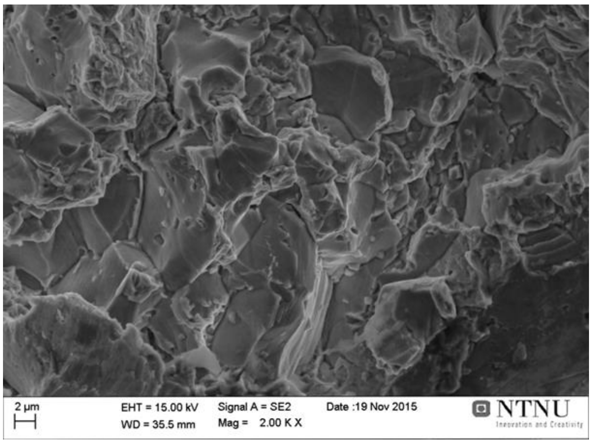

Figure 4.40: Edge of H920 sample charged with hydrogen.

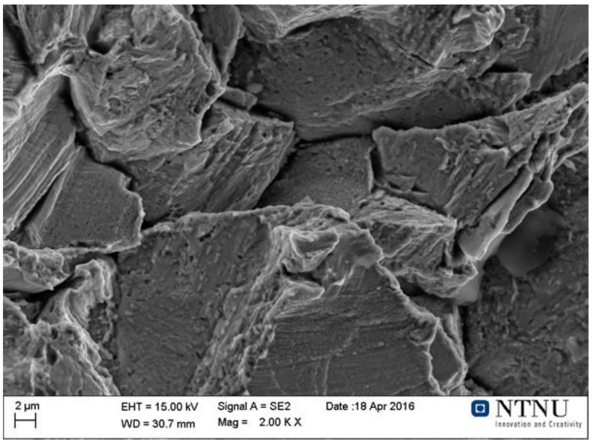

Figure 4.41: Edge of F920 sample charged with hydrogen.

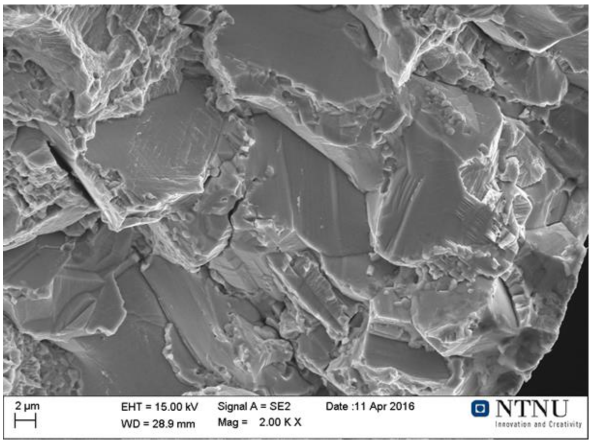

Figure 4.42: Edge of F1010 sample charged with hydrogen.

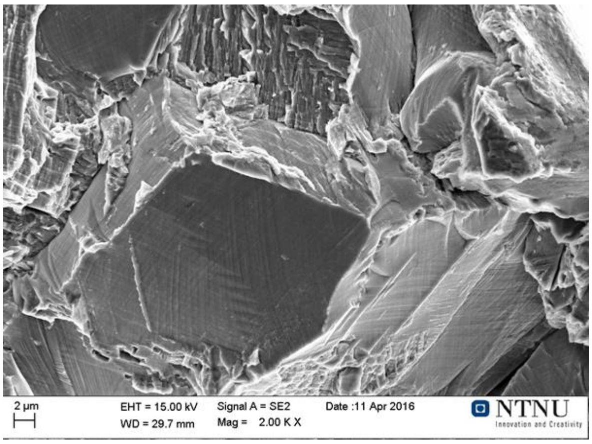

Figure 4.43: Edge of F1100 sample charged with hydrogen.

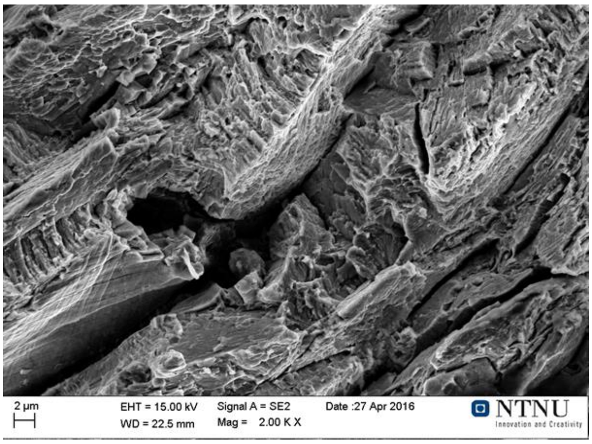

Figure 4.44: Edge of C1150 sample charged with hydrogen.

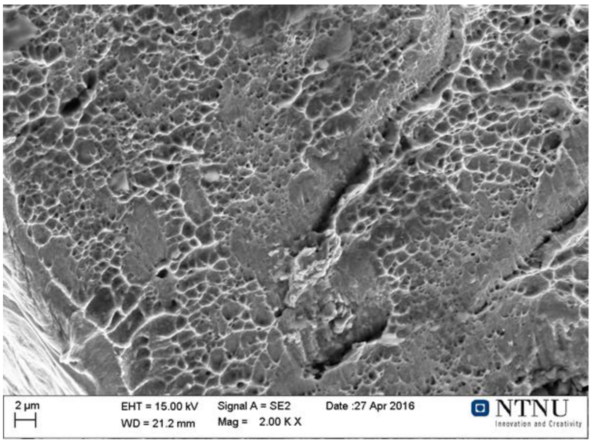

Figure 4.45: Edge of C1150 sample charged with hydrogen showing ductile fracture.

The fractographic examinations in the previous sections show a clear trend on the embrittling effect of hydrogen in Inconel 625. Samples containing no hydrogen, i.e. the reference samples, showed only ductile, dimpled features. This was also the case for the center of the samples charged with hydrogen, as the hydrogen concentration is assumed low at this point. The edges of the samples charged with hydrogen showed a mix of brittle transgranular and intergranular features, as the hydrogen concentration was highest near the surface. The only exception was C1150, which showed signs of ductility even at the edge.

4.7.7 Secondary cracking

Pictures were also taken from the side of the samples to examine the presence of secondary cracks. Figures 4.46-4.50 show the outer surface of some of the samples for the different versions of Inconel 625. No secondary cracks were observed on a macroscopic scale for any of the reference samples. Almost all of the samples charged with hydrogen showed a high concentration of secondary cracks, indicating that the surfaces had become embrittled by the presence of hydrogen. The only exceptions were the C1150 samples, which did not show any secondary cracking. The samples to the left in Figure 4.50 is F1100 sample number 5, which did not fracture. This sample shows that secondary cracks can be present even prior to fracture when a sample is charged with hydrogen.

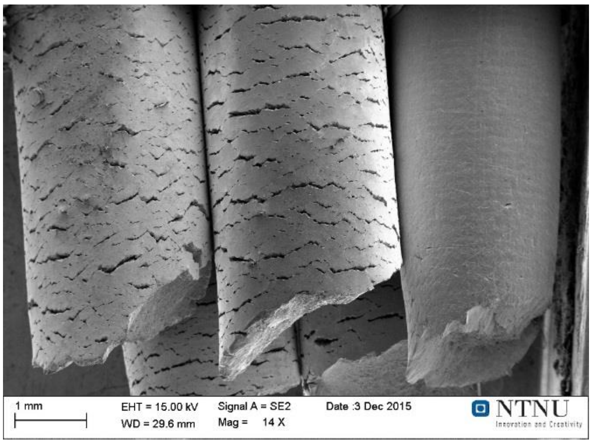

Figure 4.46: Picture from the side of three H920 samples. The sample to the right is the reference sample and the two other samples are charged with hydrogen. The samples charged with hydrogen show secondary cracks.

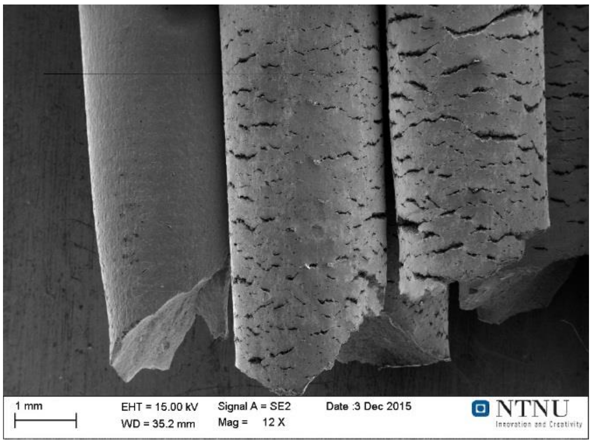

Figure 4.47: Picture from the side of three F920 samples. The sample to the left is the reference sample and the two other samples are charged with hydrogen. The samples charged with hydrogen show secondary cracks.

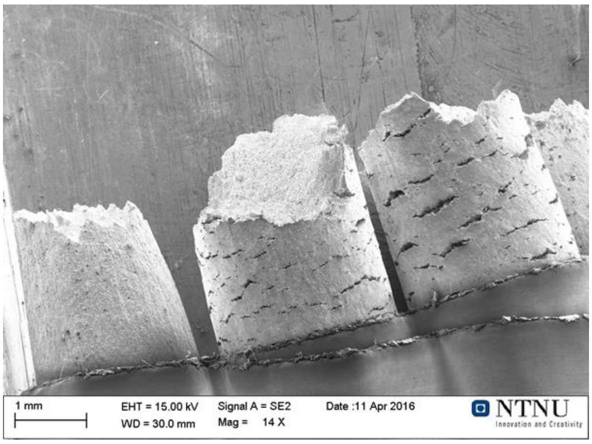

Figure 4.48: Picture from the side of three F1010 samples. The sample to the left is the reference sample and the two other samples are charged with hydrogen. The samples charged with hydrogen show secondary cracks.

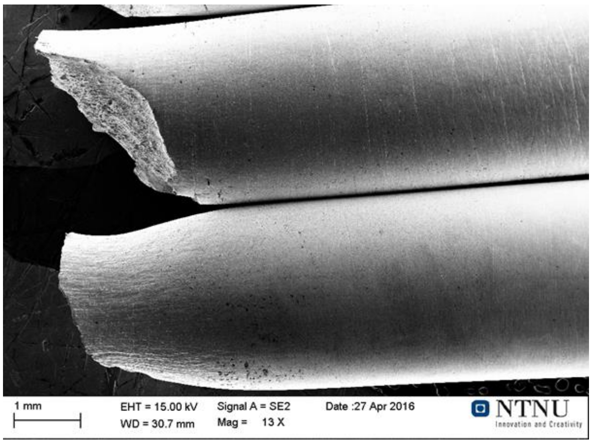

Figure 4.49: Picture from the side of two C1150 samples. The bottom sample is the reference sample and the other sample is charged with hydrogen. No secondary cracks are visible on either sample.

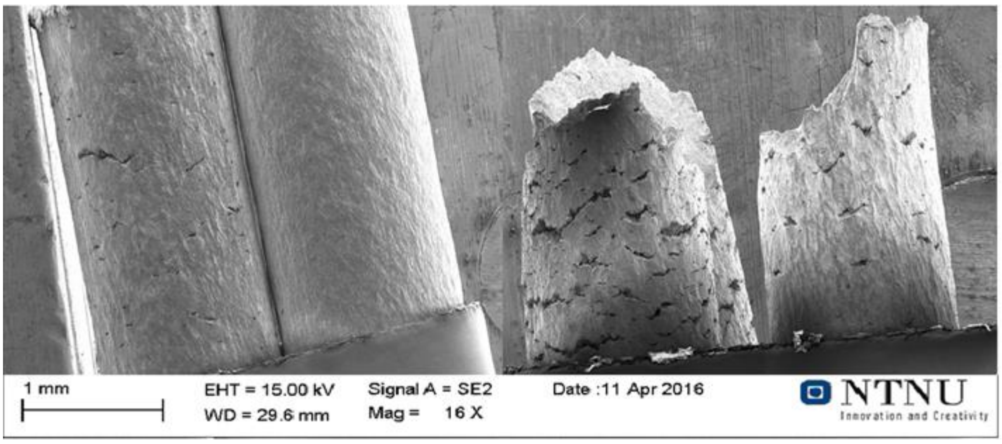

Figure 4.50: Picture from the side of four F1100 samples. The second sample from the left is the reference sample and the other samples are charged with hydrogen. The samples charged with hydrogen show secondary cracks. The sample to the left is sample number five, which did not fracture. It shows that secondary cracks are visible even prior to fracture.

4.7.8 Approximate length of brittle layer

During the examination of the fracture surfaces for the hydrogen exposed samples, an attempt was made to approximate the length of the brittle layer found at the samples' edge. This was done by examining each picture showing brittle characteristics near the edge and manually measuring the length of the brittle layer. Figure 4.51 illustrates how this was done. Along the length of the red line, the sample shows only brittle features. Beyond the red line, ductile, dimpled features are clearly visible. Several measurements were done for each sample, and the mean value was calculated. The findings are summarized in Table 4.10. Since C1150 showed large, ductile areas along the edge and generally few brittle areas, an approximation was not attempted for these samples.

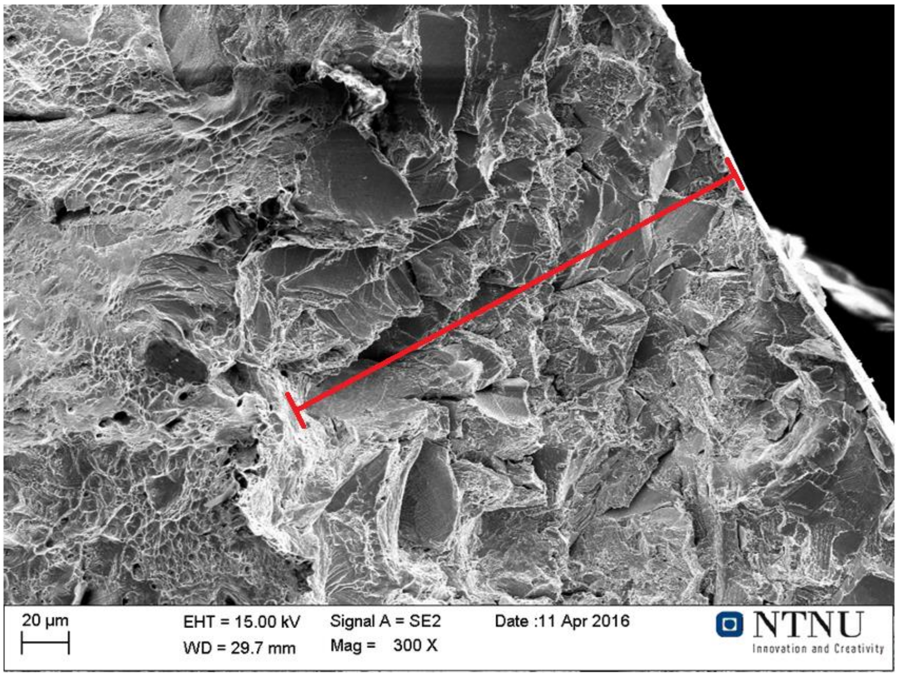

Figure 4.51: Illustration of method used to approximate the length of the brittle layer. The red line shows the extent of the brittle layer, beyond which ductile, dimpled features are clearly visible.

Table 4.10: Approximation of the length of the brittle layer in the hydrogen exposed samples. Standard deviation given in parenthesis.

Material	Length of brittle layer [µm]
H920	90 (±7)
F920	124 (±8)
F1010	98 (±3)
F1100	113 (±34)
Average	106 (±22)

4.8 Modified ASTM G48 test

Figures 4.52-4.55 show the graphs from the modified ASTM G48 test, where the potential is plotted vs time and temperature. To differentiate between the two parallels in each experiment, they are denoted 1 and 2. In Figures 4.52-4-54, the parallels are almost indiscernible, as the graphs lie on top of each other. During the third night of the experiment for H920 and F920, the heating regulator fell out and landed on the hot plate, causing the temperature of the electrolyte to go from 50°C to 60°C. As no potential drop was observed at this temperature, it was decided to continue with the experiment. Since the results from the first experiment showed a high pitting temperature (>85°C), the initial temperature for F1010 and F1100 was increased to 60°C. H920 and F920 showed stable graphs, with no signs of a potential drop, indicating that the critical pitting temperature is above 85°C. F1010 showed a steady decline after some time at 85°C, indicating that the CPT is close to 85°C. For F1100, one of the samples dropped below 500mV$_{Ag/AgCl}$, while the other sample showed a steady decline after some time at 85°C. This indicates that the CPT is approximately 85°C for F1100.

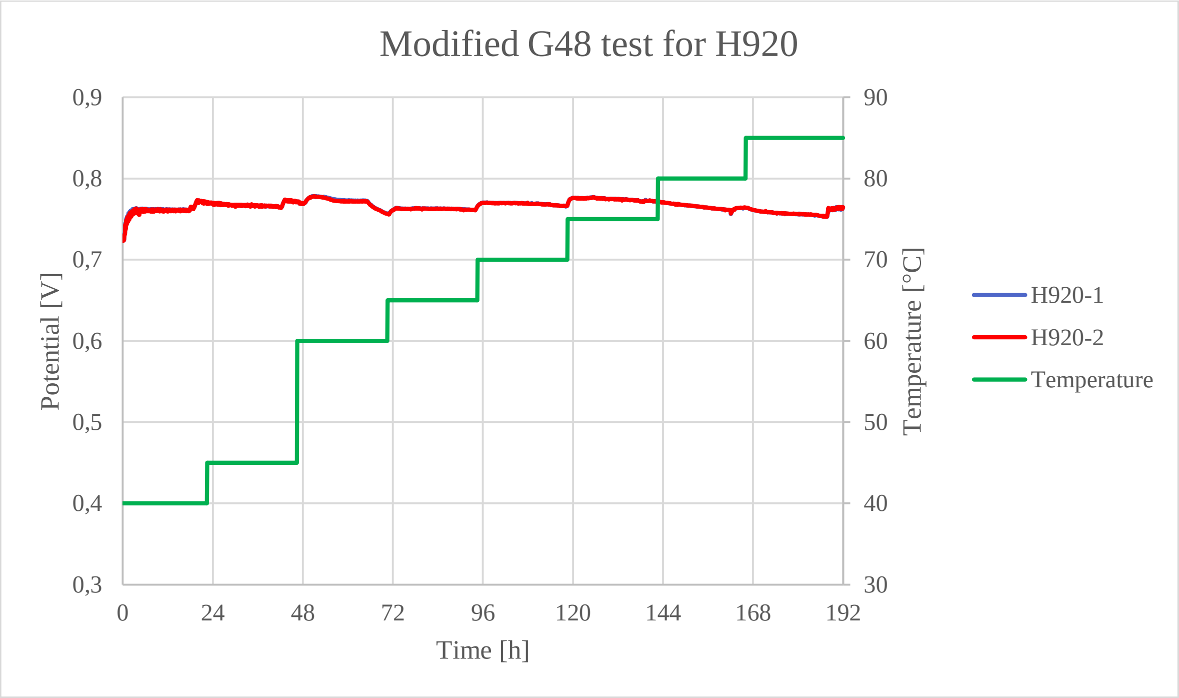

Figure 4.52: Modified ASTM G48 test for H920 where the potential is plotted vs time and temperature.

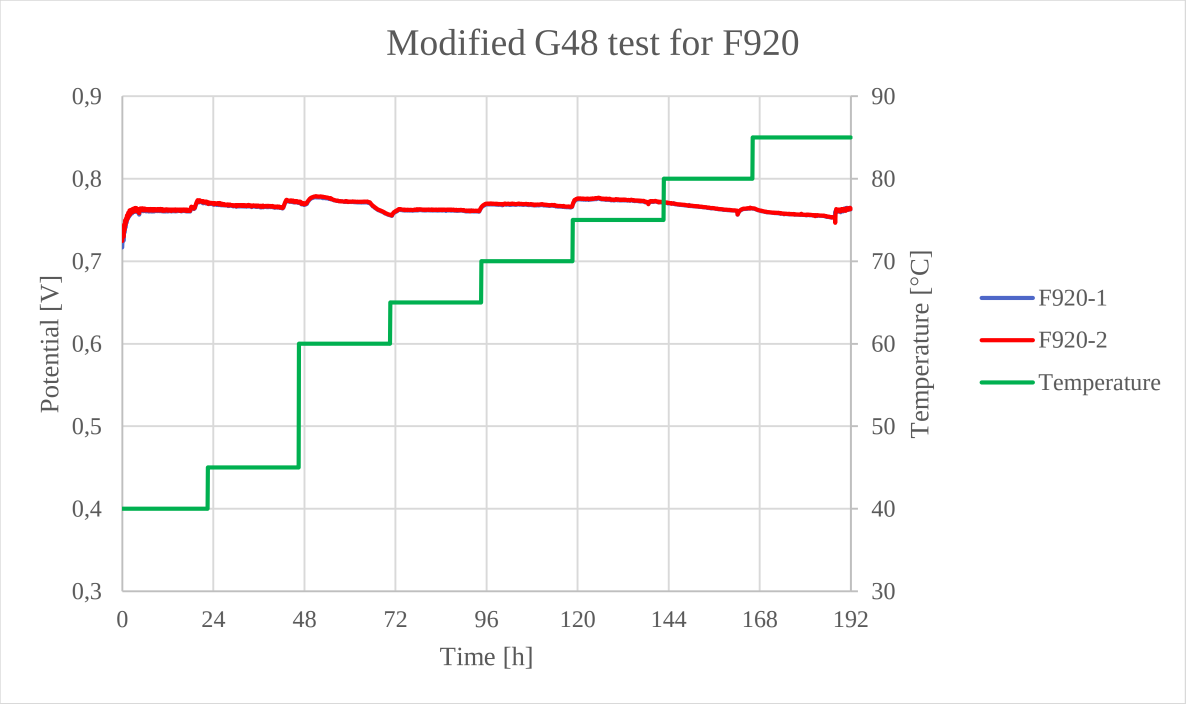

Figure 4.53: Potential vs time/temperature for the modified ASTM G48 test for F920.

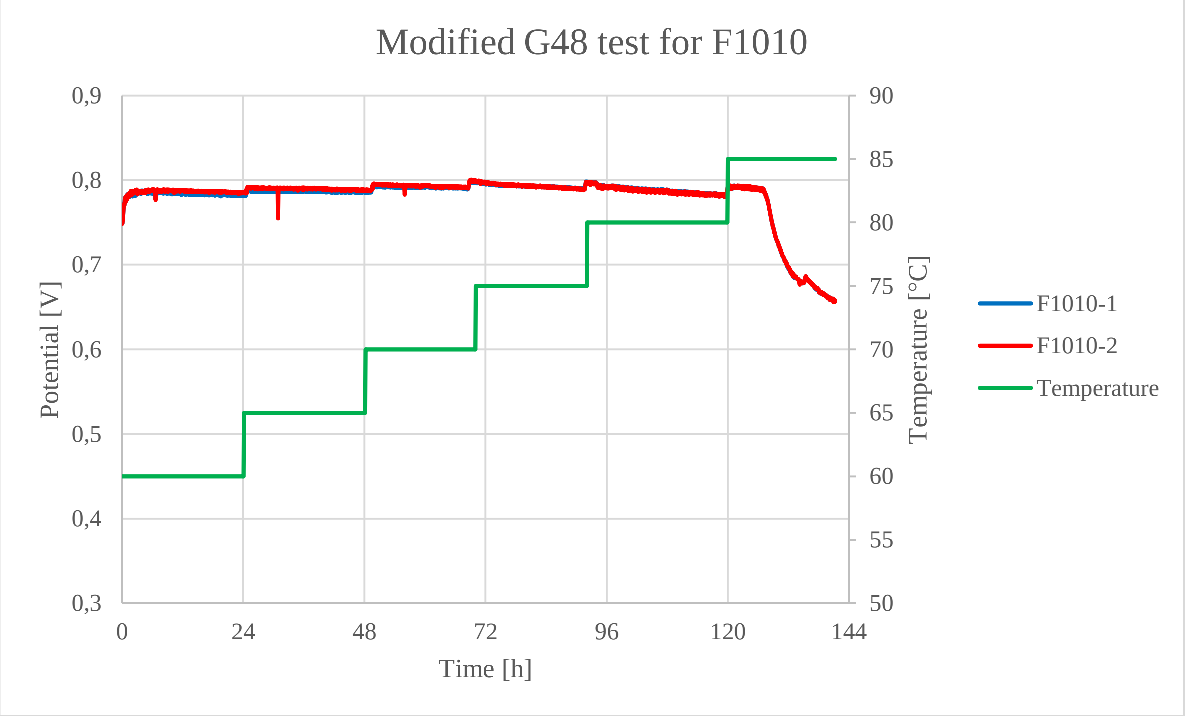

Figure 4.54: Potential vs time/temperature for the modified ASTM G48 test for F1010.

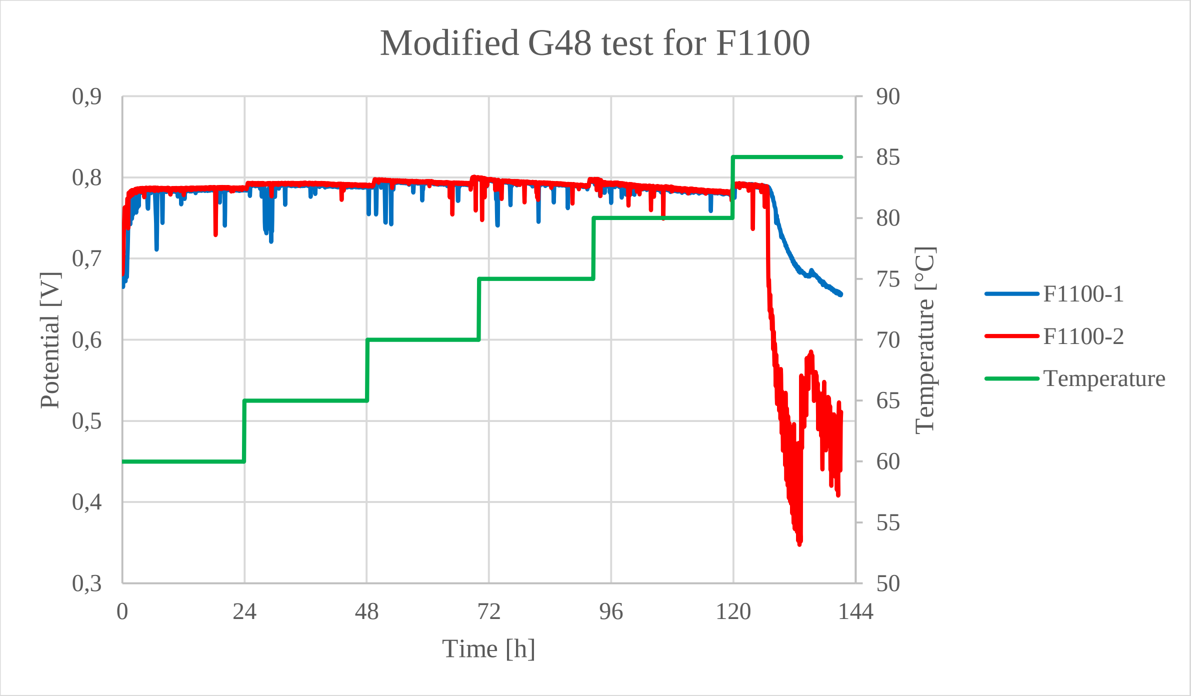

Figure 4.55: Potential vs time/temperature for the modified ASTM G48 test for F1100.

The critical pitting temperatures for the different versions of Inconel 625 are summarized in Table 4.11.

Table 4.11: Critical pitting temperature (CPT) for the different versions of Inconel 625.

Material	**H920**	**F920**	**F1010**	**F1100**
CPT	>85°C	>85°C	>85°C	~85°C

Table 4.12 gives the weight change for the samples exposed to the modified ASTM G48 test. Only F1100-2 showed a significant weight loss, which corresponds well to the fact that this was the only sample to drop below 500 mV$_{Ag/AgCl}$. Figure 4.56 shows F1100-2, where a corrosion attack is clearly visible around the area where the hole was previously located. The other samples showed no or minimal weight change. F1010-2 and F1100-1 showed a slight increase in weight, which might result from either a small error during weighing, or from the deposition of the red/brown $FeCl_3$ from the electrolyte on the samples. This deposit was impossible to remove during cleaning without damaging the base material. Figure 4.57 shows F1010-2 after testing, where the red/brown deposit is visible on the surface. The picture of F1010-2 is representative for all the samples where the potential did not drop below 500mV$_{Ag/AgCl}$.

Table 4.12: Weight change for the samples exposed to the modified ASTM G48 pitting test.

Sample	Weight before [g]	Weight after [g]	Weight change [g]
H920-1	17.5330	17.5330	0.0000
H920-2	17.4987	17.4987	0.0000
F920-1	17.1648	17.1648	0.0000
F920-2	17.2484	17.2482	-0.0002
F1010-1	16.5439	16.5439	0.0000
F1010-2	17.3709	17.3728	+0.0019
F1100-1	17.1975	17.1988	+0.0013
F1100-2	17.2412	16.5659	-0.6753

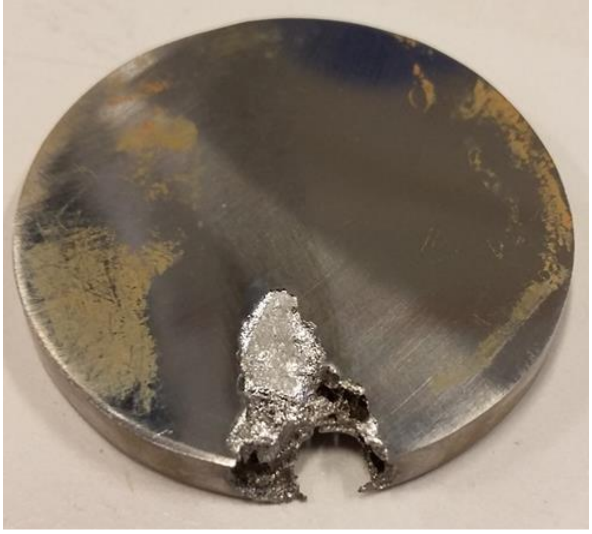

Figure 4.56: Sample F1100-2 showing corroded area.

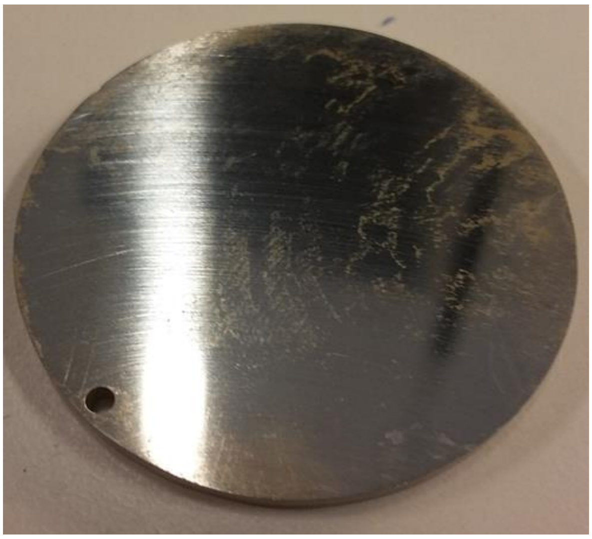

Figure 4.57: Sample F1010-2 after the modified ASTM G48 test showing a red/brown deposit on the surface.

A closer examination of the samples' surface is given in Figures 4.58-4.61. The samples that showed no decrease in potential, i.e. H920 and F920, displayed only small areas of attack, indicating that pitting was not fully initiated. On the F1010 samples, where some degree of potential-drop was observed, the pits were found to have grown in size. For the F1100 sample that had dropped below 500 $mV_{Ag/AgCl}$, the pits had grown further and more pits were observed. This shows that the assumption of using 500 $mV_{Ag/AgCl}$ as a limit for pitting initiation is reasonable.

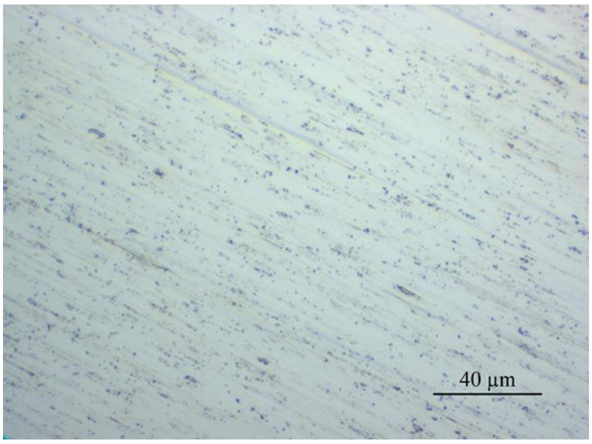

Figure 4.58: H920 after the modified ASTM G48 pitting test. Only small areas of attack are visible.

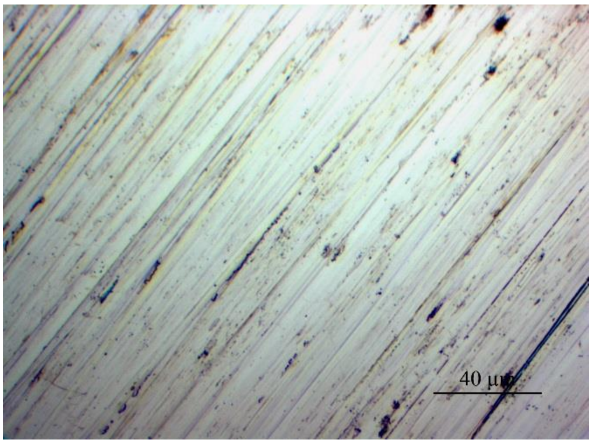

Figure 4.59: F920 after the modified ASTM G48 pitting test. Only small areas of attack are visible.

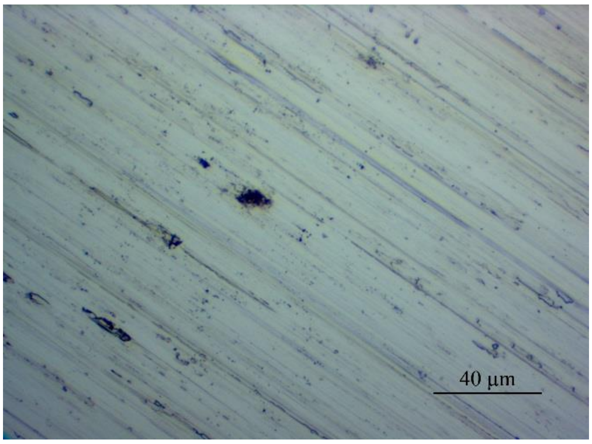

Figure 4.60: F1010 after the modified ASTM G48 pitting test. The areas of attack have grown compared to H920 and F920.

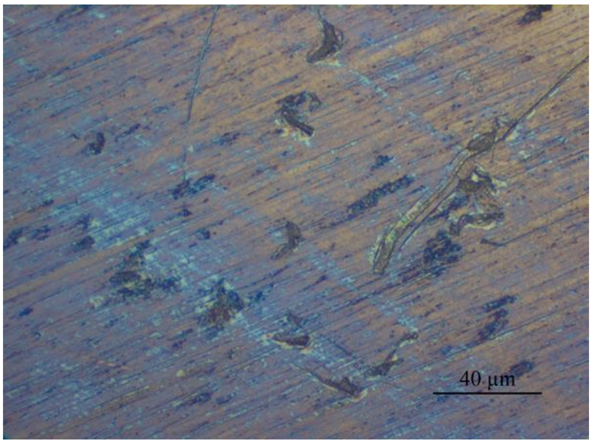

Figure 4.61: F1100-2 after the modified ASTM G48 pitting test, where pitting was initiated. The size and amount of pits have increased compared to H920, F920 and F1010.

4.9 Hydrogen measurements

The hydrogen content in the different versions of Inconel 625 as found by SINTEF is given in parts per million by weight (ppmw) in Table 4.13. H920 and F920 appear to have a lower hydrogen content than the other samples, while the highest hydrogen concentration is found in F1010. Note that these findings are subject to uncertainty, as only one sample from each version of Inconel 625 was tested. However, the main reason for measuring the hydrogen content was to verify that hydrogen had diffused into the samples during the hydrogen pre-charging. This was confirmed by the presence of hydrogen in all the samples.

Table 4.13: Hydrogen content in the different versions of Inconel 625 in parts per million by weight (ppmw).

Material	Hydrogen content [ppmw]
H920	14.13
F920	18.51
F1010	29.57
F1100	24.90
C1150	24.62

4.10 Hydrogen profile

The theoretical hydrogen profile for the hydrogen-exposed HISC samples was estimated by using Equation 4 and the temperature dependent diffusion coefficient of Alloy 718 (UNS N07718). Although extensive research was performed trying to find a temperature dependent diffusion coefficient for Inconel 625, no such constant could be found in the literature. However, the diffusion coefficient for Inconel 625 at 25°C was found to be $D = 2.2\times10^{-11}$ cm^2 s^{-1} [39]. By comparing this constant to several other diffusion constants for similar nickel alloys, it was found that the best approximation was the temperature dependent diffusion coefficient for Inconel 718, which gave a value of $D = 2.0\times10^{-11}$ cm^2 s^{-1} at 25°C [65]. The temperature dependent diffusion coefficient for Alloy 718 is given by an Arrhenius equation [65]:

$$D = 1.07\times10^{-2}\times e^{-\frac{49790}{RT}}\ [\frac{cm^2}{s}] \tag{13}$$

Where R is the gas constant in J K^{-1} mol^{-1}. At 120°C, which was the temperature used during pre-charging, the diffusion coefficient equals 2.579×10^{-9} cm^2 s^{-1}. Furthermore, by setting the initial hydrogen concentration in the samples equal to zero, i.e. $C_0 = 0$, Equation 4 can be written as:

$$\frac{C(x,t)}{C_s} = 1 - \mathrm{erf}(\frac{x}{2\sqrt{Dt}}) \tag{14}$$

By combining Equation 13 and Equation 14, the hydrogen profile for Inconel 625 can be estimated. The time (t) used was the duration of the hydrogen charging, i.e. six days, while the length (x) used was the diameter of the samples, i.e. 3mm. As a simplification, the hydrogen concentration is plotted as one-dimensional, instead of using the circular geometry of the samples. The normalized hydrogen profile is illustrated in Figure 4.62.

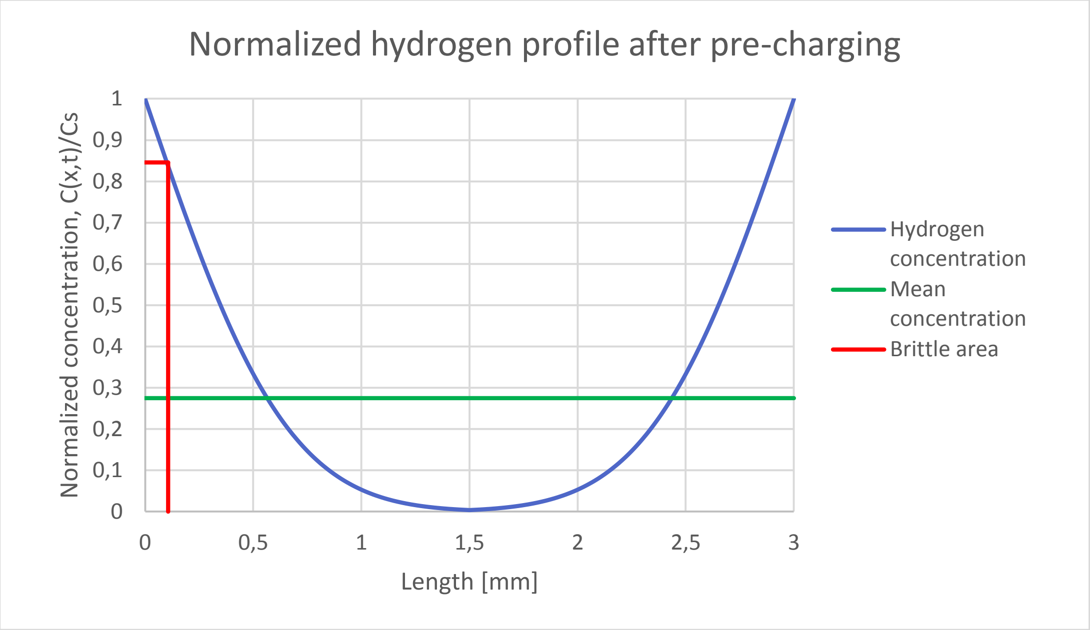

Figure 4.62: The normalized hydrogen profile after pre-charging at 120°C.

Since this thesis focuses on the effect of hydrogen on Inconel 625, an estimate for the critical hydrogen concentration necessary to obtain a brittle fracture has been estimated. The estimate is based on the findings in Table 4.10 and Table 4.13, as well as the hydrogen profile given in Figure 4.62. By numerically integrating the area under the curve in Figure 4.62 and dividing this value by the total length, the normalized mean hydrogen concentration was found to be $\frac{C(x,t)}{Cs} = 0.275$. From the hydrogen measurements given in Table 4.13, this value is found to equal 22 ppmw, if the mean hydrogen concentration is defined as the average hydrogen concentration of H920, F920, F1010 and F1100. C1150 is not included since it appeared to contain almost no brittle areas. The surface concentration of hydrogen is then obtained by Equation 15:

$$Cs = \frac{1}{0.275} \times 22\, ppmw = 78.8\, ppmw \tag{15}$$

In Table 4.10, the average length of the brittle layer was found to equal 0.106 mm. This is shown as the red line in Figure 4.62, which intersects the hydrogen profile at $\frac{C(x,t)}{Cs} = 0.845$. The critical hydrogen concentration necessary to obtain a brittle fracture, C_{critical}, can then be found by Equation 16:

$$C_{critical} = 78.8\, ppmw \times 0.845 = 66.7\, ppmw \tag{16}$$

5 Discussion

5.1 Material Characterization

The main purpose of the tensile test performed in this experiment was to acquire values for the subsequent HISC test. However, when these results are combined with the results from the optical microscope, some valuable information appears. As noted previously, the strength of the forged and the HIPed samples increased and the ductility decreased with decreasing grain size, which is in agreement with the literature [12]. However, there seems to be an unreasonably high difference in YS between F920 and F1010, as these samples have an identical grain size. Considering the heat treatment, F1010 should have had larger grains than F920, rather than the identical grain size observed. This is most likely the result of grain boundary pinning, where the continuous layer of grain boundary carbides found in F1010 has suppressed grain growth during heat treatment [20]. Since the grain size is equal in F920 and F1010, the decrease in strength for F1010 can probably be attributed to recovery, where residual stress has been relived and the number of dislocations has decreased. This will facilitate the onset of dislocation motion, i.e. plastic deformation, resulting in a softer material [12]. Since the remaining mechanical properties are relatively equal, heat treatment at 1010°C seems to be unfavorable, as the material becomes softer without gaining a significant positive increase in e.g. ductility.

The results from the EDS analysis were relatively consistent for all the versions of Inconel 625. MC carbides/carbonitrides were present as matrix precipitates in all the samples, and did not dissolve in the matrix even at higher heat treatments. This is consistent with the stable FCC crystal structure of these carbides [17]. The M_6C carbides were present as a series of separate, discrete grain boundary carbides and dissolved partially at 1100°C. No M_6C carbides were found in C1150, which had experienced the highest heat treatment. In F1010 and F1100, some TiN-particles were also present. These seemed to have formed on the expense of the TiC carbides, most likely because of the nitrogen atmosphere used in the heat treatment of F1010 and F1100.

5.2 HISC susceptibility

5.2.1 Fracture values

The fracture values obtained through the stepwise load test indicate that both the forged and the HIPed versions of Inconel 625 were adversely affected by hydrogen. This is evident from the decrease in fracture strength for the samples charged with hydrogen compared to the uncharged reference samples, as given in Table 4.8. However, the degree of embrittlement differs somewhat between the different versions of Inconel 625. One notable difference observed is between F920 and F1010. These samples have an identical grain size and chemical composition, but F1010 experiences a larger decrease in strength when charged with hydrogen than F920. The main difference between these samples is the increased size and amount of grain boundary carbides found in F1010 compared to F920, which indicates that this is the cause of the increased HISC susceptibility. The increased degree of embrittlement by grain boundary carbide precipitation is supported by the literature, where carbides have been shown to act as hydrogen traps [19]. This will increase the local hydrogen concentration at the carbide/matrix interface and thereby lower the fracture strength [19].

Compared to F920 and F1010, F1100 showed a lower reduction of fracture strength when charged with hydrogen. The main reason for this is believed to be the highly reduced amount of grain boundary carbides in F1100 compared to F1010 and F920. Based on the reasoning and findings above, this should reduce the HISC susceptibility. Since the literature has yet to provide a clear answer on the effect of grain size on hydrogen embrittlement in nickel alloys [8, 49-51], the larger grains in F1100 compared to F920 and F1010 should also be considered as a possible reason for the reduced HISC susceptibility of F1100. However, this theory is challenged when F1100 is compared to H920. H920 has the smallest grains amongst the forged and the HIPed samples and contains a high amount of carbides, both in the matrix and at the grain boundaries. Based on the carbides alone, it should be expected that H920 showed a reduction in fracture strength similar to F920 and F1010. However, H920 showed a lower reduction in fracture strength than F920 and F1010, indicating that the smaller grains might have reduced the HISC susceptibility. Nevertheless, it is challenging to reach a conclusion on the topic, as the production of forged and HIPed components gives somewhat different properties. The HIPing process is known to produce a homogeneous microstructure [31], which was shown by Sjöberg and Cornu to reduce the susceptibility to hydrogen embrittlement [49]. As such, the more homogeneous microstructure of H920 might be the reason for the increased resistance to HISC and not the grain size. It is therefore not possible to determine if a reduction in grain size has a positive or negative effect on the fracture strength of Inconel 625 samples charged with hydrogen based on the findings in this thesis alone.

Contrary to the other samples, C1150 showed an increase in strength for the samples charged with hydrogen compared to the reference sample. However, it is uncertain whether this is the result of an actual increase in strength or the result of an error during testing. To the author's knowledge, no such increase has been previously reported in the literature for nickel alloys, making it reasonable to question this finding. An increase in strength might be the result of a microstructural flaw in the reference sample, or an error during the calibration of the Cortest proof rings. A more reasonable assumption is that the reference samples and the samples charged with hydrogen had the same fracture value, i.e. that no change in fracture strength occurred when the samples were charged with hydrogen. However, further testing is required to verify this. Since the amount of hydrogen in C1150 was found to be approximately the same as in the other samples (see Table 4.13), the lack of a reduction in fractures strength seems to indicate that C1150 was less affected by hydrogen than the other samples. One reason for this might be the absence of grain boundary carbides in C1150, since these carbides have been shown to decrease the fracture strength for the other samples. The small grains in C1150 could also contribute to the decrease in strength, but since the abovementioned findings from F1100 might contradict this, the effect of grain size is still uncertain.

5.2.2 Reduction of area

The detrimental effect of hydrogen on Inconel 625 is further supported by the RRA-values, as given in Table 4.9. All the samples charged with hydrogen showed a significant decrease in ductility compared to the reference samples. However, the degree of embrittlement varied somewhat between the different versions of Inconel 625 and some trends appeared. For the forged and the HIPed samples, the RRA decreased with decreasing grain-boundary carbide content, while the RRA decreased with decreasing ASTM grain size for all the versions of Inconel 625. The effect of grain size can be seen to some extent by comparing H920, F920, F1010 and C1150, but because of the high standard deviation of these samples, this trend is subject to a high degree of uncertainty. The reduced HISC susceptibility because of larger grains (i.e. a lower ASTM grain size) is therefore most evident when comparing these four versions of Inconel 625 with F1100, which had larger grains and a significantly lower RRA.

The other factor influencing the difference in RRA is the amount of grain boundary carbides, which has been shown to decrease the ductility of samples charged with hydrogen [19, 66]. This is concurrent with the results found in this thesis for the forged and the HIPed samples, as F1100 showed a lower RRA and a lower carbide content than H920, F920 and F1010. Opposing results were found for C1150, which contained no grain boundary carbides, but had the highest RRA. However, this does not necessarily contradict the adverse effect of grain boundary carbides, as other factors can contribute to the decrease in RRA. For instance, the ductility of nickel alloys charged with hydrogen has been found to decrease with an increasing amount of cold work [24, 25]. Considering the high degree of cold working in C1150 (66%), it is probable that this is the main reason for the decrease in ductility. In general, the high amount of variables present between the different versions of Inconel 625 makes it challenging to reach conclusions, as a certain trend might have several possible explanations. For any further work on the subject, it is therefore recommended that one type of Inconel 625 be studied at a time, or at least that more versions of the same type be used. In this way, it will be easier to identify the factors that contribute to the HISC susceptibility of Inconel 625.

It might be argued that the two abovementioned trends could lead to a wrongful conclusion on the effect of grain size. This statement is based on the fact that H920, F920 and F1010 have smaller grains and more grain boundary carbides than F1100, both of which are used to justify their respective trends. Since the effect of grain boundary carbides has been shown to increase the brittleness of hydrogen-exposed samples [19, 66], while the literature is still inconclusive on the effect of grain size in nickel alloys [8, 49-51], it might be possible that the grain boundary carbides are responsible for the entire RRA-change. A similar argument can be used for C1150, where the introduction of dislocations because of the high degree of cold work might be the reason for the decrease in ductility and not the high ASTM grain size [25]. However, because of the consistency of the trend in regards to the effect of grain size, it is reasonable to assume that larger grains have a beneficial effect on the ductility of hydrogen-exposed samples.

The high RRA of C1150 is surprising when the fracture strength of C1150 is simultaneously considered, as C1150 showed no decrease in strength for the samples charged with hydrogen. This seems to indicate that an increase in RRA is not necessarily accompanied by a decrease in fracture strength. A closer examination of this phenomenon would be interesting in any further work on the topic.

5.2.3 Fracture surfaces and secondary cracking

The results from the fractography given in Section 4.7 show that hydrogen has had an embrittling effect on the forged and the HIPed versions of Inconel 625. This is evident when comparing the reference samples with the samples charged with hydrogen. The reference samples showed only ductile, dimples features over the entire fracture surface, while the samples charged with hydrogen showed a thin (in the order of 100 μm), brittle layer close to the edge. The fracture mode was determined to be mainly transgranular, but the samples containing a high amount of grain boundary carbides, i.e. H920, F920 and F1010, exhibited some degree of intergranular fracture as well. As for the reference samples, the samples charged with hydrogen showed only ductile, dimpled features in the center, which is concurrent with the low hydrogen concentration at this point. The embrittling effect of hydrogen was further supported by the secondary cracks found on the outer surface of all the HIPed and the forged samples charged with hydrogen. No such cracks were present on the reference samples.

Contrary to the HIPed and the forged samples, C1150 showed no secondary cracks on neither the reference sample nor the samples charged with hydrogen. Furthermore, the fracture surfaces of the C1150 samples charged with hydrogen did not exhibit the same degree of embrittlement as the other samples. This was evident by the presence of dimples even in the parts showing some degree of embrittlement, as well as parts near the edge where the fracture was completely ductile. This is concurrent with the strength-values of C1150, but not with the RRA-values. The absence of secondary cracks in C1150 indicates that grain boundary carbides facilitate the formation of secondary cracks. This is based on the observation that secondary cracking was observed in all the versions of Inconel 625 containing grain boundary carbides, but not in C1150, where no grain boundary carbides were found.

Based on the previous sections, some conclusions can be drawn. Firstly, the amount of carbides plays an essential role on the HISC susceptibility of Inconel 625 by reducing the fracture strength and increasing the RRA. Secondly, heat treatment at 1010°C is the most unfavorable, as it results in a reduction of the base strength of the material, as well as making the material more susceptible to HISC. Thirdly, heat treatment at 1100°C is the most favorable amongst the forged qualities, as it reduces the metals susceptibility to HISC, both in regards to fracture strength and RRA. The effect of grain size on the HISC susceptibility of samples charged with hydrogen is still unresolved, but the results seem to indicate that larger grains reduce the RRA-values. Finally, C1150 showed the highest resistance to HISC, as no reduction in fracture strength, nor any secondary cracking were observed.

5.3 Validity of the hydrogen profile

The theoretical hydrogen profile for Inconel 625 and the subsequent estimate of the critical hydrogen concentration necessary for brittle fracture is somewhat flawed and should only be viewed as a rough estimate. The diffusion rate used for the hydrogen profile was that of Inconel 718 and not Inconel 625. Turnbull et al. found that the main factors leading to a reduction in the effective diffusivity in nickel-base alloys were the amount of (Nb,Ti)C and γ' [67]. Inconel 718 contains γ', which is not present in Inconel 625, as well as having about 1.5% more Nb/Ti than Inconel 625 [67]. Based on these considerations, it seems like the estimated diffusion rate of Inconel 625 is too low. This would lead to an underestimate of the critical hydrogen concentration necessary for brittle fracture, as the hydrogen profile should be higher. However, other factors will also contribute to the diffusivity of hydrogen, like the amount of cold work, which has been found to reduce the hydrogen diffusion rate due to hydrogen trapping at dislocations [26]. Hydrogen diffusivity measurements for Inconel 625 would therefore have to be performed to obtain a more accurate hydrogen profile.

Although the critical hydrogen concentration necessary for brittle fracture found in this thesis is only a rough estimate, the method itself does bring up some interesting possibilities. By improving this method, it might be possible to estimate the amount of hydrogen and the extent of the brittle area in service-exposed samples, as well as the corresponding decrease in strength and ductility. This would require further testing to obtain the true value of the critical hydrogen concentration, as well as a temperature dependent diffusion coefficient for Inconel 625. The average surface concentration of hydrogen during cathodic protection would also have to be found.

5.4 Relevance to the industry

Although the HIPed and the forged versions of Inconel 625 were found to be susceptible to HISC, a note should be made on the relevance of these findings to components used in actual service subsea. The samples exposed to hydrogen were found to have their strength reduced by up to 10% of their ultimate tensile strength. As the UTS/YS ratio ranges from about 170-200%

for these samples, a reduction in UTS by 10% still equals a fracture strength that is high above the YS for each material, and therefore most likely also high above the stress that a component is dimensioned for. However, one factor that has to be considered is the amount of hydrogen found in the samples tested in this experiment compared to the amount of hydrogen found in service-exposed samples. Even though extensive research was performed trying to obtain the hydrogen content of service-exposed components made of nickel-base superalloys, no such information could be found. A rough estimate has therefore been performed by evaluating Equation 13 and Equation 14 in Section 4.10. If the temperature is set equal to 10°C, which is a reasonable estimate for a subsea installation, and all other factors remain constant, the time necessary to obtain the same hydrogen profile as given in Figure 4.62 is approximately six years. Furthermore, a subsea component subjected to cathodic protection will evolve less hydrogen on the surface than the samples used in this study. This will increase the time necessary to obtain the hydrogen profile in Figure 4.62 even further. Although the abovementioned considerations only give a rough estimate, they show that long-term exposure to cathodic protection is required to obtain a significant hydrogen concentration in subsea components. They also show that a higher hydrogen concentration than the one obtained in this thesis is possible, but that it will require an exposure time in the order of decades, assuming a metal temperature of 10°C. This seems to indicate that the fracture values obtained in the HISC test are applicative to real components, but that a higher reduction of strength is also possible as a result of a higher hydrogen concentration [34].

Based on the abovementioned hydrogen considerations, it seems reasonable to assume that the fracture strength even for long-term hydrogen-exposed components will be above the YS. However, other factors can also contribute to failure in hydrogen-exposed components. In Section 4.7.7, a high degree of secondary cracking was found for all the forged and the HIPed samples charged with hydrogen. Cracks were even visible in the F1100 sample charged with hydrogen that did not fracture. Such cracks can serve as initiation points for fracture and are especially critical in points of high, local stress. The same samples also showed a high RRA, which indicate that they have become more brittle. This could lead to failure of a component if it no longer shows the ductility it is dimensioned for after exposure to hydrogen. Finally, even though the temperature in the water holds a certain temperature, e.g. 10°C as used in the previous calculations, the temperature of the content inside a component might be a lot higher. This would result in a higher hydrogen diffusivity, which would increase the degree of embrittlement of the component. As a result, the risk of failure due to HISC cannot be excluded for components made of Inconel 625 without further testing.

5.5 Pitting

The critical pitting temperature for the samples examined was found to decrease with increasing heat treatment. This is probably the result of an increase in microsegregation with longer heat treatment, where alloying elements will diffuse to e.g. grain boundaries, thereby lowering the resistance to a corrosion attack in other parts of the material [5]. The strongest support for this is the increased amount of grain boundary carbides found in F1010 compared to F920. These carbides were found by EDS to be of the type $(Mo,Cr,Ni)_6C$. Since chromium and molybdenum are the main contributors to the pitting resistance of Inconel 625 [68], an increased amount of $(Mo,Cr,Ni)_6C$-carbides at the grain boundaries will reduce the resistance to a corrosion attack in the areas close to the grain boundaries due to the depletion of these elements. F1100 showed a lower amount of grain boundary carbides than F920 and F1010. However, it is reasonable to assume that the long heat treatment of F1100 led to a further increase in microsegregation and Mo/Cr-depleted areas, as the pitting resistance of F1100 was lower than for F920 and F1010. Even though the heat treatment showed some detrimental effect on the critical pitting temperature, the CPT was still high for all the samples examined.

From the examination of the corroded sample in Figure 4.56, the corrosion seems to have initiated at the small hole in the sample. This might suggest that the corrosion attack started out as crevice corrosion and not pitting, as crevice corrosion is known to initiate at a lower temperature because of the more aggressive environment associated with this type of attack [5]. However, it seems unlikely that the attack is purely crevice, as the hole is relatively large (1.5 mm) and the critical crevice temperature (CCT) for Inconel 625 has been found to be 30-35°C, while the critical pitting temperature has been reported as >85°C [69]. Nevertheless, some degree of crevice corrosion might have facilitated initiation in the hole, as crevice corrosion is possible in holes up to 3.18 mm [55]. Another explanation might be the surface roughness in the hole, which is expected to be higher than on the sample's outer surface. This will increase the number of initiation sites for pitting, thereby facilitating a corrosion attack [70].

5.6 Sources of error

After the heat treatment, F1010 and F1100 were ground with SiC-paper to remove the black oxide layer that had formed on the samples' surface. This introduces some degree of uncertainty in the fracture values obtained in both the tensile test and the subsequent HISC test. As the grinding for these samples was done by hand, it is reasonable to assume that the surface of F1010 and F1100 were rougher than that of the other samples. Abrasive stripes on the surface of F1010 and F1100 could thereby act as initiation points for fracture, which would reduce the fracture strength of the materials. It is also possible that the same initiation points will have a higher effect on the samples charged with hydrogen compared to the uncharged reference samples, as the reference samples in general are more resistant to fracture. However, it is challenging to determine whether this has been an issue or not, as it would require F1010 and F1100 to be compared to identical samples that were not ground by hand.

An important factor for determining the validity of the conclusions drawn in this thesis is the amount of hydrogen found in the different samples. By considering Table 4.13, there seems to be a substantial difference in the hydrogen content found in H920 and F920 compared to F1010, F1100 and C1150. Since the pre-charging period was approximately the same for all the samples, they should contain the same amount of hydrogen. However, H920 and F920 were stored for almost seven months before hydrogen measurements were done, compared to only one month for the other samples. This will result in some hydrogen diffusing out of the samples, but since the temperature during storage was -20°C, the effect should be minimal. A larger source of error is therefore the amount of samples used in the hydrogen measurements. As only one sample from each version of Inconel 625 was tested for hydrogen, the results are exposed to a high degree of scatter. It is therefore uncertain whether the actual amount of hydrogen is significantly different or not. Nevertheless, a short note should be made on the impacts of a lower hydrogen concentration in H920 and F920, since this would mean that the RRA and reduction in fracture strength is most likely underestimated for these samples. For H920, this could contradict the evidence indicating that smaller grains have a beneficial effect on the fracture strength, which in turn would shift the evidence towards the opposite, i.e. that larger grains have a beneficial effect on the fracture strength. For F920, the implications are not that critical, but it could indicate that heat treating at 1010°C is less detrimental compared to heat treating at 920°C than previously believed.

The limited number of samples used in the HISC test introduces another error source, as it makes the results vulnerable to scatter. This is especially evident for the RRA-values given in Table 4.9, which show a high standard deviation, making it challenging to comment on trends and reach conclusions. The limited number of samples used in this thesis is the result of a limited amount of time and Cortest proof rings available. For any further work on the subject, it is recommended that more samples be used.

The measurements of the Cortest proof rings' diameter during loading were done by hand and are therefore prone to error. As the increase in load from one day to the next led to a change of the Cortest proof rings' diameter in the order of 0.01 mm, it is evident that even small measuring mistakes could lead to substantial error. Depending on the amount of force applied to the caliper, it could show a diameter difference equal to several days of loading. Some of this uncertainty was minimized by using the same operator each day, as the measuring technique became increasingly familiar. Because of the uncertainty related to the loading, HISC experiments in Cortest proof rings are best suited for metals showing a high reduction of fracture strength, as the results for such metals will be less affected by measuring mistakes. Metals showing a low reduction in fracture strength, like the Inconel 625 examined in this thesis, can have their results severely altered by small measuring mistakes. A better solution for such metals is therefore recommended. One suggestion for an improvement is to implement a load cell in the Cortest proof rings. The load could then be directly observed during the tightening of the Cortest proof rings, which would remove the need for measurements of the diameter of the rings, thereby eliminating the error associated with these measurements. This would require a modification of the Cortest proof rings' diameter, as a load cell would have to be fitted into the rings in addition to the sample.

Finally, the high ductility of F1100 led to some error, as two of the samples were too ductile to fracture. It is therefore recommended that nickel alloys exhibiting a ductility above approximately 60% either should have their dimensions modified or not be used in the Cortest proof rings. However, care should be taken if the dimensions are modified, as it might affect the comparability to the standard test samples.

6 Conclusion

The following conclusions has been reached in this project:

- The forged and the HIPed versions of Inconel 625 were susceptible to HISC. This was evident by the reduction of strength and ductility, as well as the embrittled fracture surfaces and secondary cracks observed in SEM.
- The cold worked version of Inconel 625 was less susceptible to HISC, as no reduction in fracture strength, nor any secondary cracking, were observed.
- The forged samples heat-treated at 1010°C experienced the highest HISC susceptibility.
- Heat treatment at 1100°C gave the lowest HISC susceptibility amongst the forged samples, both in regards to fracture strength and RRA.
- Grain boundary carbides of the type M_6C were identified as the main reason for increased HISC susceptibility.
- The effect of grain size on the HISC susceptibility of samples charged with hydrogen is still unresolved, but the results indicate that larger grains have a beneficial effect on the ductility.
- The critical hydrogen concentration necessary to obtain brittle fracture in Inconel 625 was estimated to be 66.7 ppmw.
- The critical pitting temperature decreased with increasing heat treatment.

6.1 Recommendations for further work

- The duration of the hydrogen pre-charging should be varied to investigate the effect of different hydrogen concentrations on the HISC susceptibility of Inconel 625.
- A comparison between the hydrogen concentration in service-exposed samples and samples charged with hydrogen should be done to get a better understanding of the relevance to the industry.
- Diffusivity experiments for Inconel 625 should be performed to obtain a temperature dependent diffusion coefficient.
- A higher number of samples should be used to get results that are less exposed to scatter. This includes more reference samples.

- More variations of each type of Inconel 625 should be studied to make it easier to identify the factors that contribute to the HISC susceptibility.
- For metals showing a low decrease in fracture strength, it is recommended that a modified version of the Cortest proof rings be used to obtain results that are more accurate. A suggestion for such an improvement is to implement a load cell in the Cortest proof rings.

References

1. Eiselstein, H.L. and D.J. Tillack, *The invention and definition of alloy 625.* Superalloys, 1991. **718**(625): p. 1-14.
2. Shoemaker, L.E., *Alloys 625 and 725: Trends in Properties and Applications*, in *SUPERALLOYS 718, 625 706 AND VARIOUS DERIVATIVES*, E.A. Loria, Editor. 2005, Minerals, Metals, and Materials Society. p. 409-418.
3. Floreen, S., G.E. Fuchs, and W.J. Yang, *The Metallurgy of Alloy 625*. 1994.
4. (ISO), I.O.f.S., *ISO 21457:2010 Petroleum, petrochemical and natural gas industries -- Materials selection and corrosion control for oil and gas production systems*. 2010.
5. Talbot, D.E.J. and J.D.R. Talbot, *Corrosion and Science Technology*. 2007: CRC Press.
6. Anderson, T.L., *Fracture Mechanics - Fundamentals and applications*, ed. T.a.F. group. 2005, United States of America: CRC Press.
7. Stenerud, G., R. Johnsen, and J.S. Olsen, *Susceptibility to Hydrogen Induced Stress Cracking of UNS N07718 and UNS N07725 under Cathodic Polarization*. NACE International.
8. Knarbakk, K., *The Effect of Grain Size on Hydrogen Embrittlement of Inconel 718*, in *Department of Materials Science and Engineering*. 2014, NTNU: NTNU.
9. Thorstensen, E.B., *Is Inconel 625 susceptible to hydrogen-induced stress cracking?* 2015, Institutt for materialteknologi: Norwegian University of Science and Technology, Trondheim.
10. Haugsnes, E., *Susceptibility to hydrogen induced stress cracking of Ni-alloys exposed to cathodic polarization*, in *Institutt for produktutvikling og materialer*. 2016, Norwegian University of Science and Technology.
11. Shankar, V., S.R.K. Bhanu, and S.L. Mannan, *Microstructure and mechanical properties of Inconel 625 superalloy.* Journal of Nuclear Materials, 2001. **288**(2–3): p. 222-232.
12. Callister, W.D. and D.G. Rethwisch, *Materials Science and Engineering*. 8th ed. 2011, Asia: John Wiley & Sons Pte Ltd.
13. Sundararaman, M., P. Mukhopadhyay, and S. Banerjee, *Precipitation of the δ-Ni3Nb phase in two nickel base superalloys.* Metallurgical Transactions A, 1988. **19**(3): p. 453-465.
14. DuPont, J.N., J.C. Lippold, and S.D. Kiser, *Precipitation-Strengthened Ni-base Alloys*, in *Welding Metallurgy and Weldability of Nickel-Base Alloys*. 2009, John Wiley & Sons, Inc. p. 157-254.
15. Rai, S.K., et al., *Characterization of microstructures in Inconel 625 using X-ray diffraction peak broadening and lattice parameter measurements.* Scripta Materialia, 2004. **51**(1): p. 59-63.
16. DuPont, J.N., J.C. Lippold, and S.D. Kiser, *Alloying Additions, Phase Diagrams, and Phase Stability*, in *Welding Metallurgy and Weldability of Nickel-Base Alloys*. 2009, John Wiley & Sons, Inc. p. 15-45.
17. Sims, C.T. and W.C. Hagel, *The Superalloys - Vital High Temperature Gas Turbine Materials for Aerospace and Industrial Power*. 1972, New York: John Wiley and Sons.
18. Pound, B.G., *Hydrogen trapping in precipitation-hardened alloys.* Acta Metallurgica et Materialia, 1990. **38**(12): p. 2373-2381.
19. Symons, D.M., *The effect of carbide precipitation on the hydrogen-enhanced fracture behavior of alloy 690.* Metallurgical and Materials Transactions A, 1998. **29**(4): p. 1265-1277.

20. Nes, E., N. Ryum, and O. Hunderi, *On the Zener drag.* Acta Metallurgica, 1985. **33**(1): p. 11-22.
21. Chokshi, A.H., et al., *On the validity of the hall-petch relationship in nanocrystalline materials.* Scripta Metallurgica, 1989. **23**(10): p. 1679-1683.
22. ASM, *ASM Handbook Volume 4 Heat Treating*, in *Heat Treating of Nickel and Nickel Alloys*. 1991, ASM.
23. Doherty, R.D., et al., *Current issues in recrystallization: a review.* Materials Science and Engineering: A, 1997. **238**(2): p. 219-274.
24. El kebir, O.A. and A. Szummer, *Comparison of hydrogen embrittlement of stainless steels and nickel-base alloys.* International Journal of Hydrogen Energy, 2002. **27**(7–8): p. 793-800.
25. Pound, B.G., *Hydrogen trapping in work-hardened alloys.* Acta Metallurgica et Materialia, 1991. **39**(9): p. 2099-2105.
26. Lee, S.M. and J.Y. Lee, *The trapping and transport phenomena of hydrogen in nickel.* Metallurgical Transactions A, 1986. **17**(2): p. 181-187.
27. Uhlemann, M. and B.G. Pound, *Diffusivity, solubility and trapping behavior of hydrogen in alloys 600, 690tt and 800.* Corrosion Science, 1998. **40**(4): p. 645-662.
28. Huang, H. and W.J.D. Shaw, *Cold work effects on sulfide stress cracking of pipeline steel exposed to sour environments.* Corrosion Science, 1993. **34**(1): p. 61-78.
29. KANE, R.D., et al., *Factors Influencing the Embrittlement of Cold Worked High Alloy Materials in H2S Environments.* Corrosion, 1977. **33**(9): p. 309-320.
30. Richerson, D.W., *Modern ceramic engineering - Properties, Processing and Use in design*. 2006, New York, USA: CRC Press - Taylor and Francis group.
31. Bocanegra-Bernal, M.H., *Hot Isostatic Pressing (HIP) technology and its applications to metals and ceramics.* Journal of Materials Science, 2004. **39**(21): p. 6399-6420.
32. Atkinson, H.V. and S. Davies, *Fundamental aspects of hot isostatic pressing: An overview.* Metallurgical and Materials Transactions A, 2000. **31**(12): p. 2981-3000.
33. Rao, G.A., et al., *Characterisation of hot isostatically pressed nickel base superalloy Inconel* 718.* Materials science and technology, 2003. **19**(3): p. 313-321.
34. Hicks, P.D. and C.J. Altstetter, *Internal hydrogen effects on tensile properties of iron- and nickel-base superalloys.* Metallurgical Transactions A, 1990. **21**(1): p. 365-372.
35. Martin, M.L., et al., *Hydrogen-induced intergranular failure in nickel revisited.* Acta Materialia, 2012. **60**(6–7): p. 2739-2745.
36. Lynch, S., *Hydrogen embrittlement phenomena and mechanisms*. 2012. p. 105.
37. Van Leeuwen, H.P., *The kinetics of hydrogen embrittlement: A quantitative diffusion model.* Engineering Fracture Mechanics, 1974. **6**(1): p. 141-161.
38. Bogkris, J.O.M., et al., *The effect of stress on the chemical potential of hydrogen in iron and steel.* Acta Metallurgica, 1971. **19**(11): p. 1209-1218.
39. Pound, B.G., *Evaluation of a Diffusion/Trapping Model for Hydrogen Ingress in High-Strength Alloys*. 1994.
40. Mohtadi-Bonab, M.A., J.A. Szpunar, and S.S. Razavi-Tousi, *Hydrogen induced cracking susceptibility in different layers of a hot rolled X70 pipeline steel.* International Journal of Hydrogen Energy, 2013. **38**(31): p. 13831-13841.
41. Bhadeshia, H.K.D.H. and R. Honeycombe, *2 - The Strengthening of Iron and its Alloys*, in *Steels (Third Edition)*, H.K.D.H.B.R. Honeycombe, Editor. 2006, Butterworth-Heinemann: Oxford. p. 17-38.
42. Gangloff, R.P., *Hydrogen assisted cracking of high strength alloys*, in *Comprehensive Structural Integrity*. 2003, Elsevier Science. p. 31-101.
43. Takai, K., et al., *Lattice defects dominating hydrogen-related failure of metals.* Acta Materialia, 2008. **56**(18): p. 5158-5167.

44. Lynch, S.P., *Progress Towards Understanding Mechanisms Of Hydrogen Embrittlement And Stress Corrosion Cracking*. NACE International.
45. Barnoush, A., *Hydrogen embrittlement.* Saarland University, 2011.
46. Takasawa, K., et al., *Effects of Grain Size on Hydrogen Environment Embrittlement of High Strength Low Alloy Steel in 45 MPa Gaseous Hydrogen.* MATERIALS TRANSACTIONS, 2010. **51**(2): p. 347-353.
47. Tsay, L.W., H.L. Lu, and C. Chen, *The effect of grain size and aging on hydrogen embrittlement of a maraging steel.* Corrosion Science, 2008. **50**(9): p. 2506-2511.
48. Zan, N., et al., *Effects of grain size on hydrogen embrittlement in a Fe-22Mn-0.6C TWIP steel.* International Journal of Hydrogen Energy, 2015. **40**(33): p. 10687-10696.
49. Sjoberg, G. and D. Cornu, *Hydrogen embrittlement of cast alloy 718 effects of homogenization, grain size and d-phase.* Superalloys 718, 625. 706 and Various Derivatives 2001.
50. Gray, H., *The effect of microstructure on hydrogen embrittlement of the nickel base superalloy, Udimet 700*, in *19th Structures, Structural Dynamics and Materials Conference*. 1978, NASA: Bethesda, Maryland.
51. Latanision, R.M. and H. Opperhauser, *The intergranular embrittlement of nickel by hydrogen: The effect of grain boundary segregation.* Metallurgical Transactions, 1974. **5**(2): p. 483-492.
52. Trethewy, K.R. and J. Chamberlain, *Corrosion for students of science and engineering*. 1988, Longman House, Burnt Mill, Harlow, England: Longman Scientific and Technical. 382.
53. Johnsen, R., et al., *New Improved Method For Hisc Testing Of Stainless Steels Under Cathodic Protection*. NACE International.
54. Ho, Y.S. and G. McKay, *A Comparison of Chemisorption Kinetic Models Applied to Pollutant Removal on Various Sorbents.* Process Safety and Environmental Protection, 1998. **76**(4): p. 332-340.
55. Schweitzer, P.A., *Fundamentals of Metallic Corrosion - Atmospheric and Media Corrosion of Metals*. 2007: CRC Press - Taylor and Francis Group.
56. *VDM Metals*. [cited 2016 June 2.]; Available from: http://www.vdm-metals.com/en/.
57. *Kennametal*. [cited 2016 June 2.]; Available from: http://www.kennametal.com/.
58. *ATI Metals*. [cited 2016 June 2.]; Available from: https://www.atimetals.com.
59. ASTM, *ASTM G48 - Standard Test Methods for Pitting and Crevice Corrosion Resistance of Stainless Steels and Related Alloys by Use of Ferric Chloride Solution*. 2015.
60. NACE, *NACE Standard TM0177-96: Laboratory Testing of Metals for Resistance to Sulfide Stress Cracking and Stress Corrosion Cracking in H2S Environments*. 1996.
61. ASTM, *ASTM E407 - 07 Standard Practice for Microetching Metals and Alloys*. 2015.
62. ASTM, *ASTM E112 - Standard Test Methods for Determining Average Grain Size*. 2013.
63. ASTM, *ASTM E140 - 12b Standard Hardness Conversion Tables for Metals Relationship Among Brinell Hardness, Vickers Hardness, Rockwell Hardness, Superficial Hardness, Knoop Hardness, Scleroscope Hardness, and Leeb Hardness*. 2013, ASTM International.
64. Song, J. and W.A. Curtin, *A nanoscale mechanism of hydrogen embrittlement in metals.* Acta Materialia, 2011. **59**(4): p. 1557-1569.
65. Robertson, W.M., *Hydrogen permeation and diffusion in inconel 718 and incoloy 903.* Metallurgical Transactions A, 1977. **8**(11): p. 1709-1712.
66. Hicks, P.D. and C.J. Altstetter, *Hydrogen-enhanced cracking of superalloys.* Metallurgical Transactions A, 1992. **23**(1): p. 237-249.

67. Turnbull, A., et al., *Hydrogen transport in nickel-base alloys.* Metallurgical Transactions A, 1992. **23**(12): p. 3231-3244.
68. Mishra, A.K. and D.W. Shoesmith, *Effect of Alloying Elements on Crevice Corrosion Inhibition of Nickel-Chromium-Molybdenum-Tungsten Alloys Under Aggressive Conditions: An Electrochemical Study*. Corrosion, 2014. **70**(7): p. 721-730.
69. McCoy, S., et al., *High performance age-hardenable nickel alloys solve problems in sour oil and gas service.* Balance, 2002. **14**(5): p. 16-23.
70. Burstein, G.T. and P.C. Pistorius, *Surface Roughness and the Metastable Pitting of Stainless Steel in Chloride Solutions.* Corrosion, 1995. **51**(5): p. 380-385.

Appendix A

Picture of experimental setup for hydrogen pre-charging and modified ASTM G48 test

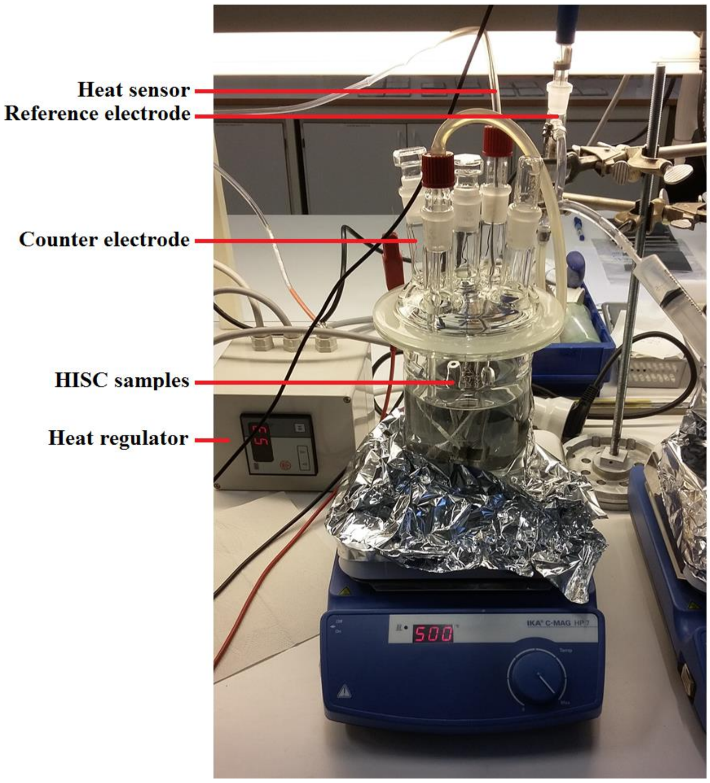

Figure A.1: Picture of experimental setup for the hydrogen pre-charging.

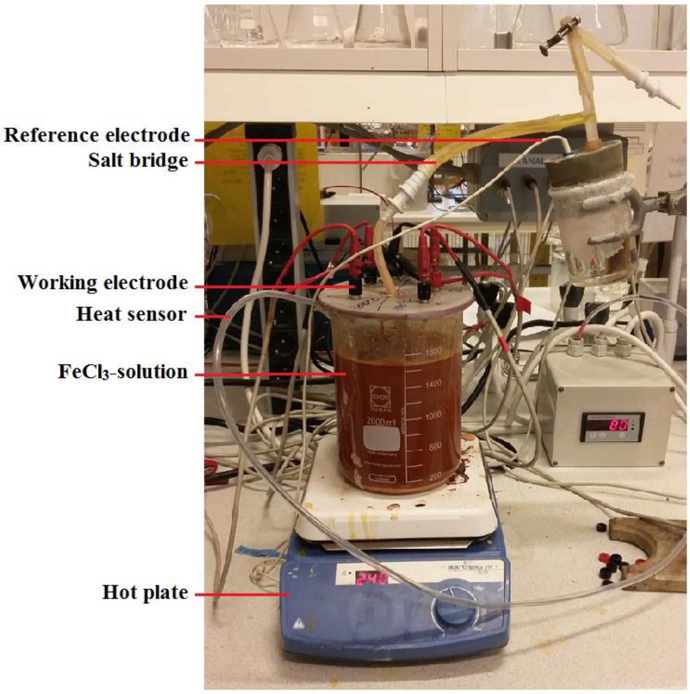

Figure A.2: Picture of the experimental setup for the modified version of the ASTM G48 test.

Appendix B

Description of the hydrogen content analyzing method as given by SINTEF

The samples are heated in a graphite crucible in the pulse furnace. During this melt extraction Hydrogen and Carbon Monoxide are released from the sample and taken up by the carrier gas flow. On passing the dust trap, oxidizing agents and a molecular sieve, coarse particles are removed from the carrier gas and CO2 as well as H2O are retained. The thermal conductivity measuring cell of the H-mat 225 operates as Hydrogen detector. Thermistors in a bridge circuit measure the thermal conductivity of the carrier gas flow and of a reference gas flow. A change of the thermal conductivity of the carrier gas flow due to the released Hydrogen produces a measurement signal on comparing the two gas flows. The magnitude of this signal is proportional to the Hydrogen content of the sample. The course in time of the measured signal is displayed on the graphics screen. The analyzer can be checked by this means to ensure that it is functioning correctly. The time integral of a measured curve corresponds to the Hydrogen content of the particular sample. The central processing unit calculates the Hydrogen content to an accuracy of 0.001 ppm. *

Nitrogen gas is used as carrier gas. Hydrogen gas is used for calibration.

** Operating Manual H-mat 225, JUWE Laborgeräte GmbH*

Appendix C

EDS examinations

Figure C.1 shows a SEM image indicating some of the spots examined by EDS for H920.

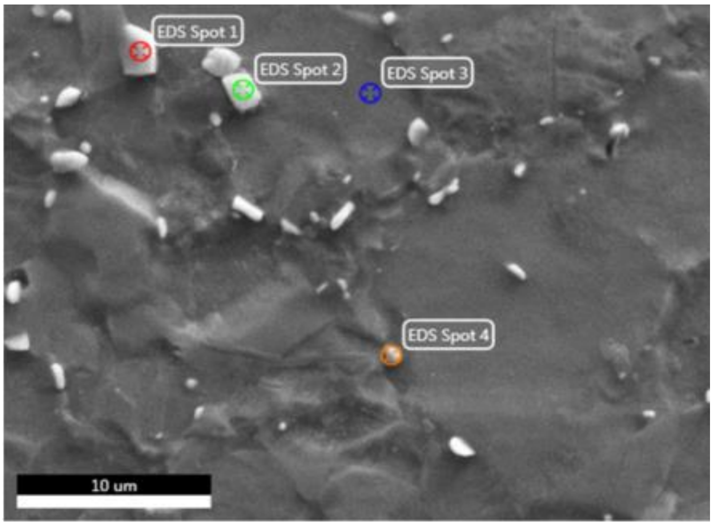

Figure C.1: Spots marked for chemical examination by EDS for H920.

Table C.1, Table C.2 and Table C.3 gives the chemical content and error of spot three, one and four, respectively.

Table C.1: Chemical content of spot three from H920.

Element	Weight %	Atomic %	Error %
C	5.26	21.41	11.38
N	0.18	0.64	99.99
Nb	2.16	1.14	8.00
Mo	7.21	3.67	5.33
Ti	0.12	0.13	34.11
Cr	20.39	19.16	1.96
Mn	0.30	0.27	26.28
Fe	0.23	0.20	26.96
Ni	64.14	53.38	2.05

Table C.2: Chemical content of spot one from H920.

Element	Weight %	Atomic %	Error %
C	13.81	41.74	10.74
N	7.84	20.32	15.38
Nb	36.19	14.14	1.34
Mo	16.23	6.14	2.30
Ti	0.38	0.29	19.10
Cr	19.41	13.56	2.46
Mn	0.30	0.20	28.36
Fe	0.16	0.10	55.54
Ni	5.68	3.51	3.81

Table C.3: Chemical content of spot four from H920.

Element	Weight %	Atomic %	Error %
C	9.69	35.27	10.59
N	0.00	0.00	99.99
Nb	7.98	3.76	4.73
Mo	8.06	3.67	4.42
Ti	0.31	0.28	11.81
Cr	19.71	16.58	2.04
Mn	0.55	0.44	19.54
Fe	0.23	0.18	21.82
Ni	53.46	39.81	2.10

Figure C.2 shows a SEM image indicating some of the spots examined by EDS for F920.

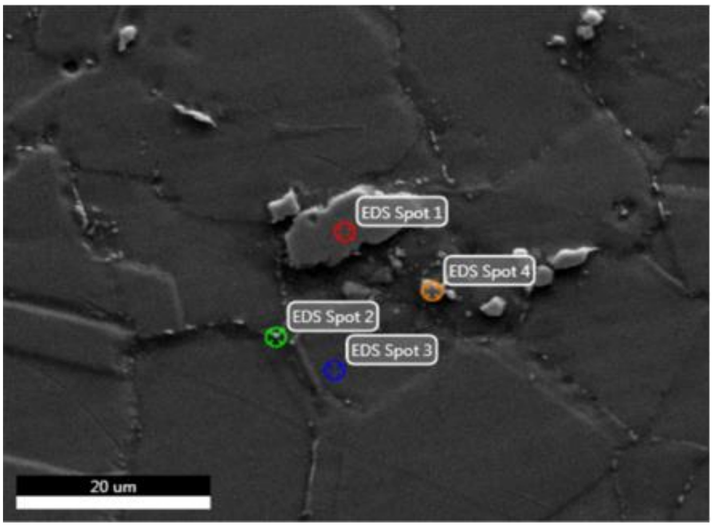

Figure C.2: Spots marked for chemical examination by EDS for F920.

Table C.4, Table C.5 and Table C.6 gives the chemical content and error of spot three, one and two, respectively.

Table C.4: Chemical content of spot three from F920.

Element	Weight %	Atomic %	Error %
C	1.39	6.51	14.81
N	0.00	0.00	99.99
Nb	2.93	1.77	7.64
Mo	8.37	4.91	4.74
Ti	0.41	0.48	12.47
Cr	22.28	24.12	1.98
Mn	0.55	0.57	18.58
Fe	4.11	4.14	3.84
Ni	59.97	57.49	2.16

Table C.5: Chemical content of spot one from F920.

Element	Weight %	Atomic %	Error %
C	15.38	56.28	11.33
N	0.00	0.01	99.99
Nb	69.60	32.93	1.35
Mo	5.36	2.46	5.04
Ti	5.73	5.26	4.09
Cr	1.02	0.86	12.07
Mn	0.12	0.10	56.33
Fe	0.31	0.24	33.37
Ni	2.48	1.86	7.31

Table C.6: Chemical content of spot two from F920.

Element	Weight %	Atomic %	Error %
C	5.73	23.16	49.92
N	3.31	11.46	99.99
Nb	10.73	5.60	15.75
Mo	26.72	13.52	9.93
Ti	0.59	0.60	79.10
Cr	16.25	15.16	15.96
Mn	0.83	0.73	80.46
Fe	3.61	3.14	50.28
Ni	32.22	26.63	13.66

Figure C.3 shows a SEM image indicating some of the spots examined by EDS for F1010.

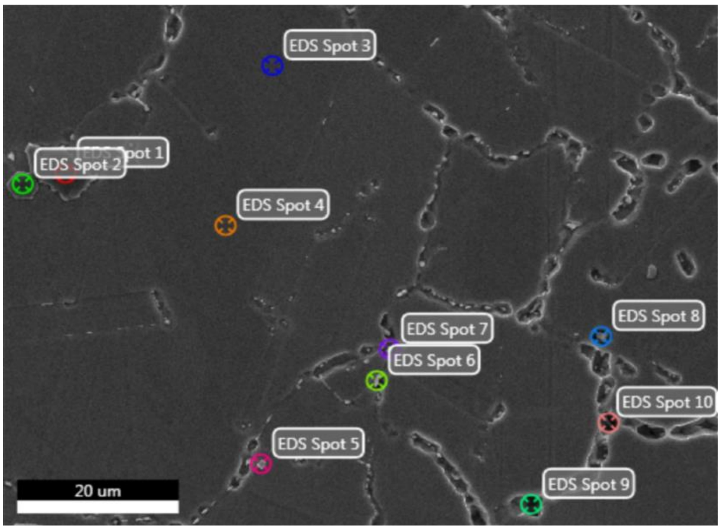

Figure C.3: Spots marked for chemical examination by EDS for F1010.

Table C.7, Table C.8 and Table C.9 gives the chemical content and error of spot four, one and five, respectively.

Table C.7: Chemical content of spot four from F1010.

Element	Weight %	Atomic %	Error %
C	1.89	8.56	93.66
N	0.29	1.13	99.99
Nb	2.82	1.65	48.06
Mo	6.41	3.63	20.75
Ti	1.07	1.21	68.42
Cr	21.26	22.21	9.28
Mn	1.32	1.31	76.21
Fe	4.90	4.76	28.24
Ni	60.05	55.56	7.27

Table C.8: Chemical content of spot one from F1010.

Element	Weight %	Atomic %	Error %
C	2.49	7.32	59.64
N	14.35	36.2	36.64
Nb	10.04	3.82	14.77
Mo	1.72	0.63	66.68
Ti	64.50	47.58	4.96
Cr	2.79	1.90	70.04
Mn	1.10	0.71	82.08
Fe	0.79	0.50	88.38
Ni	2.23	1.34	75.95

Table C.9: Chemical content of spot five from F1010.

Element	Weight %	Atomic %	Error %
C	6.88	27.4	44.44
N	1.95	6.67	99.99
Nb	9.12	4.70	16.1
Mo	24.98	12.46	9.31
Ti	1.23	1.23	69.38
Cr	17.43	16.05	12.7
Mn	1.03	0.89	77.54
Fe	2.97	2.55	47.99
Ni	34.4	28.25	10.77

Figure C.4 shows a SEM image indicating some of the spots examined by EDS for F1100.

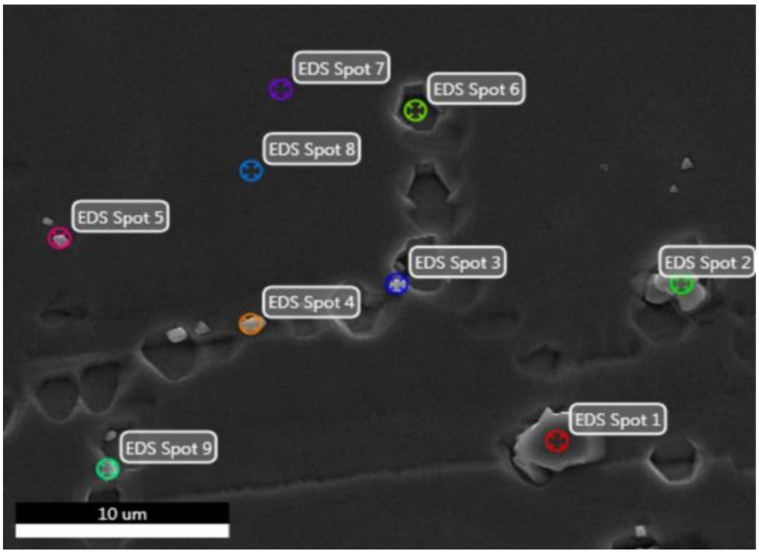

Figure C.4: Spots marked for chemical examination by EDS for F1100.

Table C.10, Table C.11 and Table C.12 gives the chemical content and error of spot seven, one and four, respectively.

Table C.10: Chemical content of spot seven from F1100.

Element	Weight %	Atomic %	Error %
C	4.97	19.74	44.89
N	1.29	4.39	99.99
Nb	2.70	1.38	47.71
Mo	6.95	3.45	19.28
Ti	1.19	1.18	67.41
Cr	21.56	19.77	9.22
Mn	1.19	1.03	76.95
Fe	5.25	4.48	26.55
Ni	54.89	44.57	7.41

Table C.11: Chemical content of spot one from F1100.

Element	Weight %	Atomic %	Error %
C	14.41	52.93	33.42
N	0.57	1.80	99.99
Nb	64.08	30.42	4.76
Mo	7.36	3.38	27.77
Ti	5.65	5.20	21.17
Cr	1.95	1.66	62.87
Mn	1.85	1.49	67.43
Fe	0.89	0.70	75.37
Ni	3.22	2.42	60.16

Table C.12: Chemical content of spot four from F1100

Element	Weight %	Atomic %	Error %
C	26.88	63.08	9.51
N	3.33	6.70	19.50
Nb	6.05	1.84	3.70
Mo	16.91	4.97	2.09
Ti	0.24	0.14	23.26
Cr	13.86	7.51	2.14
Mn	0.21	0.11	35.61
Fe	2.22	1.12	5.22
Ni	30.29	14.54	2.19

Figure C.5 shows a SEM image indicating some of the spots examined by EDS for H920

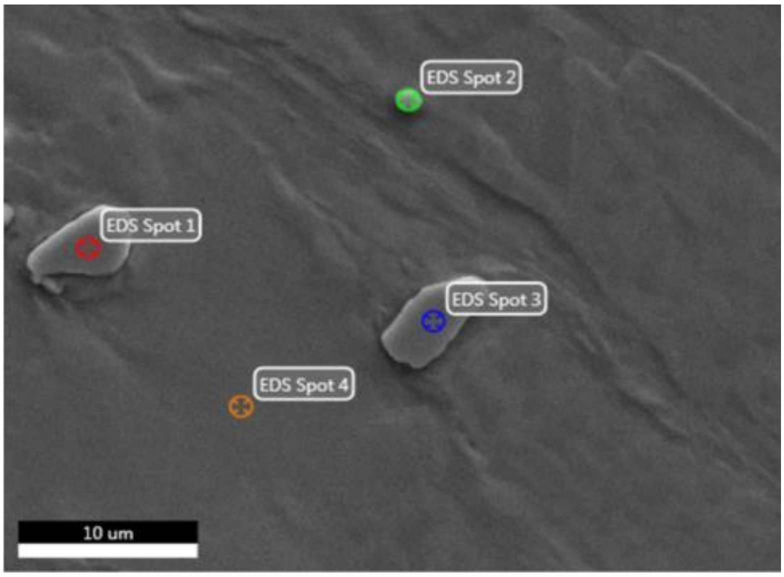

Figure C.5: Spots marked for chemical examination by EDS for C1150.

Table C.13 and Table C.14 gives the chemical content and error of spot four and one, respectively.

Table C.13: Chemical content of spot four from C1150.

Element	Weight %	Atomic %	Error %
C	1.30	6.06	15.16
N	0.06	0.24	99.99
Nb	2.51	1.52	7.68
Mo	7.26	4.25	5.25
Ti	0.31	0.36	20.72
Cr	21.48	23.19	1.99
Mn	0.36	0.37	26.45
Fe	4.55	4.57	3.95
Ni	62.17	59.44	2.15

Table C.14: Chemical content of spot one from C1150

Element	Weight %	Atomic %	Error %
C	12.71	49.52	11.57
N	0.00	0.01	99.99
Nb	65.77	33.12	1.25
Mo	6.02	2.94	5.06
Ti	10.54	10.30	3.58
Cr	1.36	1.22	10.75
Mn	0.27	0.23	37.94
Fe	0.47	0.39	20.85
Ni	2.86	2.28	6.28

Appendix D

Fracture values according to Excel sheet

Table D.1, Table D.2 and Table D.3 shows the fracture values according to the Excel sheet supplied by co-supervisor Roy Johnsen. The values are given as a percentage of the lowest yield strength for each version of Inconel 625, as found in Table 4.1.

Table D.1: Fracture values according to the supplied Excel sheet as percentage of the yield strength for H920 and F920.

Sample	**H920**		**F920**	
	No fracture [%]	**Fracture [%]**	**No fracture [%]**	**Fracture [%]**
1 (reference)	190	194	174	178
2	174	178	154	158
3	178	182	150	154
4	182	186	154	158
5	182	186	158	162

Table D.2: Fracture values according to the supplied Excel sheet as percentage of the yield strength for F1010 and F1100.

Sample	**F1010**		**F1100**	
	No fracture [%]	**Fracture [%]**	**No fracture [%]**	**Fracture [%]**
1 (reference)	186	190	204	No fracture
2	168	172	192	196
3	168	172	188	192
4		<100	180	184
5	180	184	204	No fracture

Table D.3: Fracture values according to the supplied Excel sheet as percentage of the yield strength for C1150.

Sample	**C1150**	
	No fracture [%]	**Fracture [%]**
1 (reference)	106	110
2	110	112
3	106	110
4	102	106

Appendix E

Risk assessment

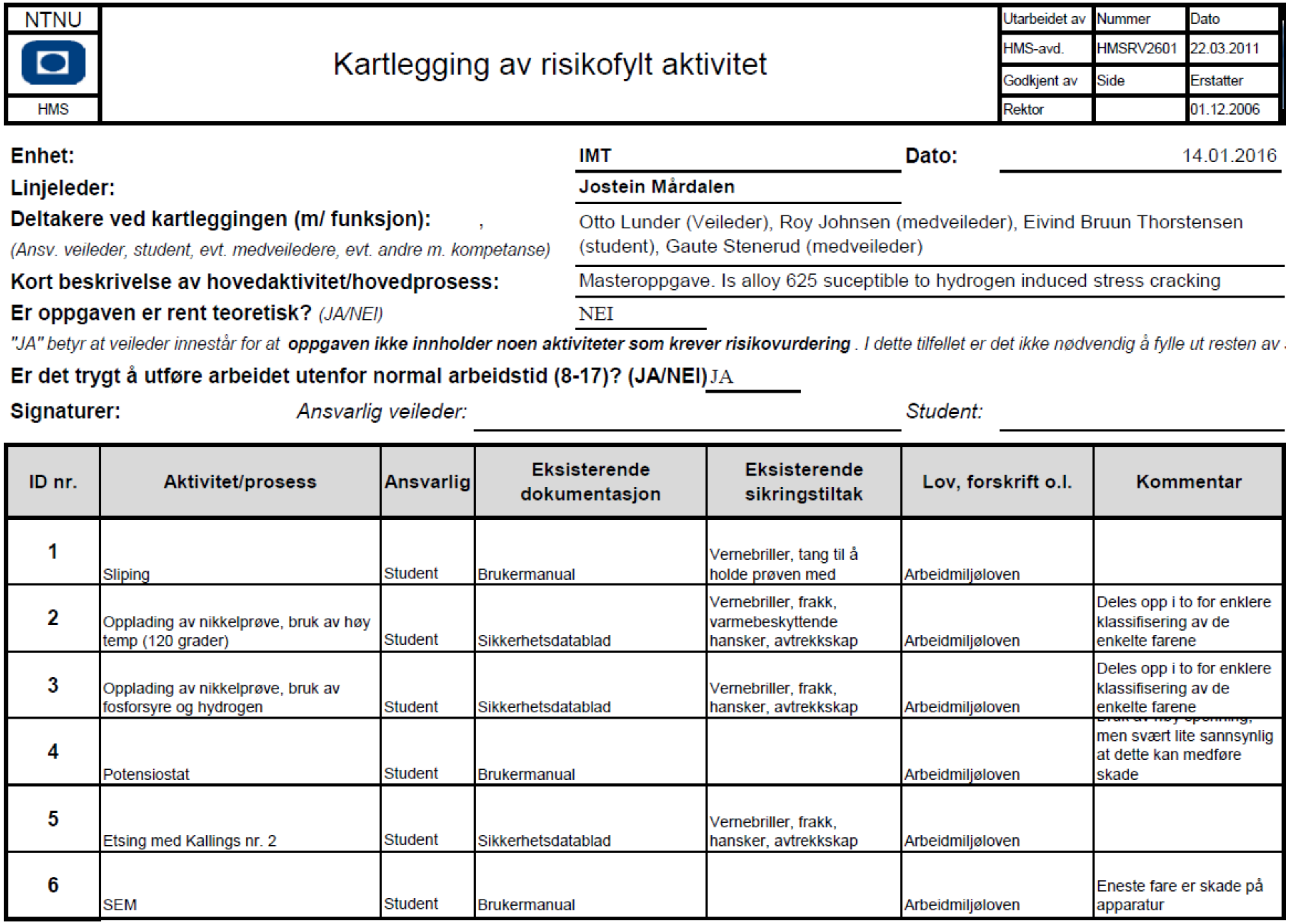

NTNU HMS	Kartlegging av risikofylt aktivitet	Utarbeidet av	Nummer	Dato
		HMS-avd.	HMSRV2601	22.03.2011
		Godkjent av	Side	Erstatter
		Rektor		01.12.2006

Enhet: **IMT** **Dato:** 14.01.2016

Linjeleder: **Jostein Mårdalen**

Deltakere ved kartleggingen (m/ funksjon): , Otto Lunder (Veileder), Roy Johnsen (medveileder), Eivind Bruun Thorstensen (student), Gaute Stenerud (medveileder)

(Ansv. veileder, student, evt. medveiledere, evt. andre m. kompetanse)

Kort beskrivelse av hovedaktivitet/hovedprosess: Masteroppgave. Is alloy 625 suceptible to hydrogen induced stress cracking

Er oppgaven er rent teoretisk? *(JA/NEI)* NEI

"JA" betyr at veileder innestår for at ***oppgaven ikke inneholder noen aktiviteter som krever risikovurdering*** *. I dette tilfellet er det ikke nødvendig å fylle ut resten av*

Er det trygt å utføre arbeidet utenfor normal arbeidstid (8-17)? (JA/NEI) JA

Signaturer: *Ansvarlig veileder:* *Student:*

ID nr.	Aktivitet/prosess	Ansvarlig	Eksisterende dokumentasjon	Eksisterende sikringstiltak	Lov, forskrift o.l.	Kommentar
1	Sliping	Student	Brukermanual	Vernebriller, tang til å holde prøven med	Arbeidmiljøloven	
2	Opplading av nikkelprøve, bruk av høy temp (120 grader)	Student	Sikkerhetsdatablad	Vernebriller, frakk, varmebeskyttende hansker, avtrekkskap	Arbeidmiljøloven	Deles opp i to for enklere klassifisering av de enkelte farene
3	Opplading av nikkelprøve, bruk av fosforsyre og hydrogen	Student	Sikkerhetsdatablad	Vernebriller, frakk, hansker, avtrekkskap	Arbeidmiljøloven	Deles opp i to for enklere klassifisering av de enkelte farene
4	Potensiostat	Student	Brukermanual		Arbeidmiljøloven	Bruk av høy spenning, men svært lite sannsynlig at dette kan medføre skade
5	Etsing med Kallings nr. 2	Student	Sikkerhetsdatablad	Vernebriller, frakk, hansker, avtrekkskap	Arbeidmiljøloven	
6	SEM	Student	Brukermanual		Arbeidmiljøloven	Eneste fare er skade på apparatur

7	Strekkprøving	Student	Brukermanual	Vernebriller	Arbeidmiljøloven	
8	Lysmikroskopi	Student	Brukermanual		Arbeidmiljøloven	Eneste fare er skade på apparatur
9	Hardhetstesting	Student	Brukermanual		Arbeidmiljøloven	Eneste fare er skade på apparatur
10	Varmebehandling	Student	Brukermanual		Arbeidmiljøloven	Fare for brannskader

NTNU HMS /KS	Risikovurdering	Utarbeidet av	Nummer	Dato
		HMS-avd.	HMSRV2603	04.02.2011
		Godkjent av	Side	Erstatter
		Rektor		09.02.2010

Enhet: ***IMT*** **Dato:** 14.01.2016

Linjeleder: ***Jostein Mårdalen***

Deltakere ved risikovurderingen (m/ funksjon): Otto Lunder (Veileder), Roy Johnsen (medveileder), Eivind Bruun Thorstensen (student), Gaute Stenerud (medveileder)

(Ansv. veileder, student, evt. medveiledere, evt. andre m. kompetanse)

Risikovurderingen gjelder hovedaktivitet: Masteroppgave. Is alloy 625 suceptible to hydrogen induced stress cracking

Signaturer: *Ansvarlig veileder:* *Student:*

ID nr.	Aktivitet/prosess fra kartleggingsskjemaet	Mulig uønsket hendelse	Vurdering av sann-synlighet (1-5)	Vurdering av konsekvens				Risiko-verdi (menn-eske)	arer/ status Forslag til tiltak
				Menneske (A-E)	Ytre miljø (A-E)	Øk./ materiell (A-E)	Om-dømme (A-E)		
1	Sliping	Oppskraping	1	A	A	A	A	**A1**	Tang brukes for å unngå "slipeskader"
2	Opplading av nikkelprøve, bruk av høy temp (120 grader)	Brannskader	2	A	A	C	A	**A2**	Faren for å brenne seg er størst, men minst
3	Opplading av nikkelprøve, bruk av fosforsyre og hydrogen	Etseskader, eksplosjonsfare	1	C	A	C	A	**C1**	Fare for etseskader og eksplosjon er svært
4	Potensiostat	Strøm	1	D	A	C	A	**D1**	Faren er stor, men ekstremt lite sannsynlig
5	Etsing med Kallings nr. 2	Etseskader, Brannfarlig væske og damp	1	C	A	A	A	**C1**	Ved bruk av verneutstyr og avtrekkskap
6	SEM	Skade av apparatur	1	A	A	C	A	**A1**	

7	Strekkprøving	Splinter fra pøvebrudd	1	A	A	C	A	**A1**	Ved bruk av vernebriller er dette ufarlig
8	Lysmikroskopi	Skade av apparatur	1	A	A	B	A	**A1**	
9	Hardhetstesting	Skade av apparatur	1	A	A	B	A	**A1**	
10	Varmebehandling	Skade av apparatur	1	C	A	B	A	**C1**	Ved bruk av varmehansker og tang ved